Kumulative Dissertation zur Erlangung des akademischen Doktorgrades der Naturwissenschaften am Institut der Erd- und Umweltwissenschaften, der Mathematisch- Naturwissenschaftlichen Fakultät, der Universität Potsdam.

An investigation of complex deformation patterns detected by using InSAR at Llaima and Tendürek volcanoes

eingereicht von

Hannes Bathke

9th May 2014

betreut am Helmholtz-Zentrum Potsdam Deutsches GeoForschungsZentrum GFZ von:
PD Dr. habil Thomas Walter

Universität Potsdam, Institut für Erd- und Umweltwissenschaften
Karl-Liebknecht-Str. 24, Haus 27,
14469 Potsdam- Golm, Germany

"Insanity: doing the same thing over
and over again and expecting
different results."
Albert Einstein

Eidesstattliche Versicherung

Ich erkläre hiermit, dass ich die vorliegende Arbeit selbstständig und ohne Benutzung anderer als der angegebenen Hilfsmittel angefertigt habe. Aus fremden Quellen direkt oder indirekt übernommene Gedanken sind als solche kenntlich gemacht. Diese Arbeit hat in gleicher oder ähnlicher Form noch keiner anderen Prüfungsbehörde vorgelegen.

Ort, Datum **Unterschrift (Vor- und Zuname)**

Abstract:

Surface displacement at volcanic edifices is related to subsurface processes associated with magma movements, fluid transfers within the volcano edifice and gravity-driven deformation processes. Understanding of associated ground displacements is of importance for assessment of volcanic hazards. For example, volcanic unrest is often preceded by surface uplift, caused by magma intrusion and followed by subsidence, after the withdrawal of magma. Continuous monitoring of the surface displacement at volcanoes therefore might allow the forecasting of upcoming eruptions to some extent.

In geophysics, the measured surface displacements allow the parameters of possible deformation sources to be estimated through analytical or numerical modeling. This is one way to improve the understanding of subsurface processes acting at volcanoes. If all of the processes leading to an eruption or collapse would be understood at once, the behavior of volcanoes could be precisely forecasted and thus social and economic loss could be minimized. Although the monitoring of volcanoes has significantly improved in the last decades (in terms of technical advancements and number of monitored volcanoes), the forecasting of volcanic eruptions remains puzzling.

In this work I contribute towards the understanding of the subsurface processes at volcanoes and thus to the improvement of volcano eruption forecasting. I have investigated the displacement field of Llaima volcano in Chile and of Tendürek volcano in East Turkey by using synthetic aperture radar interferometry (InSAR). Through modeling of the deformation sources with the extracted displacement data, it was possible to gain insights into potential subsurface processes occurring at these two volcanoes that had been barely studied before. The two volcanoes, although of very different origin, composition and geometry, both show a complexity of interacting deformation sources.

At Llaima volcano, the InSAR technique was difficult to apply, due to the large decorrelation of the radar signal between the acquisition of images. I developed a model-based unwrapping scheme, which allows the production of reliable displacement maps at the volcano that I used for deformation source modeling. The modeling results show significant differences in pre- and post-eruptive magmatic deformation source parameters. Therefore, I conjecture that two magma chambers exist below Llaima volcano: a post-eruptive deep one and a shallow one possibly due to the pre-eruptive ascent of magma. Similar reservoir depths at Llaima have been confirmed by independent petrologic studies. These reservoirs are interpreted to be temporally coupled.

At Tendürek volcano I have found long-term subsidence of the volcanic edifice, which can be described by a large, magmatic, sill-like source that is subject to cooling contraction. The displacement data in conjunction with high-resolution optical images, however, reveal arcuate fractures at the eastern and western flank of the volcano. These are most likely the surface expressions of concentric ring-faults around the volcanic edifice that show low magnitudes of slip over a long time. This might be an alternative mechanism for the development of large caldera structures, which are so far assumed to be generated during large catastrophic collapse events.

To investigate the potential subsurface geometry and relation of the two proposed interacting sources at Tendürek, a sill-like magmatic source and ring-faults, I have performed a more sophisticated numerical modeling approach. The optimum source geometries show, that the size of the sill-like source was overestimated in the simple models and that it is difficult to determine the dip angle of the ring-faults with surface displacement data only. However, considering physical and geological criteria a combination of outward-inclined reverse faults in the west and inward-inclined normal faults in the east seem to be the most likely. Consequently, the underground structure at the Tendürek volcano consists of a small, sill-like, contracting, magmatic source below the western summit crater that causes a trapdoor-like faulting along the ring-faults around the volcanic edifice. Therefore, the magmatic source and the ring-faults are also interpreted to be temporally coupled.

In addition, a method for data reduction has been improved. The modeling of subsurface deformation sources requires only a relatively small number of well distributed InSAR observations at the earth's surface. Satellite radar images, however, consist of several millions of these observations. Therefore, the large amount of data needs to be reduced by several orders of magnitude for source modeling, to save computation time and increase model flexibility. I have introduced a model-based subsampling approach in particular for heterogeneously-distributed observations. It allows a fast calculation of the data error variance-covariance matrix, also supports the modeling of time dependent displacement data and is, therefore, an alternative to existing methods.

Zusammenfassung:

Oberflächenverschiebungen an Vulkanen können einerseits durch unterirdische Magmen- oder Fluidbewegungen oder andererseits durch Gravitation verursacht werden. So sind insbesondere vor Eruptionen oft Aufwölbungen an Vulkanen zu beobachten, verursacht durch Magmenintrusion in die Erdkruste. Nach Eruptionen hingegen sinkt das Vulkangebäude aufgrund von Magmenextrusion wieder. Kontinuierliche Messungen an Vulkanen ermöglichen es, Eruptionen teilweise bis auf wenige Tage vorherzusagen.

Die gemessenen Oberflächenverschiebungen können in analytischen oder numerischen Modellierungen genutzt werden, um Parameter eines möglichen Quellprozesses abzuschätzen. Auf diese Art und Weise kann das Verständnis über die unterirdischen Prozesse, die an Vulkanen stattfinden, verbessert werden. Falls eines Tages diese Prozesse vollständig verstanden sein sollten, würde dies eine genaue Vorhersage von Eruptionen an Vulkanen ermöglichen. Damit könnten potentielle soziale und ökonomische Schäden bis auf ein bestimmtes Minimum reduziert werden. Obwohl es in den letzten Jahrzehnten eine enorme Entwicklung und Verbesserung der Überwachung von Vulkanen gab, (sowohl in technischer Hinsicht als auch in der Anzahl der überwachten Vulkane), sind viele Vorhersagen sehr vage und ungenau.

Mit dieser Arbeit möchte ich einen Beitrag zum Verständnis von unterirdischen Prozessen an Vulkanen und auf lange Sicht gesehen, zur Vorhersage von Eruptionen leisten. Ich habe die Vulkane, Llaima in Chile und Tendürek im Osten der Türkei, mit Hilfe der Interferometrie von Radardaten (InSAR) untersucht. Die somit gemessenen Verschiebungen an der Erdoberfläche ermöglichen es, durch Modellierung der möglichen Deformationsquellen, Informationen über die Untergrundstrukturen dieser beiden bisher kaum erforschten Vulkane zu bekommen. Obwohl unterschiedlich in Aufbau, Gesteinszusammensetzung und Entstehung, zeigen beide Vulkane Anzeichen dafür, dass jeweils mehrere interagierende Deformationsquellen im Untergrund existieren.

Am Vulkan Llaima war es schwierig, aufgrund der starken Dekorrelation des Radarsignals zwischen den Satellitenaufnahmen, die InSAR Methode anzuwenden. Ich entwickelte eine Methode um die doppeldeutigen (wrapped) relativen Phasenwerte der Interferogramme modellbasiert in eindeutige (unwrapped) relative Phasenwerte umzurechnen. Die damit erzeugten Oberflächenverschiebungskarten am Vulkan eigneten sich nun für eine anschließende Modellierung der Deformationsquelle. Die Modellierungsergebnisse zeigen signifikante Unterschiede zwischen den Parametern der präeruptiven- und posteruptiven Deformationsquellen. Demzufolge könnten zwei unterschiedliche, interagierende Magmenkam-

mern unter Llaima existieren, eine tiefe, posteruptiv aktive Kammer und eine flache, durch den Aufstieg von Magma präeruptiv aktive Kammer.

Am Vulkan Tendürek ist eine langfristige, kontinuierliche Senkung des Vulkangebäudes zu beobachten, die mit einem großen, aufgrund von Kühlung sich kontrahierenden, magmatischen Sill, erklärbar ist. Unter Hinzunahme von hochauflösenden, optischen Daten jedoch, sind bei genauerer Untersuchung an der Ost- und Westflanke des Vulkanes bogenförmige Strukturen an der Erdoberfläche sichtbar. Diese sind Anzeichen dafür, dass Verwerfungen existieren, die das gesamte Vulkangebäude in einem elliptischen Ring umgeben. Dabei ist zu beobachten, dass die Ringstörungen über Jahrtausende, möglicherweise sogar kontinuierlich, geringe Magnituden von Versatz aufweisen. Bei langer, kontinuierlicher Aktivität über mehrere zehntausende von Jahren, könnte dies ein weiterer Mechanismus zur Entstehung von Calderastrukturen an Vulkanen darstellen, der jedoch sehr langsam verläuft. Im Gegensatz dazu ist die heutige weit verbreitete Auffassung, dass Calderen als Folge katastrophaler Einstürze von Vulkangebäuden entstehen.

Um zu untersuchen welche Geometrie die vorgeschlagenen Strukturen Sill und Ringstörungen an Tendürek im Untergund haben könnten, vollführte ich eine weitaus komplexere numerische Modellierung. Diese zeigt, dass die Größe des Sills ohne Berücksichtigung der Ringstörung um ein Vielfaches überschätzt ist. Die Orientierung und Geometrie der Ringstörungen ist jedoch nicht eindeutig nur mit Oberflächenverschiebungsdaten auflösbar. Unter der Berücksichtigung von geologischen und physikalischen Gesichtspunkten sind nach Außen einfallende Aufschiebungen im Westen und nach Innen einfallende Abschiebungen im Osten die plausibelste Erklärung. Demnach verursacht der kühlende, magmatische Sill unter dem westlichen Krater eine westwärts gerichtete falltürartige Bewegung des Vulkangebäudes entlang der Ringstörungen.

Außerdem habe ich eine Methode zur Datenreduzierung entwickelt. Abhängig vom zu untersuchenden Prozess sind für die Modellierung von unterirdischen Deformationsquellen verhältnismäßig wenige gut verteilte Messpunkte an der Erdoberfläche ausreichend. Satelliten gestützte Radaraufnahmen haben jedoch unter günstigen Bedingungen oft mehrere Millionen dieser Punkte. Deshalb müssen diese riesigen Datensätze auf eine Art und Weise reduziert werden, dass keine oder nur möglichst wenige Informationen verloren gehen. Für diesen Zweck habe ich, ausgehend von einem existierenden Algorithmus, eine modellbasierte Methode zur Reduzierung von besonders heterogen verteilten Oberflächendaten entwickelt. Diese Methode erlaubt eine schnelle Berechnung der Datenfehler Varianz-Covarianz-Matrix, ist besonders gut auf Zeitreihendatensätze anwendbar und stellt somit eine Alternative zu existierenden Algorithmen dar.

Contents

List of Figures

List of Tables

List of Abbreviations

ΔR_{mod}	Modeled synthetic unwrapped displacement in radar line-of-sight.
κ	Smoothing weight
κ_{cost}	Cost function to determine the optimum smoothing weight κ
λ	Wavelength of the radar wave
ϕ_{atm}	Phase change due to atmospheric influences (mainly water vapor)
ϕ_{defo}	Phase change due to a subsurface deformation process
ϕ_{ifg}	Total phase change in an interferogram
ϕ_{mod}	Modeled wrapped phase
ϕ_{noise}	Phase change due to various minor noise sources
ϕ_{orb}	Phase change due to inaccurate satellite orbit information
ϕ_{topo}	Phase change due to topographic height of the surface
ψ_{mod}	Modeled unwrapped phase
ρ	Solution roughness of a result from a distributed slip inversion
$\mathbf{A}/\mathbf{A}_{sub}$	(Subsampled) design matrix for an inverse problem
$\mathbf{C}_{asc/desc}$	Data-error variance-covariance matrix of the ascending/descending satellite tracks
$\mathbf{C}_{mod,k}$	Model Covariance for the k-th subsampled data set
$\mathbf{d}$	Data vector
$\mathbf{d}_{sub}$	Subsampled data set of the full data vector $\mathbf{d}$
$\mathbf{F}$	Displacement in radar LOS
$\mathbf{G}$	Matrix of Green's functions

$\mathbf{g}$	Condition number of the subsampled design matrix $\mathbf{A}_{sub}$
$\mathbf{P}$	Weighting matrix
$\mathbf{v}_{asc/desc}$	Residual displacement of the ascending, descending satellite tracks
$\mathbf{x}$	Vector of model parameters
s_j	Normalized model sensitivity of each j-th data point
w_j	Model sensitivity of each j-th data point
Θ	L1-norm cost function for model based unwrapping
θ	Wrapped phase residual between $\psi_{obs} - \psi_{mod}$
D	Discrete Laplacian Operator
f	Cost function of the data misfit
K	Number of repetitions of sampling in the DPS
m_{opt}	Solution vector of slip on TDEs
$M_{ring/sill}$	Number of TDEs in the mesh of the ring-faults/sill
N_{sub}	Number of subsampled points
S	Total sensitivity of the full data set with respect to a given input model
ADM	**A**pproximate **D**eformation **M**odel
B	Performance of a subsampled data set $\mathbf{d}_{sub}$
BEM	**B**oundary **E**lement **M**ethod/**M**odel
BEM	**F**inite **E**lement **M**ethod/**M**odel
CUD	**C**omplete **U**nwrapped **D**ata set
DD	**D**islocation **D**iscontinuity
DEM	**D**igital **E**levation **M**odel
DFG	**D**eutsche **F**orschungs**G**emeinschaft

DPS	**D**esigned **P**ixel **S**ubsampling
ENVISAT	**ENVI**ronmental **SAT**ellite
GA	**G**enetic **A**lgorithm
InSAR	**In**terferometric **SAR**
Landsat TM	Landsat Thematic Mapper: multispectral mapping satellite
LOS	**L**ine-**O**f-**S**ight of the radar satellite
M.Sc.	**M**aster of **Sc**ience
MERIS	**ME**dium **R**esolution **I**maging **S**pectrometer
MODIS	**MOD**erate-resolution **I**maging **S**pectroradiometer
ODM	**O**ptimum **D**eformation **M**odel
QTA	**Q**uad**T**ree **A**lgorithm
RMSE	**R**oot **M**ean **S**quare **E**rror
SAR	**S**ynthetic **A**perture **R**adar
SBAS	**S**mall *BA*seline **S**ubset
StaMPS	**Sta**nford **M**ethod for **P**ersistent **S**catters
TDE(s)	**T**riangular **D**islocation **E**lement(s)
TSX	**T**erra**S**AR-**X** - High resolution german radar satellite
UTM	**U**niversal **T**ransverse **M**ercator coordinate system

1. Introduction

1.1. Motivation

Surface displacement, degassing, seismic activity and other changes are very often precursors for upcoming eruptive events at volcanoes. Consequently, the monitoring of these allows to assess the state of activity at volcanoes. If this is done continuously, the "character" of the monitored volcano can be studied and understood. In this way the behavior of well instrumented volcanoes may be sometimes forecasted very well. For example 250,000 people have been evacuated before the eruption of Merapi in October 2010. So there were just few fatalities to be bewailed, compared to the size of the eruption (VEI=4) (Surono et al. 2012).

On the other hand, there are still very often other unpredictable occurrences. An eruption of the well monitored Eyjafjallajökull in April 2010, for instance, was expected after the observation of strong surface displacement and seismic activity (Sigmundsson et al. 2010). Although forecasted in advance, this comparatively small eruption (VEI=3-4) (Simkin and Siebert 2013) had an unexpectedly large impact on the air-traffic all across Europe, causing a significant economic loss.

As each volcano is unique in its behavior, we do not know what impact a major or even just a minor eruption of an unknown or a barely studied volcano may have on the human society. It is too costly nowadays to equip all ~ 1500 potentially active volcanoes (Simkin and Siebert 2013) with dense instrumentation for a close monitoring of their behavior.

Nevertheless, the development of satellite-based synthetic aperture radar interferometry (InSAR) in the 1990s has allowed investigating the surface displacement at the Earth from space. In this way, several previously unknown volcanically active regions were detected, as the first large scale surveys have been conducted, e.g. the Lazufre volcanic field in the South Andes, Aleutian volcanoes and volcanoes in the East-African rift (Pritchard and Simons 2002, Lu 2005, Biggs et al. 2009). InSAR is especially invaluable to investigate some very remote or politically unstable areas that are difficult to access. Two volcanoes, which I have investigated within this thesis are located in such areas, Llaima in Chile and Tendürek in Turkey.

Little is known about the type and source of crustal deformation at these volcanoes. As later on shown in my thesis, the investigated displacement patterns at Llaima volcano are changing in time, with in- and deflating sources at different depths. Moreover the displacement is complex in space at Tendürek volcano as well, where a contracting sill caused local reactivation of ring-faults. Hence both case examples reveal unique source interactions in time and space, as well as the difficulty to apply the so far widely used simple source models to explain the processes at the volcanoes.

1.2. Volcanic deformation processes

Displacement at the surface of active or even dormant volcanoes is usually related to subsurface magmatic, tectonic, hydrothermal or gravity-driven processes.

Magmatic processes are related to movement of magma within the upper crust. The intrusion of dikes, sills and the accumulation of fresh magma inside a magma chamber may cause an inflation or an uplift of the the Earth's surface (Dzurisin 2007). Magma withdrawal, cooling contraction and crystallization of old magma cause deflation (Dzurisin et al. 2002). A magma chamber is presumed to be a zone of storage for (partially) molten rock, which is not necessarily composed of one large liquid magma body (Parfitt and Wilson 2008). It is more obvious a sponge-like zone with pores of molten rock.

Tectonic processes are related to displacements along faults. Typical faults at volcanoes are especially ring-faults that usually surround calderas, the large crater structures of collapsed volcanoes (Anderson 1936). The flanks of a volcano might be unstable due to underlying weak material or because of a detachment fault. Therefore, a volcano flank might be moving laterally along radially oriented fault systems from the summit. This process leads to the spreading of the volcanic edifice (Ruch et al. 2012) and may even result in a collapse of the respective flank, which may lead to increased magmatic activity in turn (Manconi et al. 2009). If the basement below the volcano consists of weak material, the whole edifice might spread and sag gravity-driven into the soft substratum (Shirzaei et al. 2011, Byrne et al. 2013).

Displacement at surface, caused by hydrothermal activity, is related to migration of fluids within the crust. A magmatic intrusion is associated with the release of volatiles or "steam" ($CO_2, H_2S, SO_2, ...$). If these are trapped in the subsurface below the ductile-brittle transition zone, they will increase the pressure on the surrounding host rocks in conjunction with the magma. This will cause inflation or uplift at the Earth's surface (Fournier 1999). If the volatiles can find ways to the surface they will be cooled down and partially condensed to fluids. The consequence of it is a reduction of volume, therefore a reduced pressure on the surrounding and the hydrothermal system. This will cause deflation or sinking of the volcanic edifice (Fournier 1999).

Some of the fluids might stay liquid within the crust, they cool down and migrate deeper into the crust again, forming a convection cell above and around the magma chamber (Dzurisin 2007). On their way the fluids can dissolve various minerals and therefore alter the chemical composition of the host rocks to potentially weaker material. This allows easy deformation and compaction, i.e. subsidence at the surface (Cecchi et al. 2004).

All of these processes are naturally connected and a combination of several of those is expected to act within a volcano. However, it is difficult to distinguish between the different source processes heretofore.

1.3. Methods

1.3.1. Synthetic Aperture Radar (SAR) Interferometry

Synthetic Aperture Radar (SAR) data is the backbone of this thesis and all the analyses and interpretations are based on the observed surface displacement at the investigated volcanoes. The basic principles of the data processing for interferogram formation and post processing have been explained in detail several times (Hanssen 2001, Massonnet and Souyris 2008). In the following section I will therefore shortly summarize the most important aspects.

A radar satellite flies continuously on a polar orbit around the Earth and transmits electromagnetic waves towards the Earth's surface. The amplitude and phase values of the reflected waves are stored as complex numbers in SAR images. With repeating passes of the satellite, several acquisitions from slightly different viewing angles are obtained over a certain area of interest. The subtraction of the phase of one radar acquisition from the phase of another acquisition yields an interferogram. There are several factors that influence the phase of an interferogram:

$$\phi_{ifg} = \phi_{defo} + \phi_{topo} + \phi_{orb} + \phi_{atm} + \phi_{noise} \tag{1.1}$$

where ϕ_{defo} is the phase change at the Earth's surface caused by a deformation source in the subsurface that we want to investigate. ϕ_{topo} is the phase change due to topographic height of the surface, which increases linearly with larger differences between the viewing angles of the acquisitions. ϕ_{orb} is the phase change caused by inaccurate description of the satellite orbit. ϕ_{atm} is the phase change caused by layers of water vapor in the atmosphere.

Finally, ϕ_{noise} is phase change due to various sources of noise, e.g. radar system noise.

To extract ϕ_{defo} from the interferograms and to correct for the other phase components requires several extra processing steps. Nowadays ϕ_{topo} can be corrected by using a digital elevation model (DEM), which I did by using the SRTM data set (Farr et al. 2007). ϕ_{orb} usually exists in the form of a phase ramp throughout the whole image. If there is no long-wavelength displacement present in the interferogram, this can be approximated with a quadratic plane (Hanssen 2001). The data set of the descending track over Tendürek volcano showed a peculiarly strong orbital ramp that I corrected by using the mentioned approach.

Presumably the most common way to correct the atmospheric phase delay ϕ_{atm}, is to add the phase of several interferograms, i.e. “stacking” (Samsonov 2010). Usually the phase change due to a certain deformation process is somehow coherent in time, whereas atmospheric phase delay is turbulent and therefore reduced. Alternative ways would be to use either meteorological data like Meris and MODIS, weather models (Jolivet et al. 2011) or GPS data (Onn and Zebker 2006) and based on that, to correct for the atmospheric phase change (Hanssen 2001). However, the first methods have been proven to be only partly successful. As for GPS, it is often not available, as in the case of my investigated volcanoes. The correction of atmospheric phase delay is a major issue up to now, and it has not been completely solved yet, which is why this limitation is extensively discussed within the several upcoming chapters and the appendix of this thesis.

The quantity of radar acquisitions over some regions of the Earth was continuously increasing and this lead to the development of various time series methods in the last decade (Ferretti et al. 2001, Berardino et al. 2002, Hooper et al. 2007, Shirzaei 2013). These methods aim to combine numerous interferograms to produce maps of even temporal surface displacement. Besides spatial phase filters, it enables to use temporal phase filters and increases the signal-to-noise ratio significantly, as a result. Hence, surface displacements can be measured by even millimeter accuracy (Ferretti et al. 2007).

1.3.2. Assessment of the deformation source through modeling

The measured displacement at the Earth surface, which is in our cases observed around the summit of volcanic edifices, can be used to infer the parameters of its deformation source (Dzurisin 2007). To do that we have to make assumptions about the subsurface medium.

The simplest and most widely used model setup is an analytical deformation source within a homogeneous elastic halfspace. The most often used analytical sources at volcanoes range from a simple point pressure source (Mogi 1958), over a spherical (McTigue 1987) to an ellipsoidal pressure source (Yang et al. 1988). They are meant to resemble a natural magma chamber, where a rectangular dislocation plane (Okada 1985) simulates magmatic sills and dikes, as well as fault planes. These models are not very realistic in nature; nevertheless they have proven to be useful in countless studies for the rough estimation of first order deformation source geometries and locations. In the following chapters I used the models of Mogi, Okada and Yang to explain the observed surface displacements at Llaima and Tendürek.

However, if there is complementary information available, it may be incorporated as additional constraint for more complex models by using the boundary element method (BEM). This information can be, for example, a 2-D seismic wave velocity profile of rocks in the underground, a DEM that allows to resemble elevation changes in the area of interest or the shape of complex sources, such as curved faults (Cayol and Cornet 1997). All these constraints are combined into linear integral equations and solved for the boundary conditions, e.g. the traction on the deformation source. A more detailed description of the boundary element method is given in **chapter 4**, where I use it to produce a detailed source model of Tendürek volcano.

After setting up the model space, an automatic search algorithm can be used to find the source parameters of the deformation source of interest (Sambridge and Mosegaard 2002). If the synthetic displacement of the forward model matches the observed displacement data, the search can be considered as successful. However due to the limited available data, the quality of the data and the nature of the highly non-linear inverse problem, there are usually large parameter ambiguities (Sudhaus and Jónsson 2009). Therefore, it is important to estimate model parameter uncertainties in order to interpret the final result properly. The search algorithm I have used in the optimizations and the estimation of source parameter uncertainties are explained in detail in **chapter 3**.

1.4. Field areas

The study areas of my work are situated at very different parts of the world, in different geodynamic settings. I investigated the very remote volcanoes Llaima and Tendürek. Llaima volcano in Chile is well known and Tendürek volcano in eastern Turkey is relatively unexplored. Both volcanoes are very difficult to access and poorly instrumented. Hence, there is very little known about their magma-plumbing systems.

The volcanoes differ in their structure, shape eruption style and composition. However, a striking similarity is that both of them show surface displacement, associated with interacting complex deformation sources. Remote sensing in the form of optical and radar images, is a perfect tool for monitoring these volcanoes. It allows investigating the displacement field below the volcanic edifices and consequently the deformation sources and plumbing systems.

1.4.1. Chile

The subduction of the Nazca Plate below the western margin of the South American Plate is the driving force for the uplift of the South Andes mountain range. If the subduction angle of the Nazca plate is high (>25°), dehydration and melting of the subducted plate will produce magmas that may migrate towards the Earth surface. At low subduction angles (<10°) less or no melts are produced, because the temperature and dehydration are not high enough (Stern 2004). Accordingly to the subduction angles, all along the Southern Andes mountain range, there have been several regions developed with strong volcanism interleaved by zones with no volcanism. These are the Northern Volcanic Zone, the Central Volcanic Zone, the Southern Volcanic Zone and the Austral Volcanic Zone.

Llaima volcano

I have investigated Llaima volcano that is part of the Southern Volcanic Zone. It is one of the most active volcanoes in the South Andes with over 50 eruptions from 1640 until today (Dzierma and Wehrmann 2010). It is a holocene steep strato-volcano of andesitic-basaltic composition (Naranjo and Moreno 1991) with various eruptive styles in the past. Initially of effusive type, it has changed to plinian and again to the nowadays hawaiian and strombolian type (Naranjo and Moreno 1991).

From November 2008 to April 2011 a temporary network has been installed at Llaima by the scientists from the University of Kiel, in addition to the few permanent stations of the South Andean volcano observatory (OVDAS) (Mora-Stock et al. 2012). During that period of observation, Llaima has been showing a sustained activity in tremor and in long-periodic events, which both are characteristical either for the movement of gas and fluids, or magmas through the crust. The volcano-tectonic activity has been increasing drastically within three days after the Maule earthquake from the 27. Feb 2010 (Mora-Stock et al. 2012). However, the events have not been located precisely and therefore; neither they allow any interpretation on magma-pathways nor on the position of a magma chamber below Llaima.

Recent petrological studies of the eruptive products at Llaima show that magmas are stored at shallow depth ($\leq 4\,\mathrm{km}$), before an eruption occurs (Bouvet de Maisonneuve et al. 2012b). This shallow reservoir might be recharged with magmas from a deeper reservoir. Dependent on the amount of the recharged magma and thus on the volatile content, the eruptive style would be changed. It would be more explosive with large magma recharge and more effusive with low magma recharge (Bouvet de Maisonneuve et al. 2012a).

My InSAR results display a period of subsidence at Llaima volcano from November 2003 to April 2007 that has been followed with a period of uplift until November 2008. Analytical source modeling of these signals (chapter 2, table 2.1) show two depth ranges: 6-12 km for the deflation source and 4-9 km for the inflation source (Fig. 1.1). In comparison to the petrological studies presented above, it seems like the shallow reservoir has been recharged with magma from the deeper reservoir.

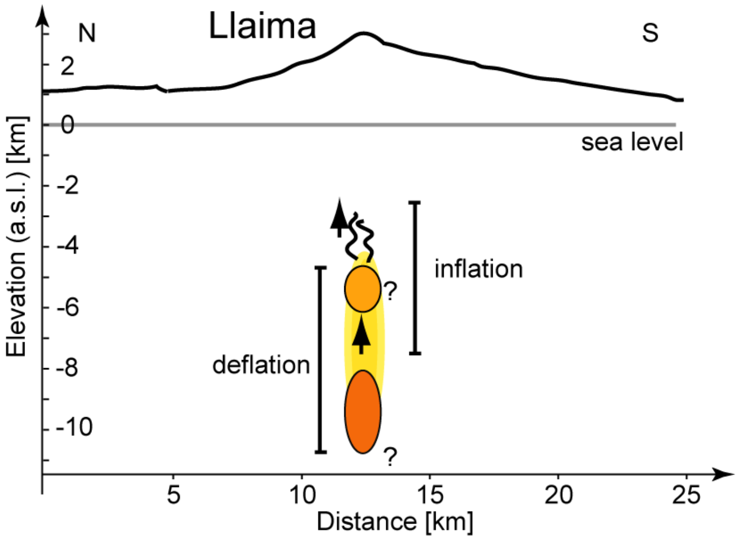

Figure 1.1.: Schematic model of Llaima volcano, vertically exaggerated by 1.33. The colored ellipses show the possible extent of the magma chamber(s) based on the inversion results in chapter 2, table 2.1. The vertical black lines mark the extent of the confidence intervals.

1.4.2. Turkey

The volcanism in Eastern Anatolia has started with the onset of the collision of Arabia with Eurasia between 40 and 12 million years ago (Pearce et al. 1990). In this region the magma is not generated by melting and dehydration of oceanic crust as described above. Instead, the continent-continent collision causes the continental lithosphere to be thickened and thus to sink deeper into the asthenosphere (Pearce et al. 1990). An additional upwelling of asthenosphere is caused by lateral stress release in the continental lithosphere due to east-west directed extension. This extension is a result of the westward movement of the Anatolian plate, in response to the north-south directed compression (Reilinger et al. 2006). High temperature in the deep reaching lower crust causes as a result, a partial melting of the lower lithosphere (Pearce et al. 1990). These melts then move towards the Earth's surface, where they cause the volcanism all along the continental collision zone.

The region of Eastern Anatolia is tectonically highly active with its countless faults and volcanoes (Karakhanian et al. 2002). The predominant volcano types in Eastern Anatolia are strato- and shield-volcanoes (Yılmaz et al. 1998). Some of those have developed calderas (Nemrut) or are in the state of caldera formation (Tendürek). The magmas at these volcanoes have a large variety (basic-acidic) and change in composition from volcano to volcano significantly: basaltic-trachytic (Tendürek), andesitic-dacitic (Ararat), trachytic (Nemrut), rhyolithic-andesitic (Süphan) (Yılmaz et al. 1998). These compositions reflect how the lithospheric mantle magmas have individually assimilated the respective crustal host rocks, during their ascent below each volcanic center (Yılmaz et al. 1998). Thus, the magmas erupted at Tendürek show little influence of the continental lithosphere.

Tendürek volcano

Tendürek is located in between two dextral NW or WNW oriented strike-slip faults. It is an elliptically shaped shield-volcano of mainly basaltic magma composition (Yılmaz et al. 1998). A detailed overview of the tectonic setting and geology of the volcano is given in chapter 3. There has been no detailed geophysical study conducted at Tendürek so far and it remains unknown whether there were any seismic activity at the volcano.

I have used several SAR scenes from both, ascending and descending viewing geometries of the Envisat satellite, to extract two time series of displacement from 2004 to 2008 and from 2003 to 2010, respectively. The data show that the volcanic edifice is subsiding with a rate of 1 cm per year continuously. A contracting sill 2 km below the sea level can explain the major part of the observed displacement signal (Fig. 1.2). The displacement data and independent optical images make clear, there are active arcuate fractures surrounding the volcanic edifice, which are most likely the surface expressions of a ring-fault.

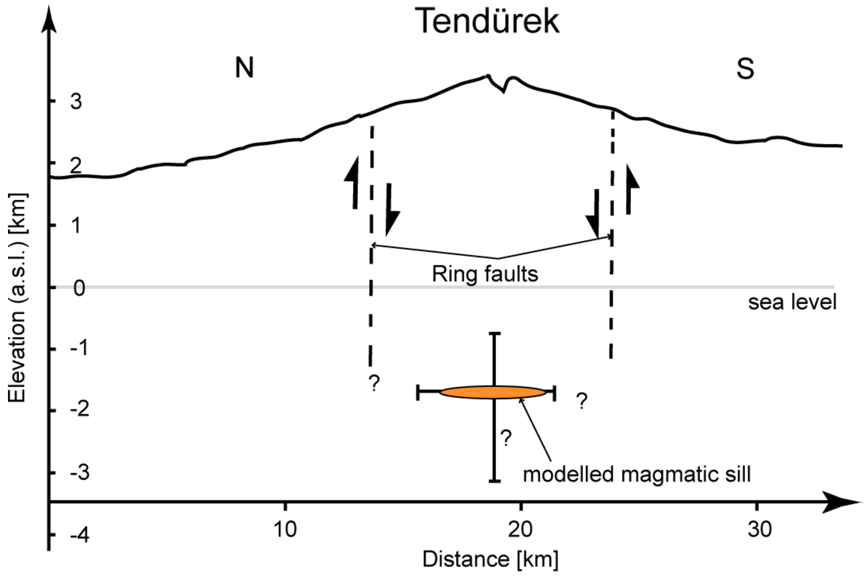

Figure 1.2.: Schematic model of Tendurek volcano, vertically exaggerated by 2.66. The colored ellipse shows the the magmatic sill based on the inversion results in chapter 3, table 3.2. The vertical and horizontal black lines mark the extent of the confidence intervals. The vertical dashed lines show the inferred location of the ring-faults.

1.5. Thesis Organization

This thesis consists of four manuscripts that are summarized in the upcoming subsections. My general conclusions and an outlook on the implications of the findings of the manuscripts are given in the end.

1.5.1. Inflation and deflation at the steep-sided Llaima stratovolcano (Chile) detected by using InSAR

In **chapter 2** we have been investigating Llaima volcano, where we used simple 2-pass radar interferometry to create interferograms. The standard phase unwrapping procedures however failed, because of the low signal-to-noise ratio in the data. Therefore, we have developed a model-assisted phase unwrapping procedure to generate the displacement maps. They show post eruptive deflation of maximum 10 cm from November 2003 to April 2007 that is followed by a maximum inflation of 8 cm until November 2008.

These displacements can be modeled with a contracting and expanding point pressure source at a depth of 6 - 12 and 4 - 9 km, respectively. This might imply the presence of more than one magma reservoir below Llaima. Before the eruption of the volcano, the magma may have ascended from a deep reservoir into a shallow one.

Author contributions: Bathke processed the data and did the source inversions. Bathke and Shirzaei developed the modeling scheme and wrote the manuscript under the supervision of Walter. All of the authors contributed to the interpretation of the data and the modeling results equally.

This chapter has been published in *Geophysical Research Letters*:

Bathke, H., Shirzaei, M. and Walter. T. R.: 2011, Inflation and deflation at the steep-sided Llaima stratovolcano (Chile) detected by using InSAR, *Geophysical Research Letters* **38**(10),1-5. **URL**:*http://www.agu.org/pubs/crossref/2011/2011GL047168.shtml.*

1.5.2. An active ring fault detected at Tendürek volcano by using InSAR

At Tendürek volcano, in **chapter 3**, we have found a steady subsidence signal over the years 2003-2010, investigating two displacement time series of both radar viewing geometries. By using deformation source modeling, we have found that the observed signal can be explained largely with a contracting magmatic sill-like source in 4.5 km depth below the volcano summit. Moreover, with high resolution optical satellite data we have found this deformation source to exist in conjunction with active, very slowly slipping ring faults around the volcano, which is a unique observation so far.

Author contributions: Bathke processed the data and did the source inversions. Bathke, Sudhaus and Holohan wrote the manuscript. Holohan and Walter contributed to the investigation with the geological interpretations. All of the authors interpreted and discussed the modeling results and the results of the data analysis.

This chapter has been published in *Journal of Geophysical Research: Solid Earth*:

Bathke, H., Sudhaus, H., Holohan, E., Walter, T.R. and Shirzaei, M.: 2013, An active ring-fault detected at Tendürek volcano by using InSAR, *Journal of Geophysical Research: Solid Earth* **118**(July), 4488-4502. **URL**:*http://doi.wiley.com/10.1002/jgrb.50305.*

1.5.3. A 3D boundary element model of ring-faulting at Tendürek volcano

In **chapter 4** we have used the boundary element method, to be able to create more complex source models of the subsurface structure at Tendürek volcano. The linear displacement velocity of two time series of displacement 2004-2008 and 2003-2010 from the ascending and descending ENVISAT satellite tracks have constrained our models, respectively. We have incorporated a contracting sill-like source with inward/outward inclined ring-faults under the consideration of true topography and the interaction of the sources into a model. After initial determination of the general geometry of the sources, we have inverted for distributed slip on the ring-faults and for distributed opening on the sill-like source.

The model results show that the underground structure at Tendürek most likely consists of a contracting sill-like source at a depth from -2.7 to -3.1 km, which is the driving force for slip on the ring-faults encircling the volcanic edifice. In comparison to results of analog experiments from Holohan (2008), which resemble the natural situation at Tendürek, it seems to be plausible that the ring-faults on the western flanks of the volcano are outward inclined reverse. In contrast to that, inward inclined normal faults at the eastern volcano flanks are most reasonable.

This setup of interacting source resembles a natural sliding trapdoor faulting mechanism in nature that has been proposed from the results of analog and numerical models by (Holohan et al. 2013).

Author contributions: Bathke processed the data. Bathke and Nikkhoo did the modeling. Holohan contributed to the interpretation of the modeling results and provided fig. 4.7. Bathke wrote the manuscript under the supervision of Walter.

1.5.4. Data subsampling for source modeling

In **chapter 5** we have developed an alternative subsampling method for the reduction of heterogeneously distributed time series data. This approach is a modified version of the model-based method from Lohman and Simons (2005). We have applied our method to synthetic data and time series data at Tendürek (Bathke et al. 2013) and have compared its performance to the Quadtree algorithm (Jónsson et al. 2002). We consider our approach to perform at least as well as the Quadtree algorithm and to improve the feasibility of the propagation of data-errors to model uncertainties futhermore.
Author contributions: Bathke did the synthetic test and the source inversions. Bathke and Shirzaei developed the modeling scheme. Bathke and Sudhaus wrote the manuscript under the supervision of Walter. All of the contributing authors discussed the modeling results.

1.5.5. General Discussion and Outlook

In conclusion all the major findings of this thesis are summarized in **chapter 6**. These cover the technical advancements have been made, the general progress in geophysical understanding of volcano deformation patterns and the complexities in their sources. This is followed by a discussion of further monitoring necessities, which are required to gain even deeper insights into the investigated subsurface processes.

2. Inflation and deflation at the steep-sided Llaima stratovolcano (Chile) detected by using InSAR

H.Bathke[1], *M.Shirzaei*[1,2], *T.R.Walter*[1]

(1): Department 2: Physics of the Earth, Helmholtz-Centre Potsdam, German Research Centre for Geosciences (GFZ), Potsdam, Germany.

(2): now at Dept. of Earth and Planetary Science, Univ. of California, Berkeley, USA

2.1. Abstract

Llaima volcano, Chile, is a typical basaltic-to-andesitic stratovolcano in the southcentral Andes. Llaima had at least four explosive eruptions in the decade 2000 - 2010, however little is known about the physical processes and magma storage at this volcano. In this study we present an InSAR deformation field at Llaima from 2003 - 2008, covering both the post-eruptive and syn-eruptive periods. The satellite InSAR data are significantly affected by environmental decorrelation due to steep topography, snow and vegetation; because of this, we applied a model-assisted phase unwrapping approach. The analysis of these data suggests two main deformation episodes: subsidence associated with the post-eruptive period, and uplift associated with the syn-eruptive period. Maximum summit subsidence and uplift are 10 cm and 8 cm, respectively. Through inverse modeling of both periods, a deflating and inflating magma body can be inferred, located at a depth of 4 - 12 km, subject to a volume decrease of $10 - 45 \cdot 10^6\, m^3$ during the subsidence period, followed by a volume increase of $6 - 20 \cdot 10^6\, m^3$ during the uplift period. Therefore, this study presents the first evidence of magma-driven deformation at Llaima volcano, and suggests that eruption periods are associated with the inflation and deflation of a deep magma body that can be monitored by using space geodesy. Keywords: Llaima, InSAR, phase unwrapping, open volcano, monitoring

2.2. Introduction

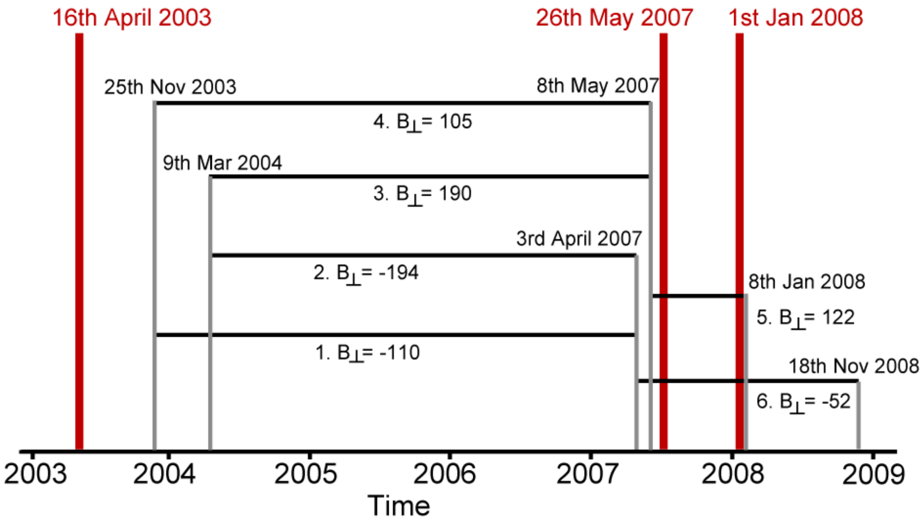

Figure 2.1.: The timing of the eruptions are marked by the red lines and the generated interferograms are shown with the black lines with their according perpendicular baselines in [m]. The end points of the black lines are associated with the acquisition time of the master and slave images.

Llaima is one of the largest and most active volcanoes in the southern volcanic zone of South America, being a Holocene steep basaltic-to-andesitic stratocone with an edifice height of 3,125 m and a volume of about 400 km^3 (Naranjo and Moreno 1991). The eruptive history of the volcano is of mainly Strombolian and Hawaiian type, however, intermittent sub-plinian activity poses a high hazard potential, including pyroclastic flows, air-falls and remobilization of material in the form of lahars (Naranjo and Moreno 1991).

Recent eruptions have occurred in 2002 and 2003, followed by a 4-year period of silence, and further eruptions again throughout 2007-2009; each eruptive period had individual phases of activity and quiescence (Simkin and Siebert 2013). There is a high probability of another imminent eruption (Dzierma and Wehrmann 2010). As there is only minor vulnerability in the poorly populated and hardly accessible region, only sparse monitoring networks have been installed until recently (Galle et al. 2010). Therefore, although being so prominent and well known volcanically, the physical processes of the magma supply at Llaima and its plumbing system are poorly understood. No magma chamber has been constrained so far, which would allow design and adjustment of monitoring networks.

As we show herein, satellite data could provide one of the most important information sources. The space-borne synthetic aperture radar (SAR) technique is one of the few methods that enables us to look back in time and study deformation occurrence at Llaima volcano. Using interferometric SAR data, Fournier et al. (2010) identified a slow landslide at the eastern flank of Llaima. Association of the observed eruptions with deformation activity was not detected however, mainly because of temporal and spatial radar signal decorrelation.

In this study we analyze a set of InSAR data and apply a model-assisted phase unwrapping and modeling approach to characterize the source of the deformation field based on noisy interferometric data sets. This approach allows us to identify two periods of activity: subsidence between 11/2003 and 05/2007 and uplift from 05/2007 until 11/2008. These periods of observation were preceded by a volcanic crisis on 04/16/2003 and included two other episodes of volcanic activity starting on 05/26/2007 and 01/01/2008 Fig. 2.1. Through inverse modeling of the observed deformation data we constrained the magmatic source strength underneath the volcano. This provided the first evidence of magma-driven deformation at Llaima volcano prior to, and after, volcanic crises.

2.3. Remote Sensing Data Set

We firstly considered Landsat data to obtain a general overview of the study area. Figure 2.2 shows a Landsat TM image acquired in 1987, represented in band 432 false color. The color red in the image indicates vegetation, white shows snow and dark grey indicates exposed rocky surfaces. The snow-capped summit and the vegetated apron are clearly visible. In comparison with geologic lithologies (Naranjo and Moreno 1991), the greyish colors in the Landsat image correlate with mainly historical lahars and pyroclastic flow deposits, and these may be the regions where InSAR works best.

We considered InSAR results that were derived from a SAR data set acquired by the ENVISAT satellite. We have chosen these data because ENVISAT acquired multiple images from the same viewing geometry over Llaima volcano before the year 2007. The data were acquired between 11/25/2003 and 11/18/2008 in descending orbit from track 10 in I2 mode.

The interferometric processing of the radar data set was done using the freely available RoiPac processor provided by JPL (Rosen et al. 2004). The geometric phase was calculated and subtracted using satellite ephemeris data and a reference digital elevation model (DEM), obtained by shuttle radar thematic mapper (SRTM) at 90 m resolution. After estimating the phase coherence, each differential interferogram in Fig. 2.2, was filtered using an adaptive filter coefficient of 0.5 (Goldstein and Werner 1998). The interferograms, after further investigation are shown in Fig. 2.2, revealing several fringes at the volcano

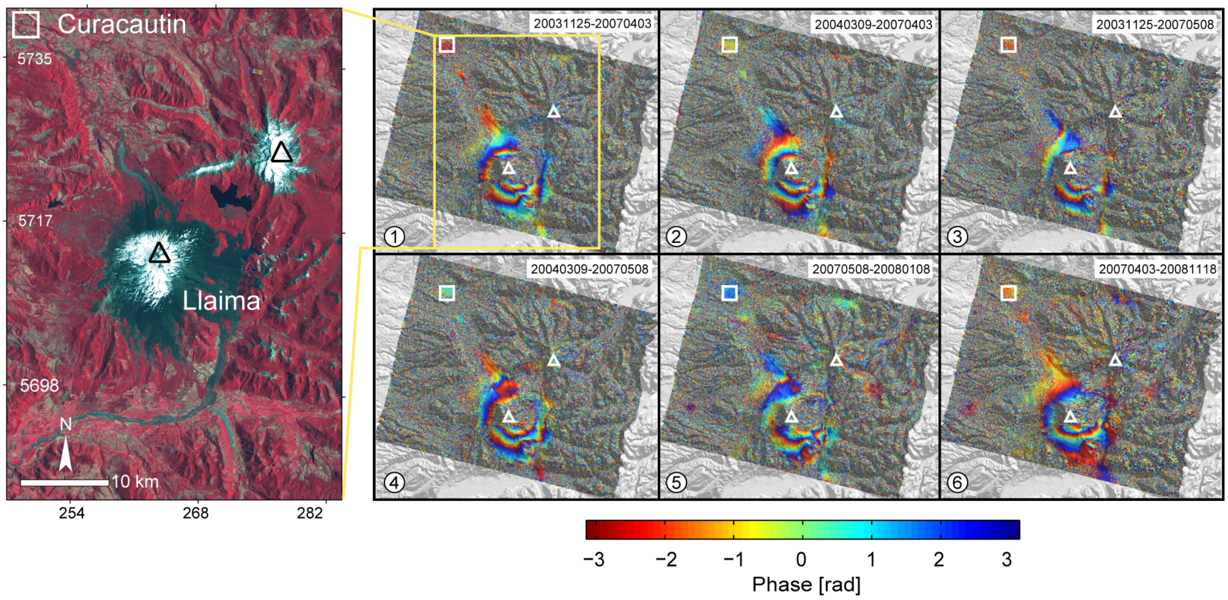

Figure 2.2.: Left: Landsat TM image from 1987-01-15 at Llaima volcano in false color where the red, green and blue channels are the bands 4, 3 and 2, respectively. Red color in the image indicates vegetation, white color shows snow and dark grey colors indicate exposed rocky surfaces, here mainly historical lahars and pyroclastic flow deposits. Right: Selected interferograms at Llaima volcano. High coherence is shown only in those areas where no snow or vegetation is seen. Curacautin city (white rectangle) is at approximately 30 km distance from the Llaima summit. White triangles depict the summit craters of the active Llaima and the dormant Sierra Nevada stratovolcanoes.

edifice, yet illustrating the prevalence of areas affected by significant phase decorrelation (hereafter referred to as noise).

Significant noise is affecting the InSAR pixels close to the summit. The extent of snow and glaciers is well in agreement with the extent of noise at the elevated regions in the interferograms (see comparison of the InSAR data to Landsat data in Fig. 2.2). Moreover, the areas of dense vegetation at the lower aprons and surroundings of Llaima volcano (reddish colors in Fig. 2.2a) are also affected by noise in the InSAR data. In contrast, InSAR provides reasonable data quality at regions where recent volcanic products have been emplaced.

Therefore, comparison of the InSAR and Landsat data shows that the InSAR data are heavily affected by phase decorrelation due to vegetation, and snow cover. Furthermore, decorrelation due to topography is common at many other steep-sided strato-volcanoes elsewhere, and so the InSAR method could be deemed ineffective (Pinel et al. 2010). In the following section we outline how we applied a phase unwrapping and inverse modeling approach to obtain unambiguous displacement data with the aim of retrieving further information about the source of the deformation field at Llaima volcano.

2.4. Modeling Strategy

Estimating the location and temporal change of a deformation source is one of the major tasks in volcano geodesy (Dzurisin 2007). The quality of source model parameters however, is strictly related to the quality and spatial distribution of the data sets (Shirzaei and Walter 2009). The requirement for further InSAR data handling is that the phase difference between two neighboring data points is less than pi. Significant decorrelation reduces the spatial sampling (i.e. the number of pixels) and therefore introduces spatial aliasing errors. The aliasing error may be reduced by decreasing the amplitude of the phase changes throughout the interferogram (Feigl and Thurber 2009). This we performed by subtracting the phase contribution of an approximate deformation model (ADM) (e.g. Mogi-type source after (Mogi 1958) from the wrapped filtered data. In this way, although the sampling rate remains low, the phase difference between neighboring data points is less than pi over most of the data set, which allows the application of a reliable phase unwrapping.

To obtain the ADM, we inverted the wrapped filtered data following Feigl and Thurber (2009) by using the genetic algorithm (GA) presented in Shirzaei and Walter (2009). We adapted it in such a way that the modeled deformation ΔR_{mod} is converted to the modeled unambiguous phase $\psi_{mod} = \frac{4\pi}{\lambda}\Delta R_{mod}$ (Hanssen 2001). By applying the modulus function

$\phi_{mod} = mod\left(\psi_{mod} + \pi, 2\pi\right) - \pi$, the modeled unambiguous phase ψ_{mod} was converted to a modeled wrapped phase ϕ_{mod}. The phase residual θ between the observed wrapped filtered phase ϕ_{obs} and the modeled wrapped phase ϕ_{mod} defined the cost in the GA and was minimized following L1 - norm: $\Theta = \left|wrap\left(\psi_{obs} - \psi_{mod}\right)\right|$. For the wrapping operator we used the modulo function described above, i.e. $\phi_{mod} = mod\left(\phi_{obs} - \phi_{mod} + \pi, 2\pi\right) - \pi$. After subtracting the ADM, we used the minimum cost flow algorithm (Chen and Zebker 2001), which is an L1- norm minimization approach (Ahuja et al. 1993), for unwrapping the residual phase values θ . The complete unwrapped data set was obtained by restoring the ADM to the unwrapped residual phase values. Finally, we computed the source parameters of the deformation field by applying GA to the complete unwrapped data (CUD) set, by using a similar inversion approach as mentioned above.

2.5. Application to Llaima volcano

In this section we present the pair that spans the period 11/25/2003 - 05/08/2007; results summarizing the analysis of the other interferograms (Fig. 2.2) are shown in the supplementary online material provided. Let's consider only pixels with a phase coherence above 0.24, which provides us with about 25,000 useful data points (see interferogram in Fig. 2.3a). The data shows a pronounced phase gradient approximately centered at the volcano. Moreover the area of phase decorrelation is visible on the base and the flanks. The ADM obtained by inverting this interferogram is given in Fig. 2.3b. To calculate the residual phase (Fig. 2.3d) we set a lower phase coherence threshold (0.17). This provided us with a larger group of pixels (Fig. 2.3c) which may be more affected by phase noise. This step-wise increase in observation points did not lead to significant global unwrapping errors (Marshall and Bethel 1996), since we used an L1 norm minimization approach for phase unwrapping (Constantini 1998) and we reduced the spatial aliasing by removing the ADM. Hereafter we unwrapped the residual phase and restored the ADM, so that eventually the complete unwrapped data set was obtained (Fig. 2.3e). As a test, we unwrapped the filtered interferograms without removing the ADM and noted significant unwrapping errors.

As applied below for the Llaima data set, this set can be further used for final deformation source modeling. We initialized GA with a population size of 80, a selection rate of 0.5, a mutation rate of 0.6 and with 300 iterations (further details on implementation of GA are given in (Shirzaei and Walter 2009)). The obtained model result is presented in the optimum deformation model (ODM) and the residual, can be explained as the subtraction of

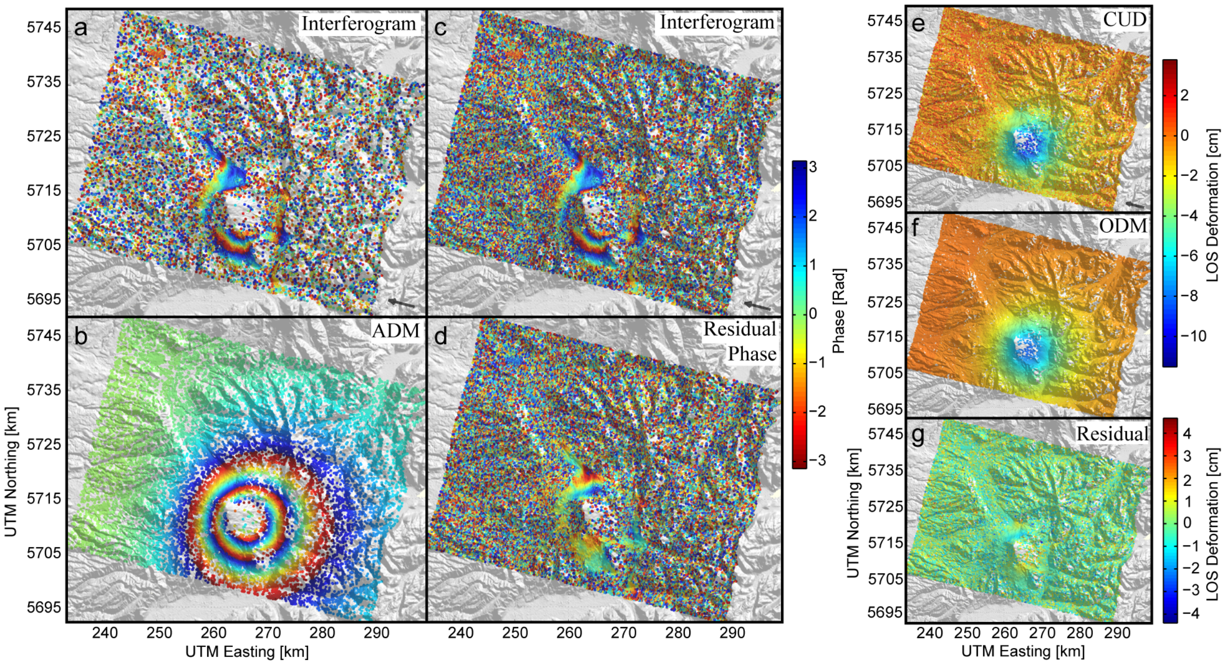

Figure 2.3.: InSAR data and source modeling results at Llaima volcano, illustrated for one of six interferograms (here SAR scene pair 2003-11-25 and 2007-05-08). a: Observed wrapped phase data with coherence threshold of 0.24. b: Synthetic phase data from the approximate deformation model (ADM). c: Observed wrapped phase data with coherence threshold of 0.17 from the same SAR scenes as part a. d: Phase residual between observed wrapped phase data with low coherence (c) and synthetic phase data from the ADM (b). e: Line of sight deformation (LOS) of the complete unwrapped data set (CUD). f: Synthetic LOS deformation for the optimum deformation model (ODM) for the CUD (e). g: LOS deformation residual between the CUD (e) and the synthetic LOS deformation for the ODM (f).

the true data from the model (Fig. 2.3f and 2.3g). These results show that the implemented unwrapping and modeling strategy is capable of retrieving a complete spatial deformation field at Llaima and enables investigation of the deformation source parameters.

2.6. Results

The unwrapped InSAR data set allows us to clearly identify and analyze two distinct periods of activity at Llaima volcano. A period of subsidence is sampled by the InSAR data acquired between 11/2003 and 05/2007. Then the InSAR data suggest a period of uplift, lasting at least until 11/2008. Given the available temporal sampling, the periods of subsidence and uplift are likely to be related to the eruptive episodes at Llaima. The period of subsidence occurred after the 04/2003 eruption, followed by uplift spanning the 05/2007 and 01/2008 eruptive episodes. We note that the sum of displacement estimated by adding both periods together is almost zero.

The result of applying the modeling method to the data set is provided in Table 2.1. The source parameters and associated uncertainties are estimated at a confidence level of 95%. For both the subsidence and the uplift periods, the magma body location is at an approximately stable position of 262.95 km and 5711.25 km, according to the UTM projection system (zone H19). Therefore the location is shifted slightly (~ 1 km) to the southeast with respect to the summit crater of Llaima. The position of the subsidence source is constrained at a depth of 6 - 12 km, whilst the uplift source is located at a somewhat shallower depth of 4 - 9 km. Therefore, although being located at similar depths within the ranges of uncertainty, the inflation source appears to be somewhat shallower. The volumes of the deflation and inflation periods are between $4.5 - 10 \cdot 10^6\, m3$ and $6 - 20 \cdot 10^6\, m^3$, respectively, and so the cumulative volume change at the location of the inferred magmatic source is minor over the entire observation period.

2.7. Discussion and Conclusion

Detection of volcano deformation is one of the most important sources of information for monitoring programs, yet to date it has had limited success, particularly at steep-sided andesitic or basaltic-to-andesitic volcanoes. Detection of deformation occurrence, and especially localization and quantification of potential magma reservoirs at depth, and their behavior, is of major relevance because these volcanoes commonly typify the most explosive form of volcanism.

	OPTIMUM SOLUTION		CONFIDENCE INTERVAL 95%	
DATES	$d[km]$	$\Delta V[km^3]$	$d[km]$	$\Delta V[km^3]$
1.20031125 – 20070403	6.8	-0.018	6.2- 9.6	-0.021, -0.01
2.20040309 – 20070403	9.9	-0.018	5.8- 10.2	-0.023, -0.013
3.20031125 – 20070508	9.9	-0.036	8.0- 12.0	-0.043, -0.025
4.20040309 – 20070508	9.7	-0.037	8.6- 12.1	-0.045, -0.028
5.20070508 – 20080108	6.2	0.012	5.3- 9.3	0.006, 0.02
6.20070403 – 20081118	5.1	0.007	4.1- 8.3	0.006, 0.014

Table 2.1.: Inversion results for a Mogi source for the interferograms shown in Fig. 2.1.

This work presents an InSAR and modeling study at Llaima volcano. Using a SAR data set of the Envisat satellite in descending orbit (Fig. 2.1), this work presents six interferograms. We note however, that a much larger SAR database is available. In total we processed 101 interferograms, but for most of the images phase decorrelation was too significant, as the two-pass interferometry could have allowed any interpretation. The application of standard-time series analysis was not feasible either, as it decreases the spatial coverage of the data significantly at steep-sided volcanoes, in such a way as to make it barely possible to observe the deformation signal related to magmatic activity (Pinel et al. 2010). So we focused on further investigating interferograms from 2-pass interferometry, because source inversions require a spatially dense data set (Shirzaei and Walter 2009).

We successfully adapted and applied a strategy that increases the accuracy of phase unwrapping. This work suggested the employment of a model-assisted unwrapping approach. Using this we found two episodes of subsidence and uplift at the volcano edifice, between 11/2003 and 05/2007 and 05/2007 till 11/2008, respectively. The poor temporal resolution may have been a drawback, as the apparent subsidence and uplift periods were temporally sampled only by a few interferograms each. Any short term variation below the sampling interval may have been missed using this dataset.

During the inverse source modeling we considered an inflating point source (Mogi 1958) buried in an elastic homogeneous half-space medium. This was only a rough approximation, where finite or more complex source geometries as well as surface topography and material heterogeneities were not considered. We note, furthermore, that some small and localized deformation might exist at the low-coherence areas at the volcano summit or flanks. This is not resolvable by our data and model. We nevertheless consider our use of such a simple model set-up to be a valid approach, because it allows us to explain the general pattern of the deformation signal. Moreover, use of a more complex model is hindered because very little is known about the deep-level mechanical properties and plumbing system geometry below Llaima. Furthermore, atmospheric delay in repeat pass interferometry (Goldstein 1995) may have obscured the deformation data, which we did try to overcome by comparing inversion results from several interferograms spanning each period. MERIS data resolution is insufficient to accurately estimate the atmospheric delay for this small area.

As a result of the inverse modeling procedure we found that the sources of subsidence and uplift are characterized by an absolute volume change rate of $3 - 13 \cdot 10^6\, m^3/yr$ and $9 - 30 \cdot 10^6\, m^3/yr$, respectively. Thus in spite of the occurrence of two eruptions during the uplift period, the Llaima inflation rate is still 3 times faster than the deflation rate, meaning that the magma supply to the reservoir is much faster than the magma withdrawal. This may mean that only relatively short pre-eruptive deformation precursors can be expected, making successful and timely monitoring and early warning strategies even more difficult.

Following the inverse modeling, we inferred the deflating and inflating sources at the depths of 6 - 12 km and 4 - 9 km responsible for the subsidence and uplift periods, respectively. We hypothesize that the inflation and the deflation sources are actually imaging the same deep reservoir system. We note, however, that the variability of the source depths between the subsidence and the uplift period is similarly observed elsewhere and can be due to several reasons, including 1) the uncertainty of the data and depth estimation through inverse modeling, (Dawson and Tregoning 2007) 2) a more complexly shaped, possibly vertically distributed, source rather than a single-point source, 3) upward migration of the magma during the magma inflow into the reservoir, 4) combined magmatic and hydrothermal activity as observed for example at Campi Flegrei, Italy (Battaglia et al. 2006).

The depth-range provided gives, for the first time, a rough estimation of the Llaima magma plumbing system. Volcanoes throughout the Andes' Southern Volcanic Zone show evidence of sources at 3 to 9 km, e.g. at Cordon Caulle (4 - 7 km), Maule (5 - 9 km), Copahue (3 - 6 km) (Fournier et al. 2010), hence they are at similar depth or somewhat shallower than at Llaima. More to the north, in the Andean Central Volcanic Zone, sources are at 5 -18 km, e.g. at Hualca Hualca (8 - 18 km), Cerro Blanco (5 - 10 km) (Pritchard and Simons 2004), or Lazufre (8 - 13km) (Ruch et al. 2008), hence being somewhat deeper than at Llaima. Although these source depths are of great uncertainty, Llaima volcano appears to host a reservoir at a depth that is in line with volcanoes investigated in the same setting.

2.8. Acknowledgments

This work was financially supported by the PROGRESS project and the project DFG WA1642/4-1. Data analyzed for this project was acquired by the European satellite ENVISAT and provided via the cat-1 proposal ID 3455. Discussions with Henriette Sudhaus and Eoghan Holohan are greatly appreciated.
The editor and the authors thank two anonymous reviewers for their assistance in evaluating this paper.

3. An active ring fault detected at Tendürek volcano by using InSAR

H.Bathke[1], *H.Sudhaus*[1,2], *E.P.Holohan*[1], *T.R.Walter*[1], *M.Shirzaei*[3]
(1) Department 2. Physics of the Earth, Helmholtz-Centre Potsdam, GFZ German Research Centre for Geosciences, Telegrafenberg, 14473 Potsdam, Germany
(2) University of Potsdam, Institute of Earth- and Environmental Sciences, Karl-Liebknecht-Str. 24-25, 14476 Potsdam, Germany
(3) School of Earth and Space Exploration, Arizona State University, Tempe, AZ 85287-6004, USA

3.1. Abstract

Although ring faults are present at many ancient, deeply-eroded volcanoes, they have been detected at only very few modern volcanic centers. At the so far little-studied Tendürek volcano in eastern Turkey, we generated ascending and descending InSAR time series of its surface displacement field for the period from 2003 to 2010. We detected a large ($\sim 105\,km^2$) region that underwent subsidence at the rate of $\sim 1\,cm/yr$ during this period. Source modeling results show that the observed signal fits best to simulations of a near-horizontal contracting sill located at around 3 km below the volcano. Intriguingly, the residual displacement velocity field contains a steep gradient that systematically follows a system of arcuate fractures visible on the volcano's mid-flanks. RapidEye satellite optical images show that this fracture system has deflected Holocene lava flows, thus indicating its presence for at least several millennia. We interpret the arcuate fracture system as the surface expression of an inherited ring fault that has been slowly reactivated during the detected recent subsidence. These results show that volcano ring faults may not only slip rapidly during eruptive or intrusive phases, but also slowly during dormant phases.

Keywords: Tendürek volcano, caldera subsidence, arcuate fracture system, InSAR displacement, fault reactivation

3.2. Introduction

Volcano ring faults present a two-fold hazard, in that they can both generate sizable earthquakes (Ekström 1994, Shuler et al. 2013) and act as eruption conduits (e.g. (Wilson and Hildreth 1997, Holohan et al. 2008)). On the other hand, they also can act as flow paths for ore-bearing hydrothermal fluids and hence represent mineral exploration targets (e.g. (Rytuba 1994)). Ring faults have been documented at ancient volcanic systems since the early 1900's (Clough et al. 1909) and mechanical explanations for their formation have been proposed since the 1930's (Anderson 1936). Although many volcanoes show the presence of ring structures, active ring faulting during phases of unrest at volcanoes is rarely observed.

Active ring faults have been detected mainly in more recent decades, as volcanoes worldwide have become increasingly closely monitored in order to prepare for potential eruptions and related hazards. As summarized in Tab. 3.1, active ring faulting has been discovered at several volcanoes of varying compositions and has been inferred to have various modes of movement and a wide range of spatial dimensions. Such faulting activity has been detected and monitored mainly seismically and/or geodetically, either by instrument networks or by satellite. While the former provide temporally-extensive but point-wise information, the latter enable spatially-extensive measurement of surface displacement, even at volcanoes that are remote or otherwise difficult to access.

Seismic methods have been used to detect blind ring fault activity during unrest or eruptive periods at the calderas of Rabaul (Mori and McKee 1987), Campi Flegrei (De Natale et al. 2006), and Bárdarbunga (Ekström 1994, Fichtner and Tkalčić 2010). At Fernandina (Simkin and Howard 1970, Filson et al. 1973), Miyakejima (Kumagai et al. 2001), and Dolomieu (Michon et al. 2007), seismic evidence of ring fault activity was complemented by visual observations and, in the latter two cases, by tilt-meter and GPS data. At Sierra Negra (Chadwick et al. 2006, Jónsson 2009) ring faulting was primarily detected through satellite-based Interferometry of Synthetic Aperture Radar (InSAR) data. Some of these detected ring faulting events occurred in conjunction with uplift (Rabaul, Campi Flegrei, Sierra Negra); others occurred in association with subsidence (Bárdarbunga, Fernandina, Miyakejima, Dolomieu).

Common to all the above examples is that slip on the detected ring faults entailed surface displacement magnitudes of meters to hundreds of meters and occurred over a short time (day to weeks) during large eruptions and/or intrusions. At Tendürek volcano in Eastern Anatolia, however, we find indicators that slip along ring faults can alternatively take place in conjunction with surface displacement of only several centimeters, occur very slowly (over many years) and lack clear evidence of contemporaneous intrusive or extrusive activity.

Our findings were arrived at by analyzing two ‘Small Baseline Subset’ (SBAS) InSAR time series of displacement at Tendürek. These were derived from Envisat ASAR images for the ascending and the descending satellite track and spanned 2004 to 2009 and 2003 to 2010, respectively. The retrieved displacement velocity signal is dominated by a steady subsidence that is centered on the volcano summit. Analytical source optimizations reveal that the dominant part of the measured subsidence signal can be well simulated by a contracting sub-horizontal, sill-like body.

After removing the sill-related displacement component from the InSAR observations, however, we found a ring-shaped gradient in the residual velocity field. As validated by high-resolution RapidEye satellite images, this gradient coincides with an arcuate fracture system visible on the volcano surface. These observations indicate long-term slip on a sub-surface ring fault at Tendürek.

Table 3.1.: Comparison of volcanoes with ring fault structures.

Volcano	Direction of surface movement	Diameter of ring faults [km]	Method of ring faults detection	Fault orientation(s) and slip sense(s)	Duration and cause of activity	Amplitude of surface displacement [m]	References
Sierra Negra (Galapagos)	uplift	elliptic, 7 x 10	geodetic	outward inclined, reverse faulting, trapdoor-like	several days, during repeating “trapdoor events”	1-3	(Chadwick et al. 2006, Jónsson 2009)
Rabaul (Papua New Ginuea)	uplift	elliptic, 5 x 9	seismic, geodetic	inward and outward inclined	$\sim$ 2 years, during several eruptions	1.6	(Nairn et al. 1995, Jones and Stewart 1997, Saunders 2001)
Campi Flegrei (Italy)	uplift/ subsidence	circular, 12	seismic, geodetic, gravimetric	inward inclined	months-years, repeatedly during several eruptions	up to several meters	(Scarpati et al. 1993, De Natale et al. 2006)
Miyakejima (Japan)	subsidence	circular, 1.6	seismic, photographic	inward inclined, normal faulting	short, $\sim$ 1 month, caldera collapse	$\sim 1,600 - 2,100$	(Geshi et al. 2002)
Dolomieu (LaRéunion)	subsidence	elliptic, 1.4 x 1	seismic, geodetic, photographic	inward inclined, normal faulting	short, $\sim$ 1 day, caldera collapse	~ 330	(Michon et al. 2007)
Fernandina (Galapagos)	subsidence	elliptic, 4 x 6.5	seismic, photographic	partly outward and inward inclined, normal and reverse faulting, trapdoor-like	short, several days, caldera collapse	~ 300	(Simkin and Howard 1970)
Bárdarbunga (Iceland)	subsidence	elliptic, 10 x 5	seismic	partly outward and inward inclined, reverse and normal faulting	short, several weeks	?	(Ekström 1994, Konstantinou et al. 2003, Fichtner and Tkalčić 2010)
Tendürek (Turkey)	subsidence	elliptic, 10 x 14	geodetic	eventually inward inclined, normal faulting	long, hundreds of years	0.08	(Yılmaz et al. 1998), this study

3.3. Tendürek Volcano

3.3.1. Tectonic setting

Tendürek volcano is located in Eastern Turkey, where active regional tectonics relate to the ongoing north-south convergence of the Arabian and Eurasian plates and the associated westward ‘escape’ of the Anatolian plate (Fig. 3.1). This tectonic setting is generally characterized by north-south shortening and east-west extension (Yılmaz et al. 1998). In the region around Tendürek, these strains are primarily accommodated by NE- or ENE-trending sinistral strike-slip faults and NW- or WNW-trending dextral strike-slip faults. Two of the latter, the Çaldıran and Balık Gölü faults (Karakhanian et al. 2004), lie immediately to the south and the north of the volcano, respectively. The region also hosts E-W trending folds and active thrust faults (e.g. the 2011 Van Earthquake), as well as N-S trending basins and normal faults. In addition, bends and/or steps along the strike-slip faults have locally resulted in uplifted ranges or pull-apart basins.

Volcanism in the region began in the Late Miocene in association with the onset of the Anatolian plate’s lateral escape (Yılmaz et al. 1998). After peaking in the Pliocene, volcanic activity persisted through the Quaternary and into historical times. Historically active centers include Mt. Ararat, Tendürek and Nemrut volcanoes (Karakhanian et al. 2002, Simkin and Siebert 2013). In the vicinity of Lake Van, various long-period seismic events have been recorded by local seismic networks (Horasan and Boztepe-Güney 2006). They suggest an upward movement of material, possibly magma or other fluids, and underline the magmatically and/or geothermally active nature of this region.

3.3.2. Geology

A low-relief, polygenetic shield volcano, Tendürek reaches a height of about 3580 m a.s.l. from a base of around 1800 m. The edifice and its associated volcanic field measure approximately 30 km north to south and 20 km east to west (Fig. 3.2). The edifice comprises two main cones, each with summit crater vents and many subordinate flank vents (Yılmaz et al. 1998). Morphologically, the coalescence of the main cones causes an E-W elongation of the volcanic edifice.

The basement rocks below Tendürek include Paleozoic meta-sediments, Cretaceous ophiolitic mélange, Paleocene marine limestones and flysch, as well as Late Miocene terrestrial sandstones and conglomerates (Yılmaz et al. 1998). These reflect the progressive closure of the Tethyan Ocean, with emergence and uplift of the Anatolian region as the Arabian and

Eurasian plates converged and collided. Alluvial deposits of the Çaldıran and Doğubeyazıt plains also underlie the Tendürek volcanic field at its distal edges in the north and south. Erupted materials are predominantly basaltic lavas, but these are interleaved with substantial trachyandesitic or trachytic lavas and pyroclastic deposits (flow and fall). Available radiometric dates for the main cones range from around 700,000- 500,000 years BP to 13,000 BP (Yılmaz et al. 1998). The youngest activity comprises small parasitic cones and basaltic lava flows formed along a N- S trending line at distances of up to 10 km to the northeast and the southeast of the main volcanic edifice. These youngest lavas are thought to have been produced around 2,500 years ago (Yılmaz et al. 1998).

The two main cones are partly encompassed by an arcuate fracture system located on the lower flanks of the edifice. This arcuate fracture system cuts the southern half of the edifice, but is not visible in the northern half (Yılmaz et al. 1998). It hence manifests as a half-ellipse with a 5 km long semi-minor axis and a 14 km long, E-W trending major axis. Tendürek is now considered to be dormant, although its hydrothermal system powers local fumaroles and hot springs (Ölmez et al. 1994, Karakhanian et al. 2004). An eruption or explosion at Tendürek may have occurred in 1855 (Karakhanian et al. 2002), however, and since the late 1970's there have been several reports of high fluorine concentration in local waters (Oruc 2008). These phenomena reveal the need to better understand the poorly-known state of activity at this volcano and its sub-surface structure.

3.4. Methods: data processing, subsampling and modeling

Constraints on the geometry and location of such sub-volcanic systems can be gained from studies of surface displacement (Dzurisin 2007). In situ instruments and on site investigations at Tendürek have also been very rare, however, due to political instability and the presence of minefields on the volcano (Byrne et al. 2009). Consequently, surface displacement measurements made by using space-born SAR imagery can provide useful independent information for approaching these questions in this case. The following sub-sections describe the InSAR time series analysis, the data subsampling and error estimation, and the source modeling approach.

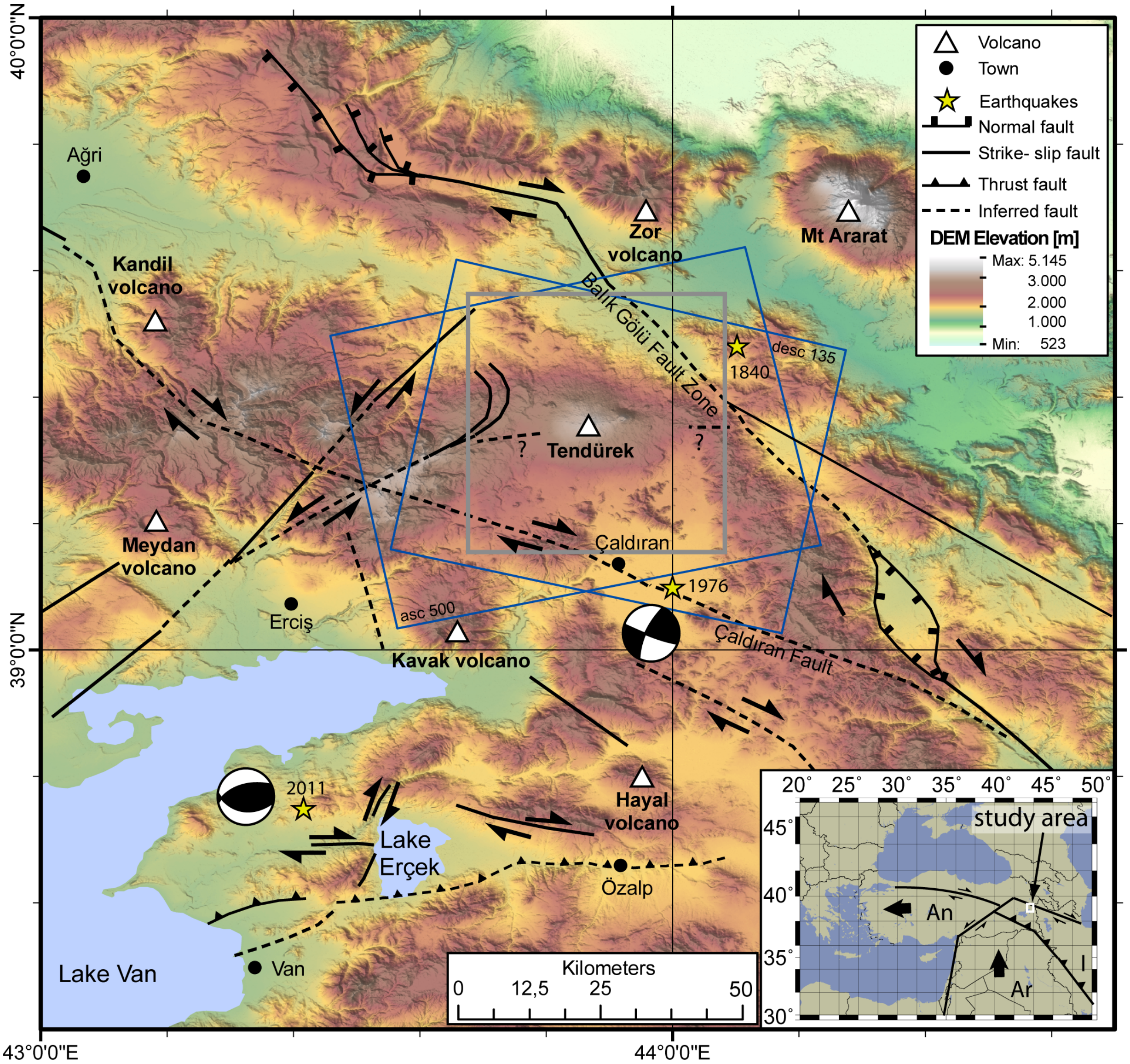

Figure 3.1.: Volcanoes and structures of Eastern Anatolia in the vicinity of Lake Van modified after (Yılmaz et al. 1998, Karakhanian et al. 2004, Dhont and Chorowicz 2005, Doğan and Karakaş 2013). The stars show the epicenters for the major seismic events in this region according to the NEIC catalog. The vertically oriented grey box marks the extent of Fig. 3.2. The inclined blue boxes show the footprints of the Envisat satellite data. The small inset figure to the lower right shows Little Asia and the major plate movements, modified after Reilinger et al. (2006). The white rectangle outlines the investigated region in the east of Turkey.

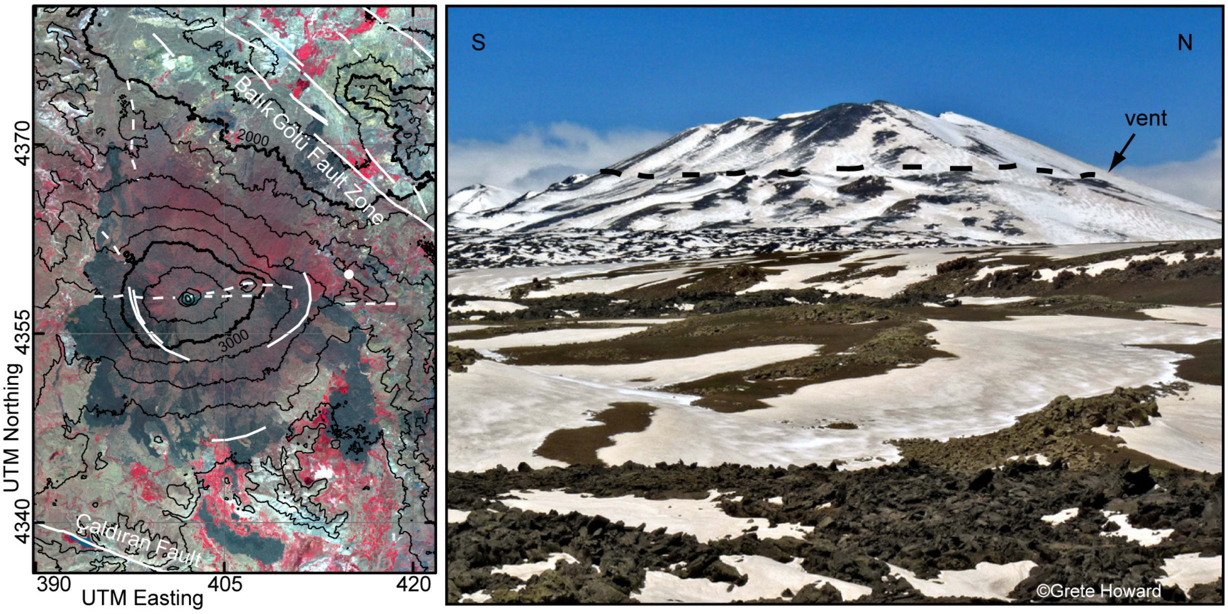

Figure 3.2.: Left: RapidEye image from 30-08-2011 in false color (red, green and blue channels are bands 5, 3 and 2, respectively; 5m resolution). The red color marks vegetation and dark grey colors mark recent lava flows. Black lines show the contour lines of the digital elevation model with an interval of 200 m. The white lines mark inferred and mapped faults modified after Yılmaz et al. (1998). The white dot marks the approximate location from where the picture (right) of Tendürek has been taken. Right: Photo of Tendürek volcano from 08-05-2009. The dashed black lines mark the ring fractures.

3.4.1. InSAR time series analysis

In the simplest approach, displacement at volcanoes can be derived from interferometry of two SAR images acquired at different times (2-pass interferometry). In cases where displacement magnitude is low, however, such as might be expected at a dormant volcano like Tendürek, simple 2-pass InSAR may not yield any useful displacement signal. A more complex approach to detecting surface displacement at volcanoes is to generate an InSAR time series, whereby numerous SAR images taken over a longer time span are combined. One advantage of this approach is that it increases the signal to noise ratio, by for instance concentrating on temporally stable information and by facilitating the reduction of atmospheric artifacts. This enables the detection of even small displacements that occur over a longer time frame than is generally possible by using simple 2-pass SAR interferometry alone. A second advantage is that the time-series approach yields insights into the temporal evolution of displacement.

To generate an InSAR time series for Tendürek, we combined 19 SAR images acquired by the ENVISAT satellite in the years from 2004 to 2009 in ascending track (track 500), and 22 images from 2003 to 2010 in descending track (track 135) (Fig. 3.3). Time series generation involves making all possible 2-pass interferograms from these data sets, selecting and combining those interferogram pixels with the best signal-to-noise ratio, filtering the interferometric phase signal to improve its quality, and finally converting the phase information to displacement in the line-of-sight of the radar satellite.

In detail, the processing chain for the InSAR time series involved the following steps, algorithms and software. For the SAR data focusing and interferogram formation, we used the software packages RoiPac (Rosen et al. 2004) and Doris (Kampes and Usai 1999), respectively. To derive differential interferograms, i.e. to remove the phase contributions due to topography, we used the digital elevation model (DEM), derived from the shuttle radar topography mission (SRTM), at a resolution of $\sim 90\,\mathrm{m}$ (Farr et al. 2007). Differential interferograms have been filtered using a Goldstein adaptive filter (Goldstein and Werner 1998). We extracted the displacement signal from the interferograms and analyzed the temporal evolution of the displacement, by using the small baseline subset (SBAS) module in StaMPS (Hooper 2008).

StaMPS software uses interferometric phase shifts of identified stable pixels instead of complete interferograms. The stability of a pixel is evaluated based on its interferometric phase coherence and signal amplitude dispersion. For pixel selection we used 53 small baseline interferograms in ascending orbit, and 69 interferograms in descending orbit (Fig. 3.3).

For phase unwrapping, we used the minimum cost flow algorithm implemented in the snaphu software package (Chen and Zebker 2001). Spatially correlated phase contributions, i.e. turbulent atmospheric phase delay, and phase contributions due to orbital and DEM errors, can obscure any displacement-related signal. We removed these phase contributions by applying a low-pass filter in space and a high-pass filter in time to the unwrapped data (Ferretti et al. 2001, Hooper 2006). Furthermore, several independent interferograms from both satellite tracks confirm that the measured signal is mainly related to ground displacement rather than to a topography-correlated atmospheric phase contribution (Hanssen 2001) (Supplement A.2.2, Supplementary Fig. A.7 - A.10). Our remaining signal is composed of surface displacement and reduced noise, and can be used to determine the properties of its source.

We discarded some interferograms from the time series due to their low signal-to-noise ratio. Finally, 47 interferograms in ascending mode, and 52 interferograms in descending mode were used in the generation of the time series.

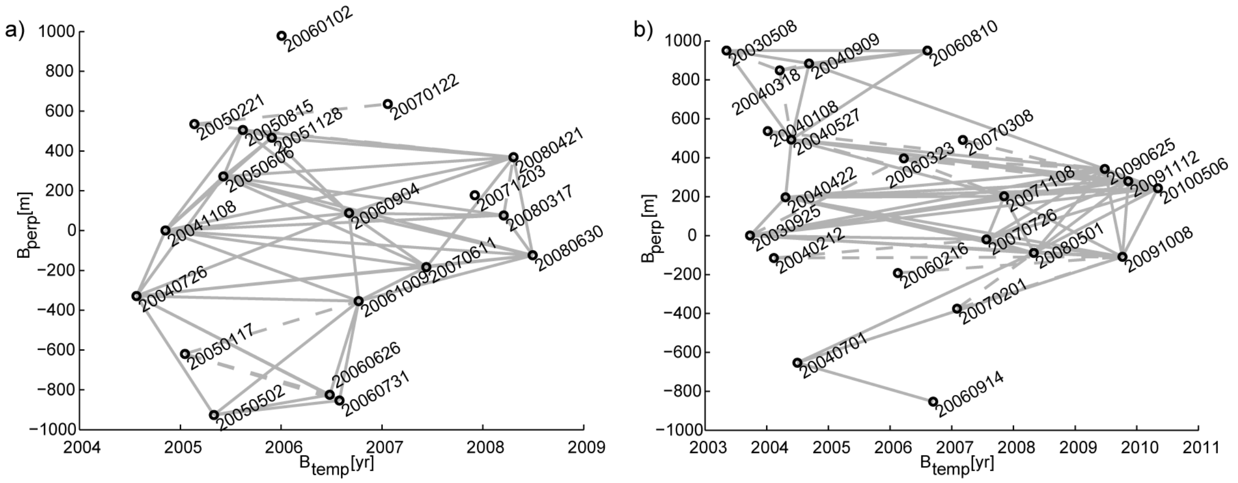

Figure 3.3.: Diagram of temporal and perpendicular baselines for the 53 small baseline interferograms of the ascending track (a) and 69 interferograms of the descending track (b). Grey lines connect the dates of images (black circles) that form an interferometric pair in the time series analysis. Dashed lines mark images that have been discarded due to low signal-to-noise ratio.

3.4.2. Data subsampling and error estimation

An InSAR time series typically contains several hundreds of thousands of data points, not all of which carry independent information. The analysis of such a data set can be made more efficient by reducing the number of data in an objective manner. The reduced data set will have data errors characteristics that differ from the original data set, however. Consequently, we empirically estimate the data errors of the original data set, and from this estimate we derive a weighting function for each point in the reduced data set. In that way we balance the quality and distribution of the reduced, or subsampled, data set.

In order to reduce the number of data points, we used the Quadtree algorithm (Jónsson et al. 2002). We adjusted the algorithm's parameters, so that we ended up with about 2,500 pixels for each satellite track. After correction for atmospheric, orbital and topographic effects, any observed displacement in the InSAR time series will include some correlated and/or uncorrelated noise. To estimate the amount of such noise, we created sample variograms and co-variograms from the full observational data set, by plotting the variance and covariance values of point-pairs, as a function of their separation (Sudhaus and Jónsson 2009). The data variance was estimated based on sample semi-variograms, at separations where the increasing variance values reach a stable plateau level (Supplement S1). The covariance was estimated by fitting a positive-definite function to the samples of each co-variogram (Supplementary Fig. A.6). From the variance and the covariance function, we built the data error variance-covariance matrix, such that the data points of each track were individually weighted in the later source optimization (See Section 3.4.3).

3.4.3. Source modeling and optimization

Surface displacement observed in InSAR time series at volcanoes is usually related to sub-surface processes such as volume changes, migration of fluids or movement on fractures. To investigate the characteristics of potential sub-surface sources causing such displacement, we generally idealize the volcano system in terms of an analytical model. By changing the model's parameters in a statistically-guided manner, we find the optimum model whose parameters best reproduce the surface displacement data.

In our approach, we consider a magmatic or hydrothermal source of finite extent rather than a geologically more ambiguous point source. We have therefore implemented planar (Okada 1985) and ellipsoidal (Yang et al. 1988) source models. We assumed a homogeneous elastic half-space with a Young's modulus of 33 GPa and a Poisson's ratio of 0.25. With these models, we ran a source optimization to estimate the optimal parameters of these sources that could best explain the observed displacement.

We jointly optimized the ascending and descending data by using a Monte Carlo direct search method (Sambridge and Mosegaard 2002), specifically a genetic algorithm (Holland 1975). This search algorithm starts with a chosen number of randomly drawn models, and then explores the model parameter space for models with a 'low-cost', i.e. with a good fit to the data. During the search, the parameters of preferably low-cost models are recombined to form a ‘next generation’ of models, which again are evaluated, sorted and selected by their cost. By doing this iteratively, the parameters of the models converge towards an optimum solution with lowest cost.

To account for errors of the subsampled data sets in the source modeling, we weighted the residual observations,$\mathbf{v}$, which constitute the difference between the observed and the synthetic modeled displacement, with the inverse of the empirically estimated data error variance-covariance matrix, $\mathbf{C}^{-1}$. Thus the cost, f, in the optimization is given by:

$$f = \mathbf{v}_{asc}^{T}\mathbf{C}_{asc}^{-1}\mathbf{v}_{asc} + \mathbf{v}_{desc}^{T}\mathbf{C}_{desc}^{-1}\mathbf{v}_{desc} \tag{3.1}$$

Several parameters control the performance of the search algorithm. Population size is the number of models in each generation from which, based on the selection rate, a fraction of the population with the lowest costs are selected for the next generation. To explore a large solution space, a fraction of the selected solutions are also changed arbitrarily, based on the mutation rate. We chose a population size of 100, a selection rate of 0.5, a mutation rate of 0.7 and a generation number of 1,000.

To test the robustness of the model results with respect to errors of the subsampled data, we also created synthetic noise, based on the related error statistics (Wright 2003, Sudhaus and Jónsson 2009). For each independent optimization run, new realizations of synthetic noise were added to the reduced data set, such that the data is slightly modified to reflect the data error. With these noise-modified data sets, we ran 200 independent optimizations, and obtained a distribution of possible source models that explains the data well. To estimate the 95% confidence intervals, and to allow for non-Gaussian model parameter distributions, we sorted the solutions of each model parameter and calculated the upper and lower 2.5% percentiles. From these model parameter distributions and the correlations between model parameters (i.e. model parameter trade-offs), we can learn about the uncertainties and non-uniqueness associated with our optimum sub-surface deformation source.

3.4.4. RapidEye imagery

Volcanic eruptions result in the generation of various types of erupted material, the deposition of which can be affected by pre-existing geologic structures and morphological features. Mapping out the distributions of deposits of different types may therefore reveal the locations of older geologic structures. In this way, high-resolution multispectral satellite data, which allow one to differentiate deposits of different chemical composition, may

also enable one to map lineaments and fractures at surface.
We used six RapidEye image tiles (25x 25 km), dating from 30-08-2011, which have five spectral bands (3 visible, 2 near-infrared) and a 5 m spatial resolution. To easily identify lava flows from their surroundings, we produced a false color image by using the bands 5, 3 and 2 for the red, green and blue channels, respectively. From this high-resolution image, we can then identify by eye differences in volcanic deposits and map structures around the volcanic edifice.

3.5. Results: InSAR time series and modeling

3.5.1. Displacement velocity field at Tendürek

The InSAR time series shows that Tendürek volcano underwent gradual subsidence between 2003 and 2010 (Fig. 3.4). Displacement rates in radar line-of-sight are near-linear in the ascending data set (Fig. 3.4a) and slightly non-linear in the descending data set (Fig. 3.4b). As first order approach, we therefore separately calculated a linear (i.e. average) velocity of the observed signal for each track. The subsidence velocity reaches a maximum rate of 11 mm/yr at the volcano summit. This subsidence rate decreases to about 6 mm/yr on the upper volcano flanks and to about 2 mm/yr on the lower volcano flanks, where it is similar to the data noise level (see Supplementary Table A.1).
The prominent shape of the signal in the ascending track is almost circular (diameter ~ 10 km) (Fig. 3.4a, top panel), whereas that in the descending track appears to be more elliptical in E-W direction (major and minor axes of 14 x 10 km) (Fig. 3.4b, top panel). Profiles through the signal show a bowl-shaped pattern at the volcano summit that continues with a smaller gradient towards the lower eastern volcano flanks (Fig. 3.4, middle panels). This gradient is weak in the E-W oriented profiles of the ascending track compared to a strong gradient in the E-W oriented profiles of the descending track. This apparent difference in signal pattern likely arises from the different satellite viewing geometries. Nevertheless the area of subsidence covers $\sim 105\,km^2$, lies above 2600 m a.s.l. and is elliptical in both ascending and descending satellite tracks.

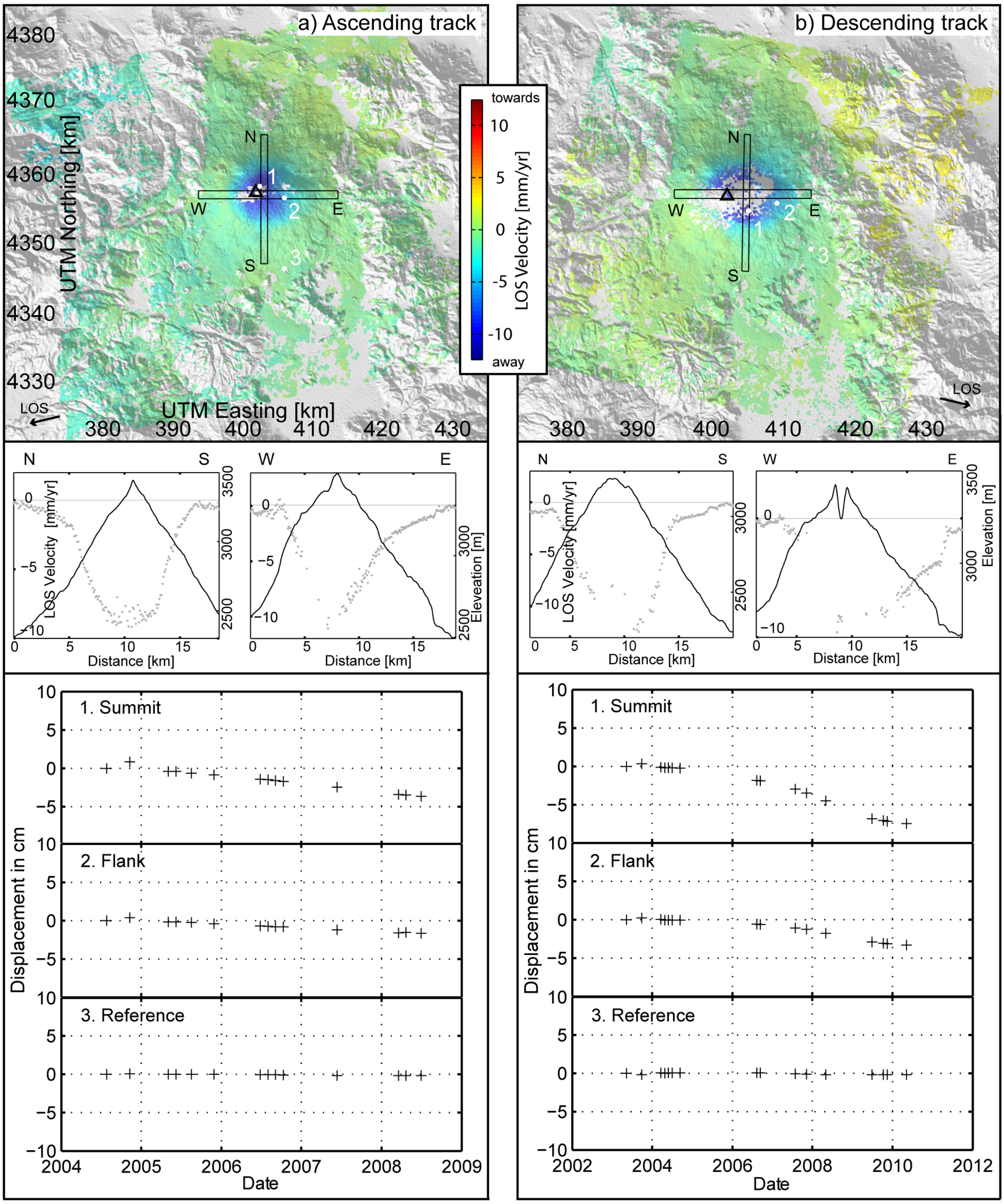

Figure 3.4.: Top panels: Displacement velocity from the SBAS time series analysis of the ascending (a) and descending (b) track satellite data. The black triangle marks the western crater at the summit of Tendürek volcano. Mid panels: Profiles along N-S and E-W of the LOS velocity (grey dots) and the surface elevation (black line). Bottom panels: Temporal changes of the mean of selected pixels within a circle of 200 m radius at the position of the white numbered points in the top panels.

3.5.2. Source modeling of the Tendürek subsidence signal

The subsampled data set

As is typical for volcanoes, the pixel distributions in our data sets are heterogeneous (Fig. 3.4). Due to rough topography and snow coverage, there are only a few stable pixels at the volcano summit and in the far-field region (at distances greater than c. 20 km). In contrast, there are many stable pixels on the flanks of the volcano. The Quadtree square distribution (Fig. 3.5a & b) compensates for this heterogeneity by having a denser sampling of pixels at the summit and in the far field (compared to the original data set), whereas sampling of pixels on the flanks is sparser. We used these subsampled or reduced ascending and descending data sets for the modeling, results of which are presented in the next sub-sections.

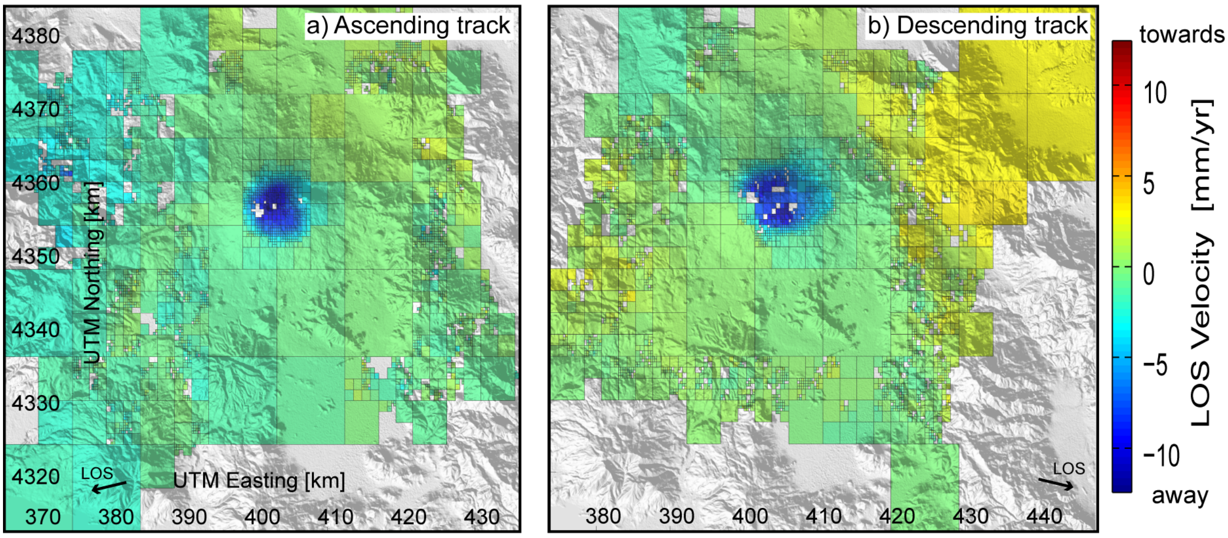

Figure 3.5.: Results of data subsampling: Quadtree squares for the ascending and the descending track, respectively.

Okada source model results

The best fitting Okada plane lies below the center of the volcano and dips gently towards the north-east. This optimum Okada plane measures 6 x 7 km, is centered at UTM easting 403.5 km and UTM northing 4356.8 km, lies at a depth of 2.7 km, strikes at 340°, dips at 11° and closes at 1.4 cm/yr. This result has an estimated volume change of $\sim 4.55 \cdot 10^{-3}\, km^3$. The dip and depth of the model plane are the least well constrained, since here we find bi-modal parameter distributions. The other parameters are well constrained, however, as shown by the histograms with pronounced peaks and narrow confidence intervals (Fig. 3.6, Tab. 3.2). The optimization results for Okada source models are therefore generally robust. Two-dimensional correlations of the Okada source parameters are provided in Supplementary Figure A.11. They show that solutions change significantly when the strike changes from northwest to northeast (i.e. when the origin of the Okada plane differs). Moreover, as depth increases, the dip increases, the length shortens and rate of closure increases.

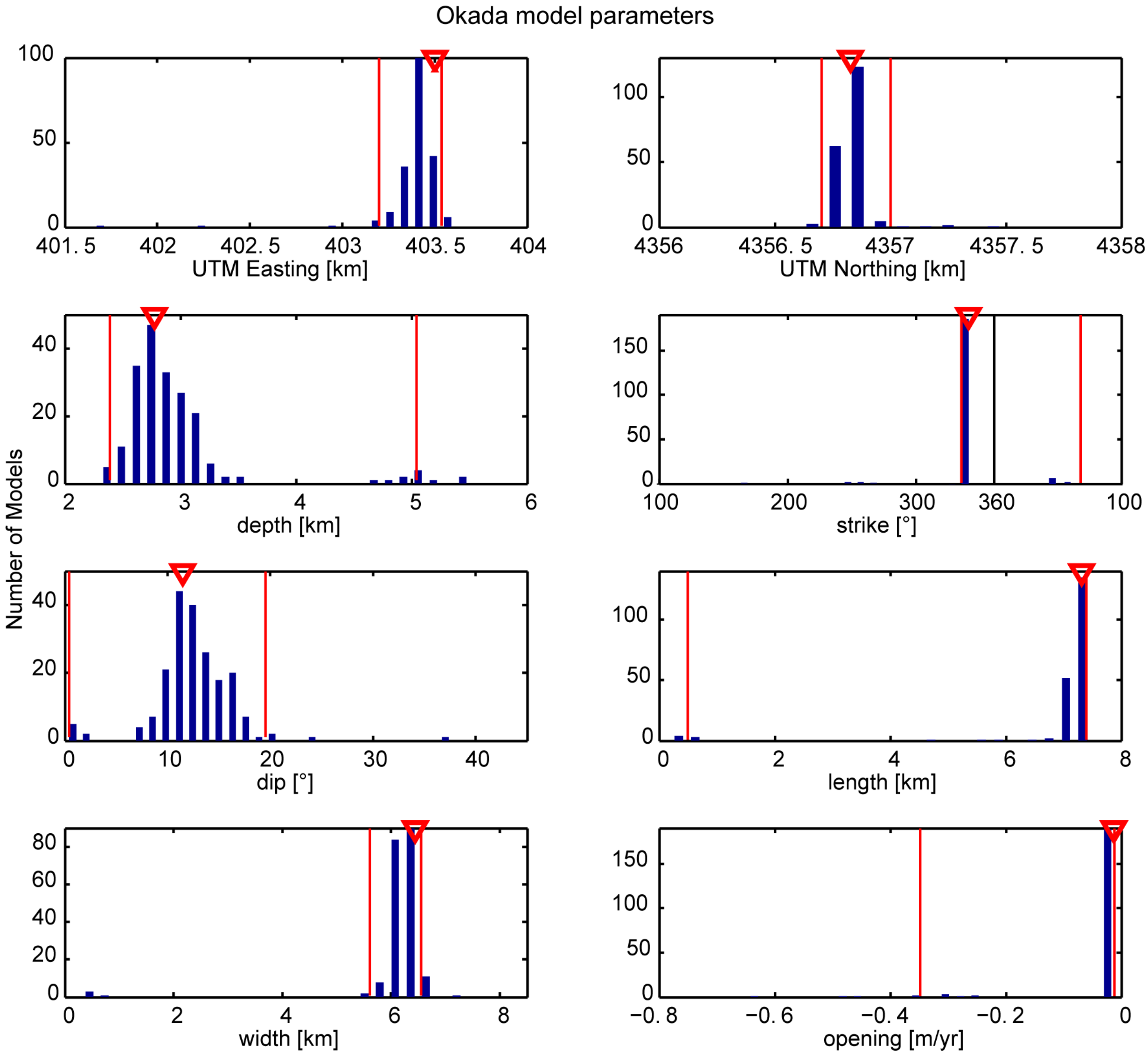

Figure 3.6.: Histogram of 200 independent optimization results for the Okada model parameters by using Quadtree subsampled data. Triangles give the corresponding optimum values and the red vertical lines mark the 2.5 and 97.5% percentile.

Table 3.2.: Optimization results: Parameters for the Okada and the Yang source models.

Okada Source				Yang source			
Source parameters	Opt. Solution	Percentile (2.5% 97.5%)		Source parameters	Opt. Solution	Percentile (2.5% 97.5%)	
UTM Easting [km]	403.5	403.2	403.5	UTM Easting [km]	403.5	402.8	403.7
UTM Northing [km]	4356.8	4356.7	4357.0	UTM Northing [km]	4356.8	4356.4	4357.1
Depth [km] w.r.t. mean elevation (1,9 km)	2.7	2.3	5.0	Depth [km] w.r.t. mean elevation (1,9 km)	3.6	3.4	4.8
Strike [°]	341	335	68	Strike [°]	215	35	308
Dip [°]	11	1	20	Plunge [°]	3	~ 0	35
Length [km]	7.3	0.5	7.4	Major axis [km]	4.7	1.4	4.9
Width [km]	6.4	5.6	6.6	Axis ratio b/a	0.07	0.06	0.46
Opening [cm/yr]	-1.4	-1.4	-34.9	Pressure change [GPa]	-0.012	-0.018	-0.001

Yang source model results

The best fitting Yang ellipsoid is also centered below the volcano and it is almost horizontal with a very gentle plunge towards the SW. This optimum ellipsoid measures 4.7 x 0.33 km, is centered at UTM easting 403.5 km and UTM northing 4356.8 km, lies at a depth of 3.6 km, has a plunge azimuth of 215° and a plunge angle of 3°, and undergoes a pressure change of -12 MPa/yr. This result has an estimated volume change of $\sim 3.29 \cdot 10^{-3}\, km^3$. The optimizations of the Yang source model are generally less robust, however.
The histograms (Fig. 3.7) and the parameter correlations (Supplementary Fig. A.12) for the Yang source show that there are three major peaks in most of the source distributions (UTM easting, UTM northing, plunge azimuth, plunge, major axis). They show that an ellipsoid at 3.5-4 km depth, with a nearly horizontal major axis of 4-5 km length explains the displacement almost as well as a shallower ellipsoid at 3.2-3.5 km depth with a vertical major axis of $\sim$ 1 km length (Tab. 3.2). A third solution is an even deeper located source at 4.5-4.9 km depth, with a not well-constrained length along the major axis. These solutions deviate in their plunge azimuth also. The optimum solution with an almost horizontal plunge has - due to the axis symmetry of the ellipse - two peaks in the distribution of the plunge azimuth, at about 30° and 220°. Other less likely solutions tend to group at

near-perpendicular plunge azimuths of 130° and 310°. Overall the pressure change is very poorly constrained and ranges from 1 to 20 MPa/yr.

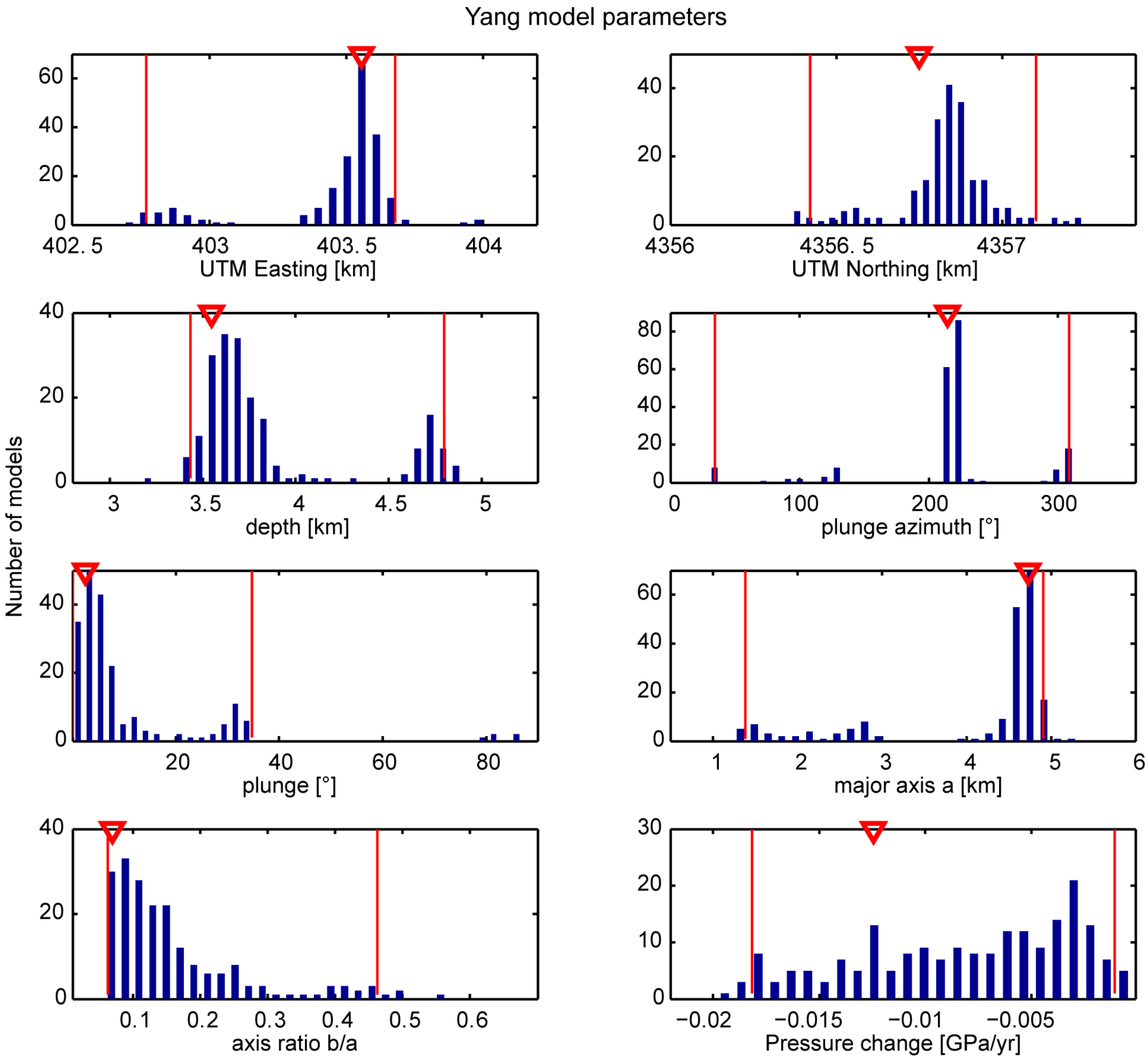

Figure 3.7.: Histograms of 200 independent optimization results for the Yang model parameters. Triangles give the corresponding optimum values and the red vertical lines mark the 2.5 and 97.5% percentile.

Analysis of residual displacements

Residual displacements can provide further insight into processes contributing to the signal that are not incorporated into our model. These are obtained through subtracting the displacement predicted by the optimum source models from the observed surface displacement (Fig. 3.8).

The vertical displacement component of our sill model can explain most of the observed signal, whereas the horizontal displacement component shows larger residuals (Supplementary Fig. A.13). The vertical and horizontal displacement component of our ellipsoidal model both show large spatially correlated residuals (Supplementary Fig. A.14).

The residual displacement in the ascending and descending data generally does not exceed 3 mm/yr for the Okada model and 5 mm/yr for the Yang model. Therefore these models explain the majority of the observed displacement signal.

Nonetheless, a systematic ring-like pattern is seen in maps and profiles of the residual displacement velocity field (Fig. 3.9). In the ascending track, we identified an ellipsoidal boundary, where a gradient in the displacement of up to some millimeters is evident (Fig. 3.9a & c). In the descending data (Fig. 3.9b & d), we found pronounced discontinuities, rather than gradients. These coincide with Tendürek volcano's arcuate fracture system (Yılmaz et al. 1998) (Fig. 3.10a & b).

3.5.3. Surface features in RapidEye data

In the false color image of the RapidEye data (Figs. 3.2, 3.10), vegetation is shown in red and recent lava flows are shown as shades of dark grey. In this image, we note several features of interest related to the arcuate fracture system surrounding the volcanic edifice. Firstly, there are several sub-parallel lineaments on the south- western flank (Fig. 3.10c). These are up to ~ 6 km long and are concentrated in a ~ 1.3 km wide region. Secondly, there is a small volcanic vent located directly on the continuation of the arcuate fracture system (Fig. 3.10d). Thirdly, the arcuate fracture system appears to have acted as a barrier to some of the youngest lava flows in the southeast (Fig. 3.10e).

3.6. Discussion

Our InSAR time series shows not only that the so far little-studied Tendürek volcano subsided, but also that this surface displacement was partly controlled by an arcuate fracture system on the volcano flanks. From 2003 to 2010, Tendürek underwent a maximum subsidence of 7-8 cm, within an elliptical area of 10 x 14 km and with a steady, near-linear velocity of 11 mm/yr.

For the period of 1993- 2000, an unpublished 2-pass interferometric study (M.Sc. Thesis) by Tolluoglu (2006) reported a maximum subsidence of about 12-15 cm at the volcano summit. This corresponds to a rate of 15-19 mm/yr, which has a similar signal magnitude

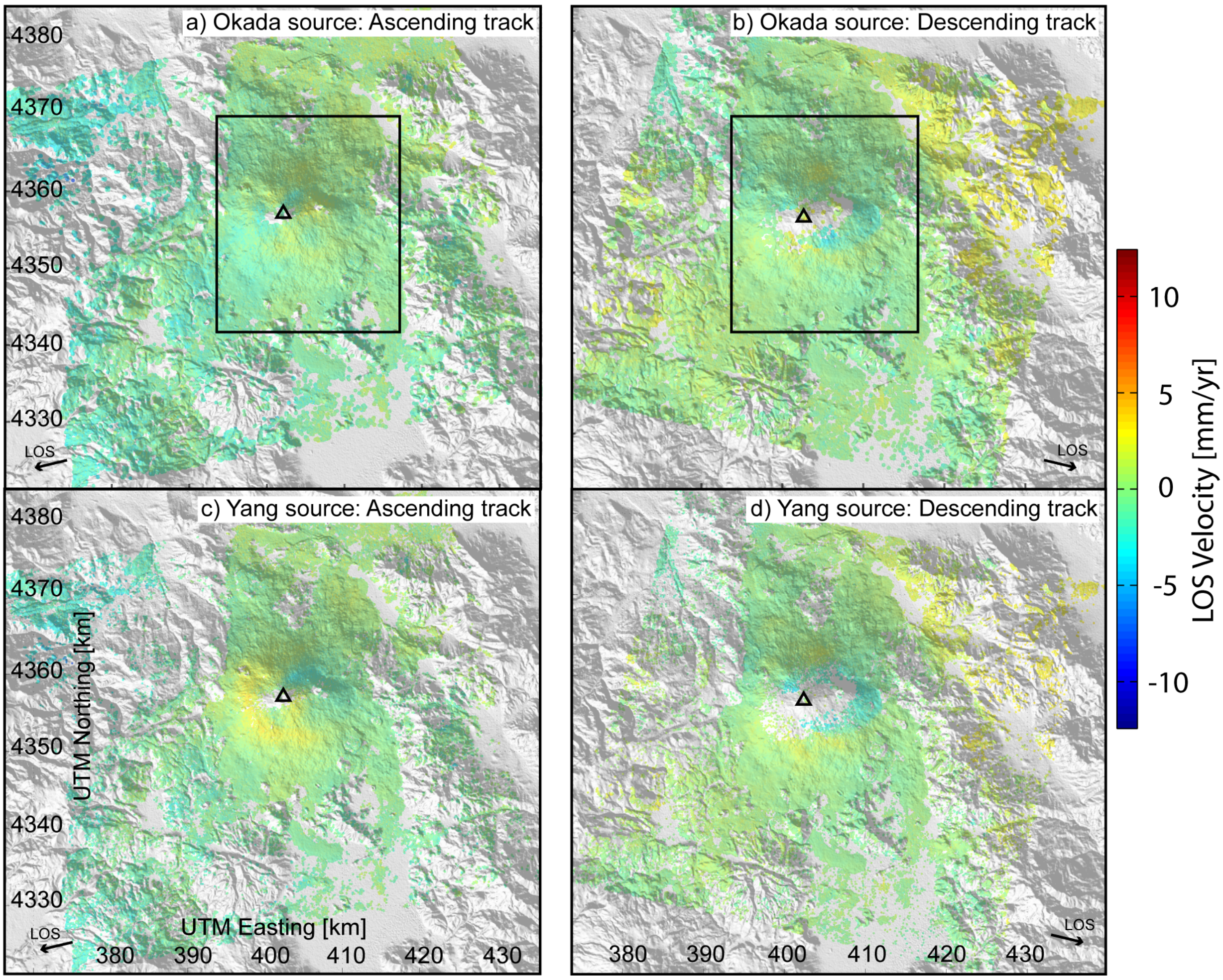

Figure 3.8.: Residual displacement velocity of the optimum Okada source model for the ascending (a) and for the descending (b) tracks and of the optimum Yang source model for the ascending (c) and descending (d) tracks, respectively. The black boxes in a) and b) mark the extent of the enlarged residues in Fig. 3.9

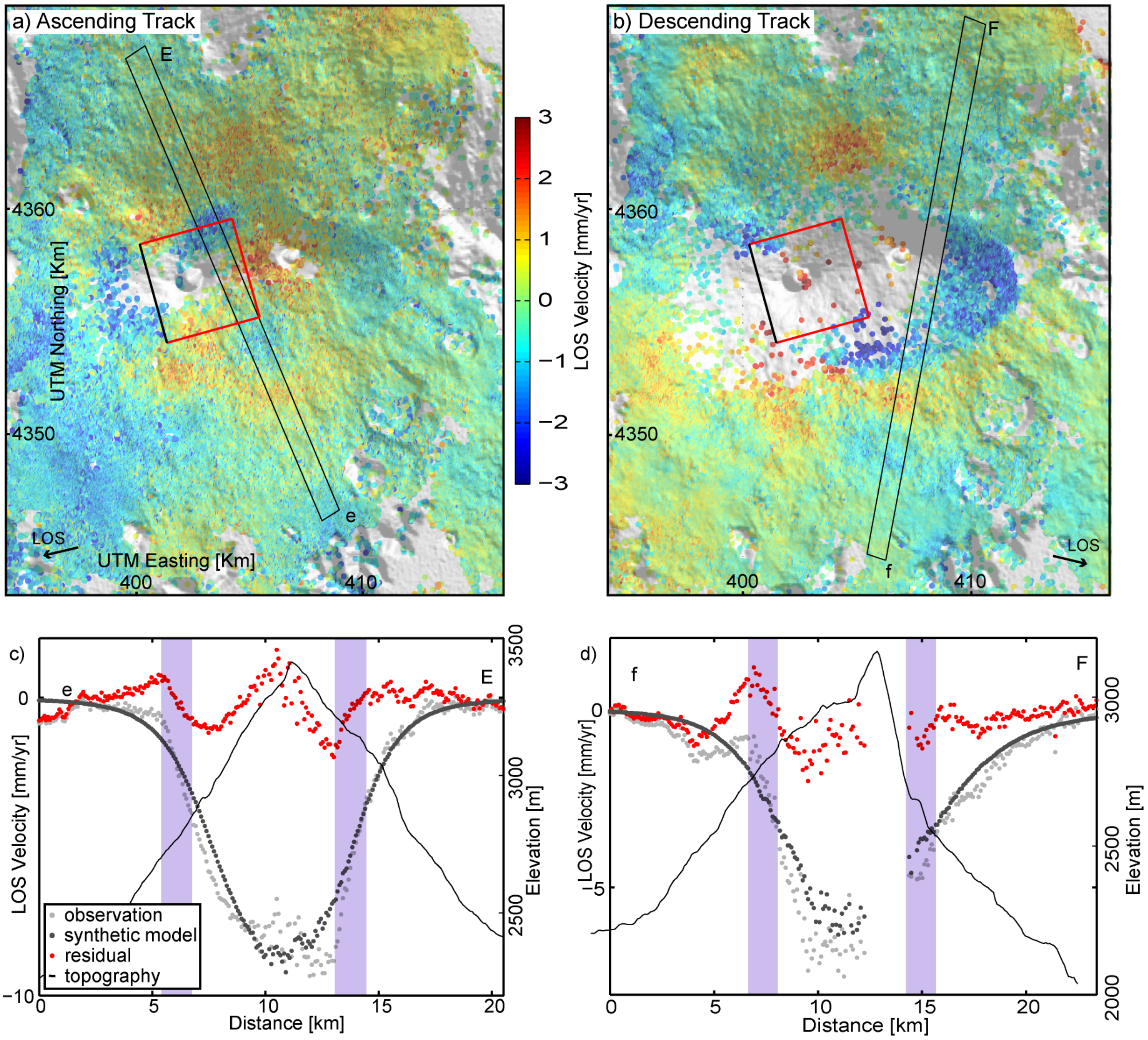

Figure 3.9.: Zoom into residual displacement velocity maps (a & b) and profiles (c & d). The red rectangles in a) and b) show the position and lateral dimensions of the optimum Okada source model (upper edge in black). The black rectangles through the volcano show the position of residual velocity profiles given in c) and d). These profiles are chosen to illustrate regions with strong gradient in the residual deformation. Light grey points give the observed line-of-sight displacement velocity, dark grey points show the synthetic displacement velocity of the inferred Okada plane and the red points mark the residual. The solid black line represents the elevation of the surface of the volcano. The vertical blue bars mark the inferred surface location of the arcuate fracture system.

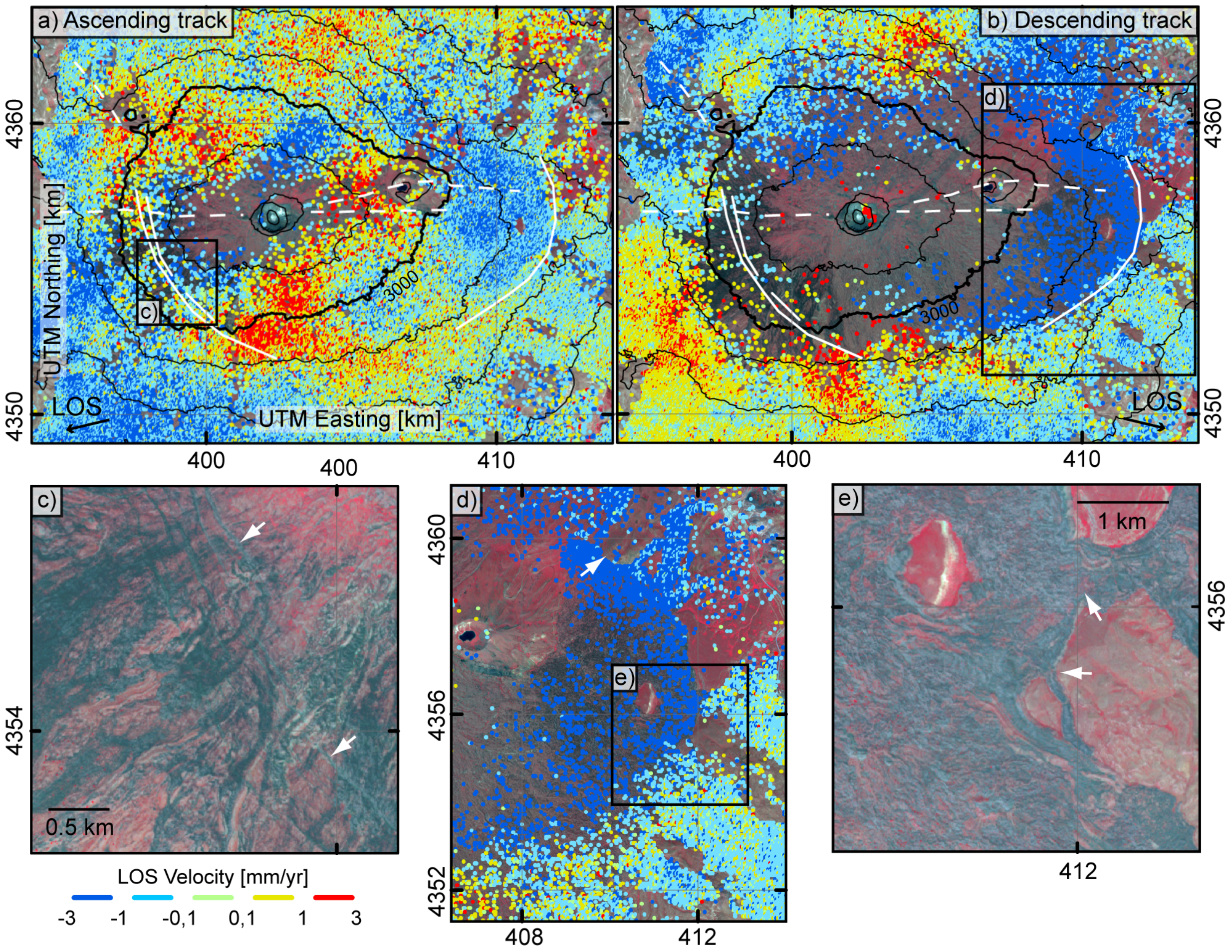

Figure 3.10.: RapidEye image in false color (see also caption Fig. 3.2). Residual displacement velocity of the ascending (a) and descending (b) tracks, with fault structures (solid and dashed white lines) at Tendürek volcano, modified after (Yılmaz et al. 1998). Black lines show the contour lines of the digital elevation model with an interval of 200 m. d) Enlarged box of the descending residual velocity. The white arrow shows the location of a small eruptive vent. c), & e) Enlarged images of the south-western and eastern volcano flanks, where white arrows indicate the ring fault fractures and the places, where the migration of a lava flow has been guided by the previously existing ring fractures.

to the subsequent subsidence detected in our study. Consequently we conclude that this subsidence has likely been on-going since at least 1993.

Analytical source modeling of the detected signal is most consistent with, and mostly explained by, a deflating sill-shaped deformation source. The residual displacements show a strong gradient along the location of the arcuate fracture system (Fig. 3.10a & b). In the following sections, we discuss the assumptions and restrictions of the applied methods, possible explanations for the observed subsidence signal, and the context of our interpretation with respect to active ring faulting at modern volcanoes.

3.6.1. Modeling assumptions

Our modeling gives insight into the subsurface processes that could have caused the observed signal. Nevertheless, as in any such study, there are some model assumptions that are unlikely to be true in nature and that, if changed, could in detail lead to some differences from the modeling results presented.

The main a priori assumptions here are that topography, crustal heterogeneities, and secondary deformation sources are negligible when modeling the dominant deformation source. For topography, Cayol and Cornet (1998) showed that displacement on volcanoes with slopes higher than $\sim 20°$ differs significantly from estimations made assuming a half-space. The average slope of Tendürek is only about 7°, however, and therefore the role of topography is ignored by us in this case. The absence of crustal heterogeneities in our model is also justified, because without appropriate constraints, a more complex model setup would have resulted in larger model parameter ambiguities. Following analysis of residuals, the assumption of no secondary deformation source was found to be not strictly justified. As discussed below, however, this secondary source appears to be a ring fault, implementation of which into our modeling scheme is complex and beyond the scope of the present study.

A further minor a priori assumption here is that the deformation source exhibits a uniform displacement along its boundary (e.g. uniform closing along the Okada plane). We also tested distributed opening along our optimum Okada plane, however, this does not improve the model fit significantly. In the absence of better geological constraints, a more complex source dislocation pattern therefore does not improve the understanding of the source mechanisms at Tendürek volcano, and so we decided that adopting the simpler source is the better solution.

3.6.2. Interpretation of the main deformation source at Tendürek

The observed displacement velocity can be reasonably well explained with a range of Yang or Okada source models, rather than just through one precise optimum solution (Tab. 3.2). Nevertheless, the Yang source models lead to higher residual displacements than the Okada source models (Fig. 3.8). Therefore, we considered the Okada model to be more suitable for explaining the measured displacement. Surface displacement data alone is not sensitive to distinguish between a sill-like source from a flat topped reservoir (Yun et al. 2006). Therefore, our best fit sill-like source could also resemble the flat roof of a more vertically extensive reservoir.

In the following paragraphs, we consider three geological phenomena that commonly cause deformation at volcanoes and hence could be represented by the inferred deformation source model.

A first common deformation mechanism is spreading or sagging of the volcano edifice under gravity. Spreading would result in outward directed horizontal motion on the volcano flanks, whereas inward horizontal motion is observed (Supplementary Figs. A.13 & A.14). Moreover, both spreading and sagging require a layer of soft and weak material for the volcano to sag into or slide along (e.g. (Byrne et al. 2013) and references therein). The most obvious candidates for such a layer at Tendürek are the recent alluvial sediments. These outcrop at the volcano base between 1.8 to 2.3 km a.s.l., and have thicknesses of less than 200 m (Yılmaz et al. 1998). Our modeling results show that the deformation source lies at a 0.8-3.1 km b.s.l (Fig. 3.11). Consequently, we discard spreading or sagging as potential deformation processes at Tendürek over the period of observation.

A second possible deformation mechanism is hydrothermal activity. This occurs at Tendürek, as evidenced by fumarolic activity (Ölmez et al. 1994), and can cause surface subsidence through surface discharge or subsurface withdrawal of fluids. In addition, alteration and weakening of rock masses by hydrothermal activity can lead to their easier compaction and deformation (Cecchi et al. 2004), potentially also resulting in subsidence at the volcano.

A third possible source for the subsidence at the surface is volume loss arising from the cooling, solidification and degassing of a subsurface magmatic body. The total volume reduction based on our optimum source models is around $3.29-4.55 \cdot 10^{-3}\,km^3$ with an annual rate of $0.47 \cdot 10^{-3}\,km^3/yr$ and $0.65 \cdot 10^{-3}\,km^3/yr$ for the Yang and Okada sources, respectively. The complete solidification of a basaltic melt with a density of $2600\,kg/m^3$ to solid gabbro with a density of $2800 - 3100\,kg/m^3$ causes a volume reduction of around 7-16% (Sigmundsson et al. 1997, Shirzaei et al. 2013). The solidification of more evolved melts (e.g. trachytic or granitic) results in even higher volume reductions of 18-25% (Sigurdsson

2000). From the assumptions that the potential magma body below Tendürek measured 6 x 7 km (as indicated by our best-fit sill-like model) and that it had a conservative thickness of 50 m, its initial volume was 2.1 km^3. This means that a 0.2% volumetric change of this body would match the estimated absolute volume change of the source. Therefore, a partial solidification of the magmatic body, interlinked with volume reductions due to associated cooling and degassing, could comfortably explain the observations.

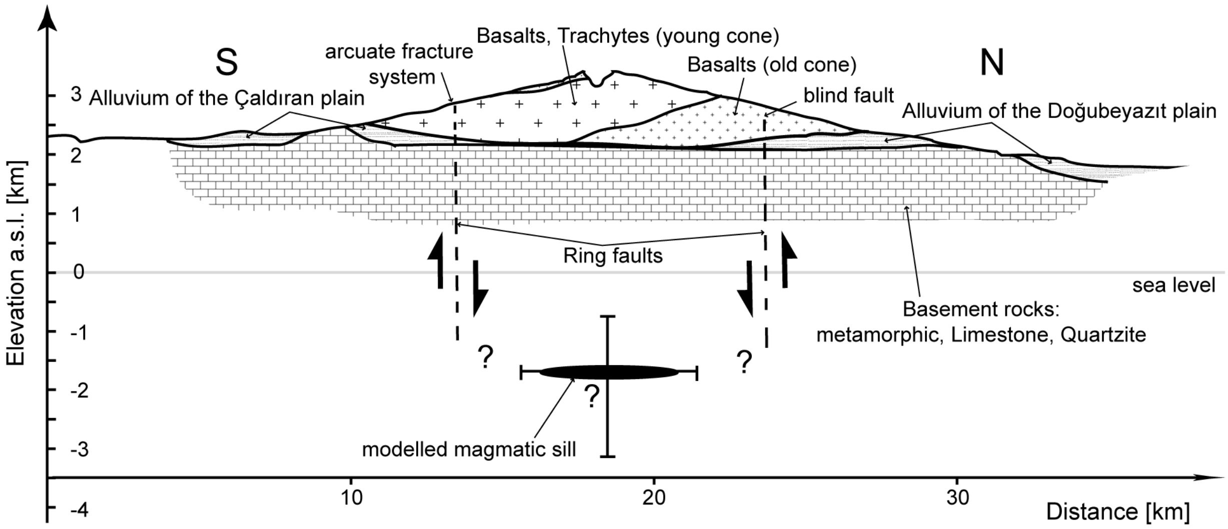

Figure 3.11.: Schematic cross section of the source of deformation and the inferred ring fault system at Tendürek volcano (vertically exaggerated by a factor of 2). The dip angle of the ring fault is speculative, indicated by question marks and therefore the ring fault is drawn vertically by convention. Geologic units and the structure of the basement are schematic and modified after Yılmaz et al. (1998).

3.6.3. Tectonic influence

Several features of the Tendürek volcanic field are consistent with formation under a tectonic regime of North-South shortening and East-West extension (Fig. 3.1) (Reilinger et al. 2006). These include a N-S alignment of several parasitic cones in the east of the volcanic field and a N-S trending fissure in the west, which presumably reflect the preferred orientation of regional dykes (Yılmaz et al. 1998). The E-W elongations of the volcanic edifice and of the arcuate fracture system are not obviously consistent with such as regional dyke control, however. Similar perpendicular alignment of the long axis of the displacement field to the regional dyke orientation was observed in the Lazufre volcanic field, South Andes (Ruch and Walter 2010). Maximum horizontal compressive stress perpendicular to the elongation of the displacement field can explain these patterns following the borehole breakout theory (Ruch and Walter 2010). A similar concept might apply as well at Tendürek volcano.

Alternatively, the orientations of the edifice and the arcuate fracture system could relate to control on magma pathways from a regional fault. Yılmaz et al. (1998) map an east-west trending fault on the eastern side of the volcano (Figs. 3.1 & 3.2), which, if projected westward along strike, passes through the main craters, as well as the long axes of both the edifice and the arcuate fracture system. To the East, this fault appears to link into the Balık Gölü fault, and thus may well be a part of the highly active regional tectonic system.

3.6.4. An active ring fault at Tendürek volcano

The arcuate fracture system on Tendürek volcano coincides with systematic gradients in the residual displacement velocity maps (Fig. 3.10a & b). Although this fracture system has developed only around the southern half of the volcano, the associated residual displacement gradients also appear around the north of the volcano (Fig. 3.10a & b). This means that the arcuate fracture system most likely represents the trace of a subsurface fault that forms a complete ring around Tendürek volcano.

That the surface expression of the ring fault is better developed on one side of the volcano (Figs. 3.2 & 3.10) is commonly observed in analog and numerical models of ring fault formation (e.g. (Roche et al. 2000, Holohan et al. 2011)), as well as at volcanoes in nature (Lipman 1997) (‘Trapdoor’-like subsidence - Tab. 3.1). A geodetic observation consistent with such larger slip in the south and west of the ring fault is that the horizontal component of the residual displacements within the ring structure is dominantly westward (Figs. S4 and S5). This is in agreement with recent analog models that show unidirectional horizontal displacements of caldera floors, directed toward the area of inferred maximum slip along the ring fault (Holohan et al. 2013). By adopting this concept to the Tendurek ring fault, one may hypothesize that the western ring fault is the more active one.

The orientation of the ring fault is not constrained in this study and is hence depicted as vertical in Fig. 3.11. Consequently, whether the ring fault and the sill-like deformation source are linked remains an open question. One could assume that the ring fault connects the arcuate fracture system at surface to the edge of the inferred sill-like source over a vertical distance of 3.4-6.1 km (Fig. 3.11). If so, then along a N-S cross section, where the source and arcuate fracture diameters are 6 km and 10 km respectively, the fault dip is inward at $60 - 72°$. Along an E-W profile, where the source and arcuate fracture diameters are 7 km and 14 km respectively, the ring fault dip is inward at $44 - 60°$. Even if there is no geometric linkage between the ring fault and sill, its peripheral location from the subsidence source points to the ring fault being inward-inclined and normal. This is evident from analog and numerical models of ring fault formation (e.g. (Roche et al. 2000, Holohan et al. 2011). In this case, the sill and the ring fault have a kinematic linkage.

Another outstanding question is whether the ring fault and the inferred sill-like source are genetically related. At Rabaul volcano (Table 3.1), for example, the active ring faults were generated during a major subsidence and eruption event many centuries prior to their reactivation during a recent uplift event. In this case, the magma body causing reactivation of the ring faults was very unlikely to be genetically linked to the ring-fault's formation (Saunders 2001). A similar scenario may have occurred at Tendürek, for several reasons. Firstly, the aspect ratios of the inferred sill-like source and the arcuate fracture system are quite different (1.17 vs. 1.4). Secondly, they are off-centered from each other (Fig. 3.9). Thirdly, the optical data indicate that the arcuate fractures, and hence the underlying ring fault, were formed at least 13,000 years ago (Yılmaz et al. 1998), as they are cross cut by lava flows from the summit (Fig. 3.10e). Fourthly, inward inclined normal faults may lead to a space problem at depth during subsidence (Branney 1995). Therefore, (a) fault geometry at depth is more complicated, or (b) the reservoir size during the formation of the ring faults, has been significantly larger than today, leading to a more vertical or even outward dipping ring fault geometry (Fig. 3.11). The Tendürek ring fault may hence have been generated much earlier, either in a collapse event or an uplift event, and reactivated during the slow subsidence that occurred in the period of our observation.

Activity along ring faults is usually observed during catastrophic events or 'unrest' periods at volcanoes (Tab. 3.1, references therein). For example, active ring faults have been detected or observed during collapse caused by magma withdrawal (Miyakejima, Dolomieu, Fernandina) and during uplift caused either by magma intrusion (Rabaul, Sierra Negra) or possibly also by hydrothermal activity (Campi Flegrei). The durations of these events ranged from several days to months, and the magnitudes of the associated surface displacement ranged from several meters to several hundreds of meters (Tab. 1). In contrast, the duration of ring fault activity at Tendürek volcano was at least eight years and possibly several decades, and the magnitude of associated surface displacement was on the order of several centimeters. Moreover, Tendürek volcano was apparently dormant during this time, and so there is no obvious link to concurrent magma intrusion or withdrawal. Our study at Tendürek therefore provides an alternative example of long-term slip along ring faults that, as proposed by (Walker 1984), is driven by processes other than rapid magma intrusion or withdrawal.

3.7. Conclusions

InSAR derived measurements show that Tendürek volcano has subsided continuously between 2003 and 2010. The maximum detected subsidence over this period was 7-8 cm, corresponding to a rate of 11 mm/yr. The linear part of our observed subsidence signal can be best explained by a near-horizontal, contracting, sill-like body that lies at a depth of 0.8-3.1 km b.s.l. and that has lateral dimensions of about 6 x 7 km. The body's total estimated volume change over the eight year observation period is $\sim 4.55 \cdot 10^{-3}\, km^3$. Sagging or spreading of Tendürek volcano are unlikely deformation mechanisms, as the required weak sedimentary layers are located at a much shallower depth than the modeled source. Partial solidification of a sill or flat-topped reservoir can more readily explain the modeled volume change, although contributions to this from cooling, degassing, and/or hydrothermal activity cannot be excluded.

The residual displacement field shows gradients coinciding with an arcuate fracture system that is only developed on the southern flank of Tendürek volcano. These displacement gradients also continue around to the northern flanks, however, and so form a complete ellipse around the volcano. These gradients and the associated arcuate fracture system likely represent the surface expression of slip on a blind ring fault that encircles Tendürek volcano.

From optical data, we find that basaltic lava flows from the summit cross and bury parts of the arcuate fracture system on the eastern flank of the volcano. Although the absolute age of these lavas is poorly constrained, they are probably at least 13,000 years old (Yılmaz et al. 1998). The arcuate fracture system, and consequently the ring fault, must thus be older than this age. As seen at other volcanoes, for example Rabaul (Saunders 2001), the ring fault at Tendürek is therefore probably an inherited structure that has been reactivated during the recent hydrothermal or magmatic activity at the volcano.

Finally, our study of Tendürek volcano shows that ring faults may slip not only due to magma movements and catastrophic eruptions (Lipman 1997), but also due to magmatic or hydrothermal processes causing long-term subsidence (Walker 1984) at otherwise dormant volcanoes.

3.8. Acknowledgments:

We appreciate fruitful discussions with Mehdi Nikkhoo and constructive and critical comments of reviewers on an earlier manuscript. This work was financially supported within the framework of the PROGRESS project funded by the German Ministry of Education and Research (BMBF), the Helmholtz Alliance “Remote Sensing and Earth System Dynamics”, and the GFZ Potsdam. In addition, Holohan acknowledges a Marie-Curie International Fellowship co-funded by the Irish Research Council and Marie-Curie Actions. The data used were acquired by the European satellite Envisat and provided via the ESA proposal ID 3589 and 3455. RapidEye data was provided via the RESA proposal “Beobachtung von Vulkanen und deren Kopplung zu Erdbeben in Vorderasien”. The photo of Tendürek volcano in Fig. 3.2 was kindly provided by Ms. Grete Howard.

4. A 3D boundary element model of ring-faulting at Tendürek volcano

H.Bathke[1], *M.Nikkhoo*[1], *E.P.Holohan*[1], *T.R.Walter*[1]

(1) Department 2. Physics of the Earth, Helmholtz-Centre Potsdam, GFZ German Research Centre for Geosciences, Telegrafenberg, 14473 Potsdam, Germany

4.1. Abstract

Calderas are commonly considered to be structurally bounded by steep normal faults, encircling a caldera basin with diameters exceeding kilometers. Recently, the presence of oblique slip at subsiding calderas has been affirmed from analog models and geologic observations. At Tendürek volcano in Turkey, a significant horizontal motion along the ring-fault structures has been measured geodetically by using InSAR. Analytical source models of a contracting sill-like source were able to represent the main observed signal to some point of extent, but yet foundered to explain the observed displacements along the ring-faults. We performed detailed boundary element modeling under consideration of the real topography, realistic ring-fault geometries and the interaction of the sill-like source with the ring-faults. The comparison of our modeling results to analog experiments shows that the ring-faults at Tendürek might be composed of outward-inclined reverse faults on the western flanks and of inward-inclined normal faults on the eastern flanks of the volcano. In this setup the cooling-contracting sill-like source might be the cause for a "sliding-trapdoor" effect. These results have been compared to the outcomes of analog experiments, which show similar different fault dip orientations at either side of the caldera. Hence this study is a first geodetically measured proof for the existence of oblique slip faulting at calderas.

4.2. Introduction

Many volcanoes show evidences for unrest, coming along with surface displacements. These are worldwide quantified by satellite radar techniques (Ebmeier et al. 2013) and suggest the presence of magma-chambers in most cases. The parameters of such sources are usually estimated through analytical source modeling. However, at volcanoes the magmatic source is often accompanied and it interacts with other complex sources of deformation (Walter and Troll 2003). If the existing additional deformation sources are included into the model setup, the inferred source parameters of only a magmatic source will be changed significantly (Beauducel et al. 2004).

Taking aim at this, numerical modeling techniques, such as the finite element method (FEM) or the boundary element method (BEM) are used more often nowadays (Bonaccorso et al. 2005, Fukushima et al. 2005, Wauthier et al. 2012). Nevertheless, the high computational load and the often limited constraint of only surface displacement data on the inverse problem, make this investigation challenging.

In addition to a sill-like source, we have found a strong evidence for the presence of ring-faults at Tendürek (Bathke et al. 2013). Therefore, we used the BEM to construct an improved model of the volcano that consisted of the magmatic sill and ring-faults. Considering the topographic elevation changes and interaction of these sources, we inverted for the deep source geometries and strengths. We have discovered the sill (BEM), being located at the depth from -2.7 to -3.1 km a.s.l. is within the range of the model uncertainties of the analytical Okada source models from-0,8 km to -3 km a.s.l. (Bathke et al. 2013). The size of the source (1 x 1 km BEM Sill) is significantly smaller though (6 x 7 km Okada plane).

The models also reveal that our InSAR time series data provides little constraint on the dip angle of the ring-faults at Tendürek. However, under the consideration of physical and geological constraints, it is most plausible that the ring-faults consist of outward-inclined reverse faults at the western flanks and of inward-inclined normal faults at the eastern flanks of the volcano. This geodetically observed source setup at Tendürek volcano is an example for ring-faulting, resembling a trapdoor-like faulting mechanism that has been observed in analog models similarly (Holohan 2008, Holohan et al. 2013).

4.3. Data and methods

4.3.1. InSAR data at Tendürek volcano

We have generated two time series of the displacement fields at Tendürek volcano, from Envisat data of the ascending and descending satellite tracks, by using the small baseline subset module of the StaMPS software (Hooper et al. 2012). Details on the data processing are described in (Bathke et al. 2013). The data covers the periods 2004-2008 and 2003-2010, respectively. The linear component of the displacement velocity points out a maximum of $\sim 11mm/yr$ in radar line-of-sight at the summit of the volcano for both satellite tracks (Fig. 4.1 top panels). This signal reduces to $\sim 6mm/yr$ and $\sim 2mm/yr$ at the flanks and the foot of the volcano, respectively.

Analytical source modeling by using an Okada source showed that an optimum sill-like source would be located sub-horizontally beneath the western crater at -0.8 to -3.0 km above sea level, with a spatial extent of 6 x 7 km and an annual contraction of $\sim 1-3$ cm (Fig. 4.1 left, middle panels).

We used these optimum Okada source parameters to calculate a synthetic forward model to get the residual surface displacements, which cannot be explained by the sill-like source (Fig. 4.1 left, bottom panels). The residuals represent high gradients in displacement that follow an arcuate fracture system at surface (Bathke et al. 2013). We hypothesized that these fractures are surface expressions of ring-faults.

In this work we use boundary element modeling to construct a more realistic model of the deformation sources at Tendürek, including realistic topography, an elliptic sill-like source as well as our proposed ring-faults that follow the arcuate fracture system.

4.3.2. Boundary Element Method (BEM)

The boundary element method is a numerical method that allows constructing complex deformation source models by using triangular dislocation elements (TDE) in an elastic full space. Such complex deformation sources may be curved faults or irregular magma bodies for instance. Meshes of interacting TDEs may resemble the boundaries of the inverse problem. By introducing traction or displacement boundary conditions on the elements of each mesh we solve for the displacement discontinuities. Comparing the synthetic displacements at surface of our model with measured displacements, we invert for the displacement boundary conditions on the complex subsurface deformation source(s).

Dislocations (here triangular) are displacement discontinuities (DD), such as for example

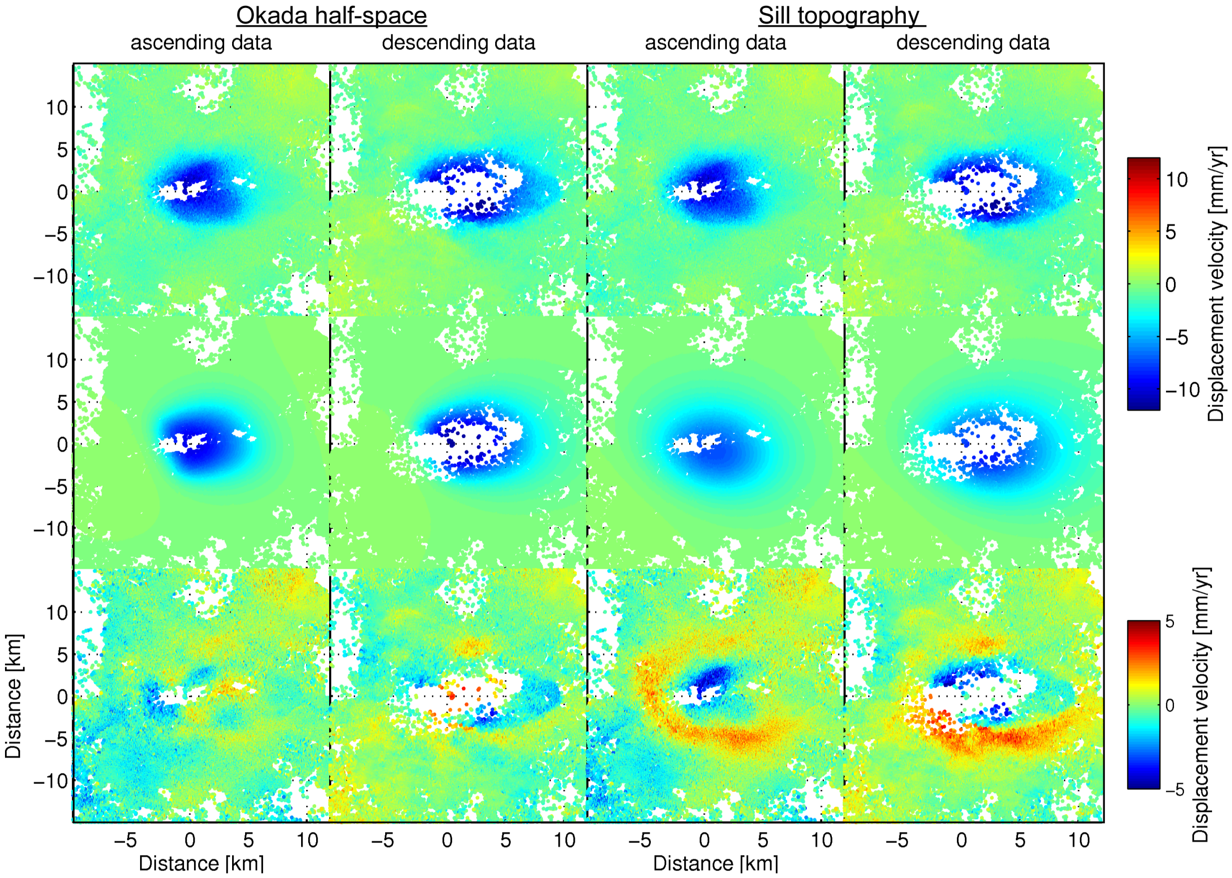

Figure 4.1.: Left columns: Analytical Okada source model; right columns: 3D sill-like source. Top panels: Displacement velocities for the ascending and descending tracks, respectively. Middle panels: Modeled optimum displacement velocities by using an Okada source and a 3D sill-like source for the ascending and descending tracks, respectively. Bottom row: Residual displacement velocities in each satellite track for the Okada source and the 3D sill-like source, respectively.

the tips of an extending crack (Scavia 1991). On both sides of such a DD, the material is oppositely displaced (Cayol and Cornet 1997). The amount of displacement or traction along a dislocation can be expressed with harmonic functions that may be constant, linear, quadratic or of even higher order (Cayol and Cornet 1997, Shou et al. 1997). Here we use constant shape functions.

We also account for topographic effects on the modeling results. A mesh of the real topographic surface can be constructed from traction free dislocations in full space by using a digital elevation model (Cayol and Cornet 1998). By solving for the displacements on the dislocations of this mesh, the effect of topography is included into our models (Nikkhoo et al. manuscript in preparation).

4.3.3. Model setup

The BEM requires to discretize the boundaries of the sources as well as the free surface in the full-space, which is assumed to be homogeneous with a Young's modulus of 33 GPa and a Poisson's ratio of 0.25. We tested different model setups consisting of sources represented by meshes: the first mesh resembles the surface topography, the second a contracting sill and the last the ring-faults.

We tested all the following model-setups under consideration of real topography and source interaction: 1) A contracting sill-like source only. 2) A contracting sill-like source surrounded by inward-inclined ring-faults constrained with uniform dip-traction. 3) The same case like 2), but with outward inclined ring-faults. 4, 5) After determining the optimum source geometry for case 2) and 3) we solved for distributed slip and opening along the ring-faults and the sill, respectively.

We have used the SRTM digital elevation model with 90 m resolution (Farr et al. 2007) to create the mesh of 3881 triangular dislocation elements (TDE) for the surface topography. The sill is expressed by an ellipse composed of a mesh of 24 TDEs. The ring-faults are resembled by a truncated cone consisting of 224 triangular dislocation elements. We have used the high gradient of displacement in the residual map of the descending track (Fig. 4.2a) to digitize the upper edge of our inferred ring-faults. The walls of the truncated cone are adjusted in the way that they follow the trace of the gradient of high displacement in the residual (Fig. 4.2b). Finally we have cut the cone into 4 quarters (cuts at 0,90,180,270 azimuth) to allow the variability in dip-traction along the ring-faults (table 4.1, column 1).

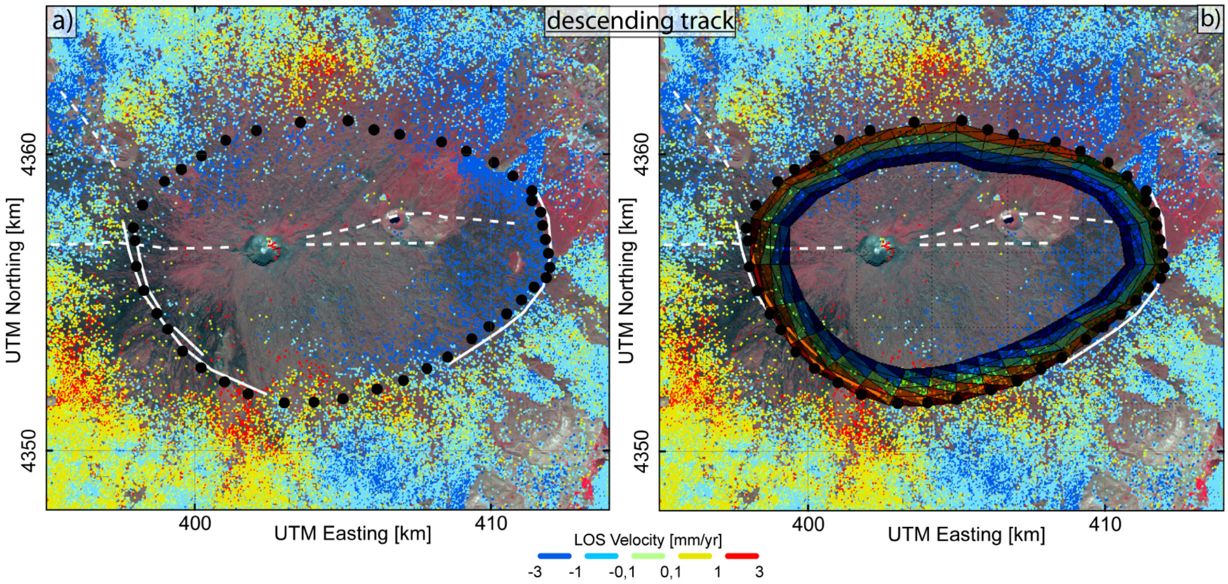

Figure 4.2.: Okada source residual displacement of the descending track. White lines (solid and dashed) show observed and inferred fractures modified after (Yılmaz et al. 1998)(see also (Bathke et al. 2013)). a) Black dots mark the digitized surface trace of the inferred ring-faults. b) The colored mesh resembles the ring-faults that are included into the boundary element model.

4.3.4. Optimization for general source geometries

The initial aim of our optimizations was to find the optimum geometric parameters for the sources of the following model setups, which could explain the previously presented mean displacement velocities in a best way. As the optimization algorithm we have used a genetic algorithm with the parameters: 40 chromosomes, 100 iterations, 0.5 selection and 0,22 mutation. We have been repeating the optimizations for each following model setup ten times.

Sill-like source

To test whether the inclusion of the inferred ring-faults into the model setup is reasonable, we optimize for the parameters of only a sill-like source in addition to real topography. In comparison to the results of the analytical Okada source modeling, we roughly estimate the influence of the real topography on the modeling results.

Sill and Ring-faults source geometry: uniform dip-traction

To determine the general source geometry of the interacting discretized sources, sill and ring-faults, we use an uniform traction constraint in the dip direction of the ring-faults. In addition we constrained the dip angle of the ring-faults to be either inward- or outward-inclined, between 60 and 90 degrees relative to the horizontal. The dip-traction of the ring faults was set to be smaller, than the contracting traction of the sill, to make sure that the sill was the driving force in the model.

4.3.5. Inversion for slip distribution

Once the main source geometries have been determined, the boundary condition of uniform traction of the sources can be discarded, which allows to invert for distributed slip along the TDEs. Hence the actively slipping parts of the investigated sources that have the largest contribution to the observed displacement can be identified. With reasonable constraints in the inversion for distributed slip, it is possible to gain further insights into the investigated deformation source process(es).

In this case we inverted for distributed slip in strike-slip and dip-slip direction along the ring-faults and distributed opening along the sill following the procedure of (Jónsson et al. 2002):

$$\mathbf{d} = \mathbf{G} \cdot \mathbf{m}_{opt} \tag{4.1}$$

Where d are the surface displacements, m_{opt} is a vector with the optimum slip distribution along the TDEs and **G** are the Green's functions that relate the model vector to the data. To constrain this over determined inverse problem, a smoothing matrix- the discrete Laplacian operator **D** and a smoothing weight κ have to be introduced. Together they define the roughness ρ of the model solution, i.e. the differences in slip m_{opt} between neighboring TDEs (Maerten et al. 2005).

$$\begin{bmatrix} \mathbf{d} \\ 0 \end{bmatrix} = \begin{bmatrix} \mathbf{G} \\ \kappa\mathbf{D} \end{bmatrix} \cdot \mathbf{m}_{opt} \tag{4.2}$$

On the one hand high κ- values will force the inversion to produce smooth slip distributions and low κ- values will allow the slip to vary quite rapidly between neighboring patches on the other hand. These two extremes have to be balanced to find a reasonable slip-distribution.

For a geologically meaningful solution, we constrained the dip-slip to be negative. With a constrained L2-norm least-squares inversion under the consideration of different smoothing weights κ, we calculate the misfit (RMSE):

$$f = \sqrt{\frac{\mathbf{v}^T\mathbf{v}}{N}} \tag{4.3}$$

where $\mathbf{v} = \mathbf{d} - \mathbf{A} \cdot \mathbf{m}_{opt}$ and $\mathbf{A} = \begin{bmatrix} \mathbf{G} \\ \kappa\mathbf{D} \end{bmatrix}$ is the residual surface displacement and N is the number of observations. The solution roughness is defined by (Jónsson et al. 2002):

$$\rho = \frac{\sum_{i=1}^{M} |p_i|}{2 \cdot M_{ring} + M_{sill}} \tag{4.4}$$

with $M_{ring/sill}$ number of TDEs in the mesh of the ring-faults or sill; and $p_i = D \cdot \mathbf{m}_{opt}$ for each solution. To determine the smoothing weight κ we calculate a κ cost-function:

$$\kappa_{cost} = \sqrt{\frac{f^2}{max(f)} + \frac{\rho^2}{max(\rho)}} \tag{4.5}$$

The minimum of κ_{cost} indicates the optimum global kappa weighting factor that produces the smallest residual displacements with a low roughness of the solution vector (red points in Fig. A.15).

4.4. Results

In this section we describe the results of the three main model setups. The first depicts the sill beneath a topographic crack that partially explains the data, but leaves a significant elliptic ring structure in the residual displacements. In the second, we added a ring-fault to the model to account for the ring shaped residual displacements. In the third we solve the inverse problem for the slip distribution in strike-slip and sip-slip direction on the ring-faults, as well as for the opening on the sill.

4.4.1. Sill and real topography

Considering the real topography, the center of the optimum sill-like source is located at -4.0 km a.s.l. It has a dip angle of 20° towards the south-east, and it contracts with a traction of -1.3 MPa/yr. The length of the major and minor axes are 6.5 km and 3.5 km, respectively.

The residual displacements in the range of +/-5 mm (Fig. 4.1, bottom panels) show a spatially correlated elliptical ring around the volcanic edifice in both satellite tracks. We used the optimum source parameters for the sill-like source and calculated the synthetic displacement velocities on a flat surface at an elevation of 1,900 m, which is the mean elevation in the vicinity of Tendürek volcano (Fig. A.16, right middle panels). Comparing the synthetic displacements of these two forward models of the sill-like source, we have discovered that in this case, the influence of the topography on the synthetic displacement velocities was around 3 mm in radar line-of-sight. Hence, by using a flat surface, the synthetic displacement velocities are overestimated and depend on the reference elevation. This result is in agreement with the work of Cayol and Cornet (1998), who used a Mogi source.

4.4.2. Sill and inward-inclined ring faults

The optimum solution of our inversions for the inward-inclined ring-faults shows that the upper edge of the ring-faults is located at 2.0 km a.s.l. The faults have a width of 2.8 km and a dip of 70°. The 4 patches of the ring faults have a traction of -0.008 to -0.034 MPa, where the first one is located in the upper right quadrant (North-East). The other ring fault patches, two-three-four follow counter clockwise (table 4.1).

The optimum sill has an elliptic dimension of 0.8 x 1.9 km and is located at a depth of -3.1 km a.s.l. under the western crater. It has a plunge of 23° towards the south-east and a contracting traction of -7 MPa. The position of the inward-inclined ring-faults and the sill below the volcanic edifice are shown in Fig. 4.3a.

The synthetic displacements of the forward model (Fig. 4.4 left, middle panels) can fit the elliptic shape of the observed displacement very well. Nevertheless, there is a spatially correlated ring-like structure in the residuals, visible all around the volcanic edifice. Residual displacements are within +/-3 mm for the ascending track and within +/-5 mm for the descending track (Fig. 4.4 left, bottom panels).

4.4.3. Sill and outward-inclined ring faults

The optimum solution of our inversions for the outward-inclined ring-faults makes clear that the upper edge of the outward-inclined ring faults is located at 2 km a.s.l., which is somewhat deeper than the inward-inclined faults. Compared to the inward-inclined case, the faults are less wide with a width of 1.8 km but steeper with a dip of 80°. The 4 patches of the ring faults have similar traction of -0.007 to -0.045 MPa (table 4.1).

In this case the sill is almost circular ($\sim$ 1.0 x $\sim$ 1.0 km). Located at a depth of -2.7 km

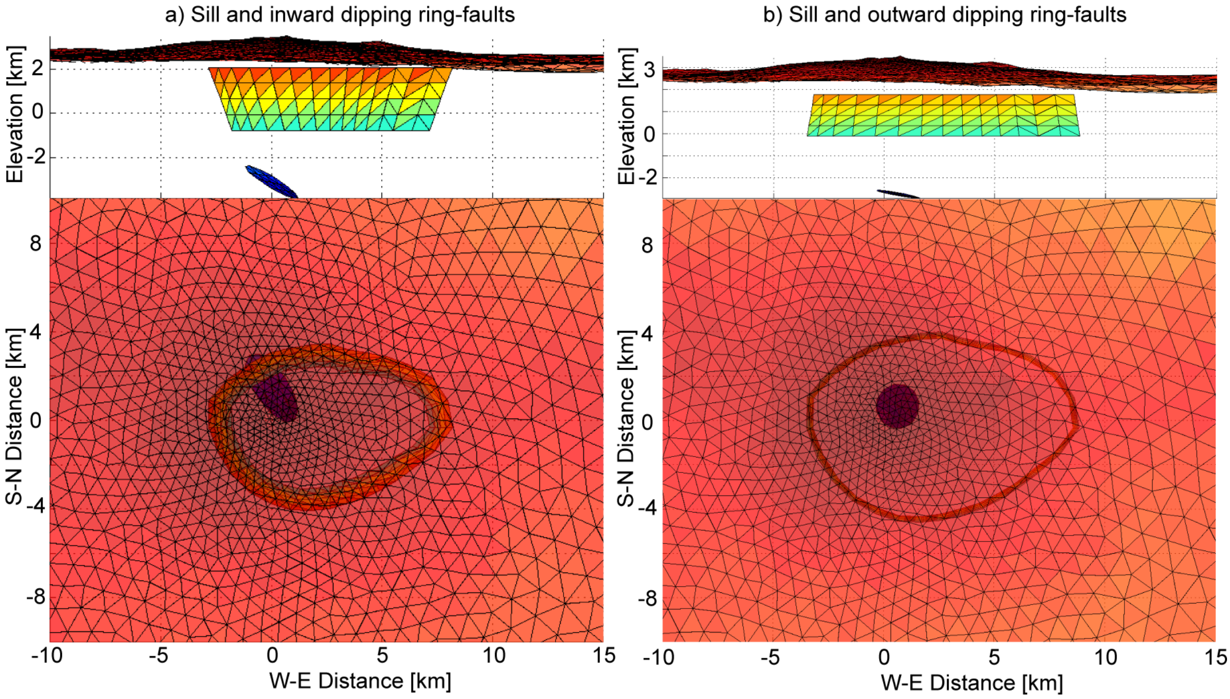

Figure 4.3.: Meshes of the topographic elevation, the optimum sill-like source and the optimum ring-faults. a) Inward-inclined ring-faults. b) Outward-inclined ring-faults.

a.s.l. under the western crater, it has a plunge angle of 11° towards the east and a high contracting traction of -12 MPa. The arrangement of the outward-inclined ring-faults and the sill below the volcanic edifice are shown in Fig. 4.3b.

The data fit of the synthetic displacement of the forward model (Fig. 4.4 right, middle panels) seems to be somewhat better for both tracks, than for the inward-inclined case. The spatially correlated ring-like structure in the residual all around the volcanic edifice is less visible (Fig. 4.4 right, bottom panels). Residual displacements are within the same bounds as for the inward-inclined setup, but the general model fit seems to be better.

4.4.4. Distributed slip inversion

The inversions for distributed slip show the global minimum of the κ_{cost}- function (equa. 4.5, red dots in Fig. A.15). It produces the best fit to the data (Fig. A.17) though, but the solution roughness is still high. Hence the strike-slip component varies rapidly with depth, which is geologically meaningless (Fig. A.18).

The next local minimum of the κ_{cost}-function (green dot Fig. A.15) produces higher data misfits (Fig. 4.5), if compared to the global minimum. However, the residuals are smaller for the inward-inclined ring-faults on the eastern flank of the volcano in comparison to

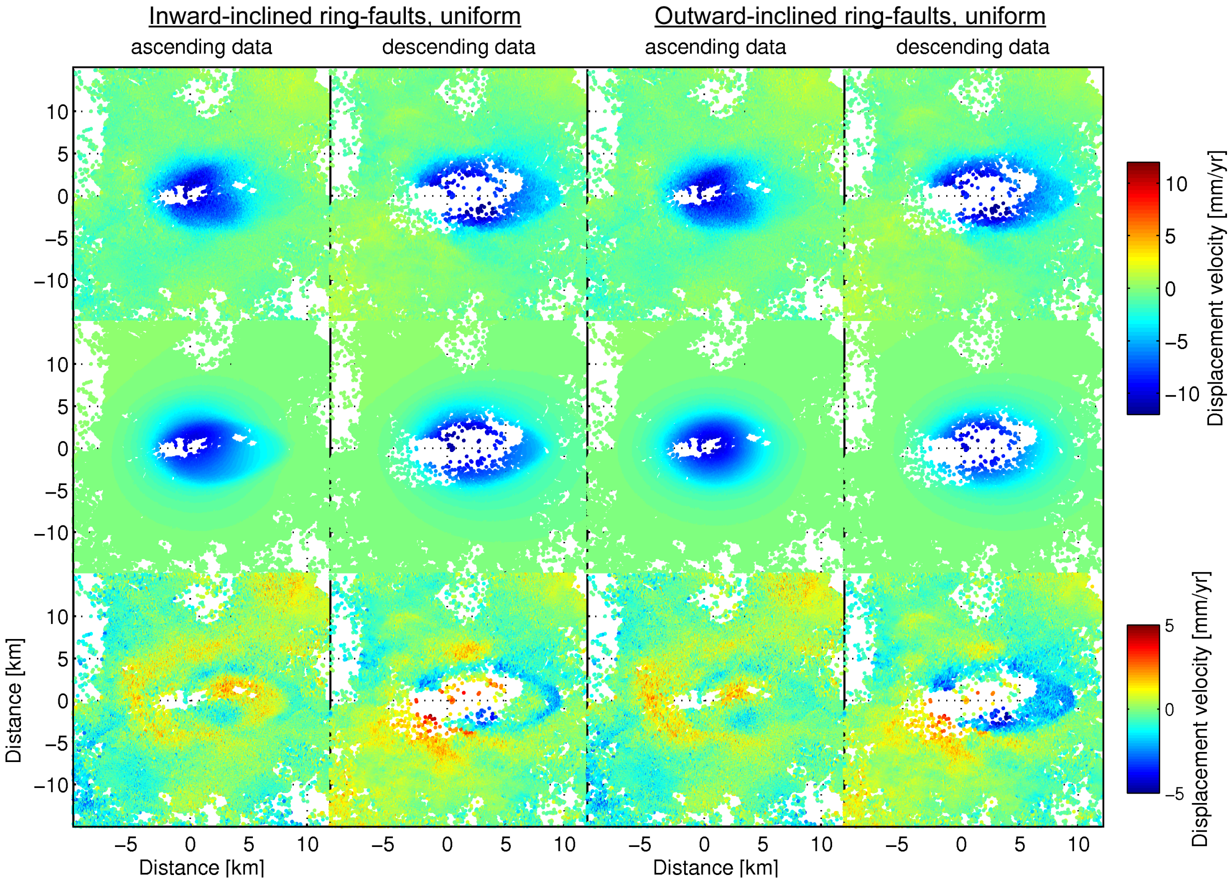

Figure 4.4.: Uniform dip-traction solution: Left columns: Sill-like source and inward-inclined ring-faults. Right columns: Sill-like source and outward-inclined ring-faults. Top panels: Displacement velocities for the ascending and descending tracks, respectively. Middle panels: Modeled optimum displacement velocities for the ascending and descending tracks, respectively. Bottom row: Residual displacement velocities in each satellite track for the inward- and the outward-inclined ring-faults and a sill-like source, respectively.

the outward-inclined ring-faults and vice versa. The residuals are smaller for the outward-inclined ring-faults on the western volcano flanks.

The adequate low roughness results in less variable strike-slip fault-patches (Fig. 4.6). For both scenarios, the inward- and outward-inclined ring-faults, shows the north-western ring-fault quadrant dextral strike-slip sense compared to a sinistral strike-slip of the south-western fault-quadrant. The eastern parts of the ring-faults are either nearly stable or have a small dextral strike-slip component (Fig. 4.6, top panels).

The dip-slip component is the largest in the western quadrants, and it increases with depth. Comparing to that, there is a slip decrease with depth at the north-western quadrant for the inward-inclined faults (Fig. 4.6, bottom panels).

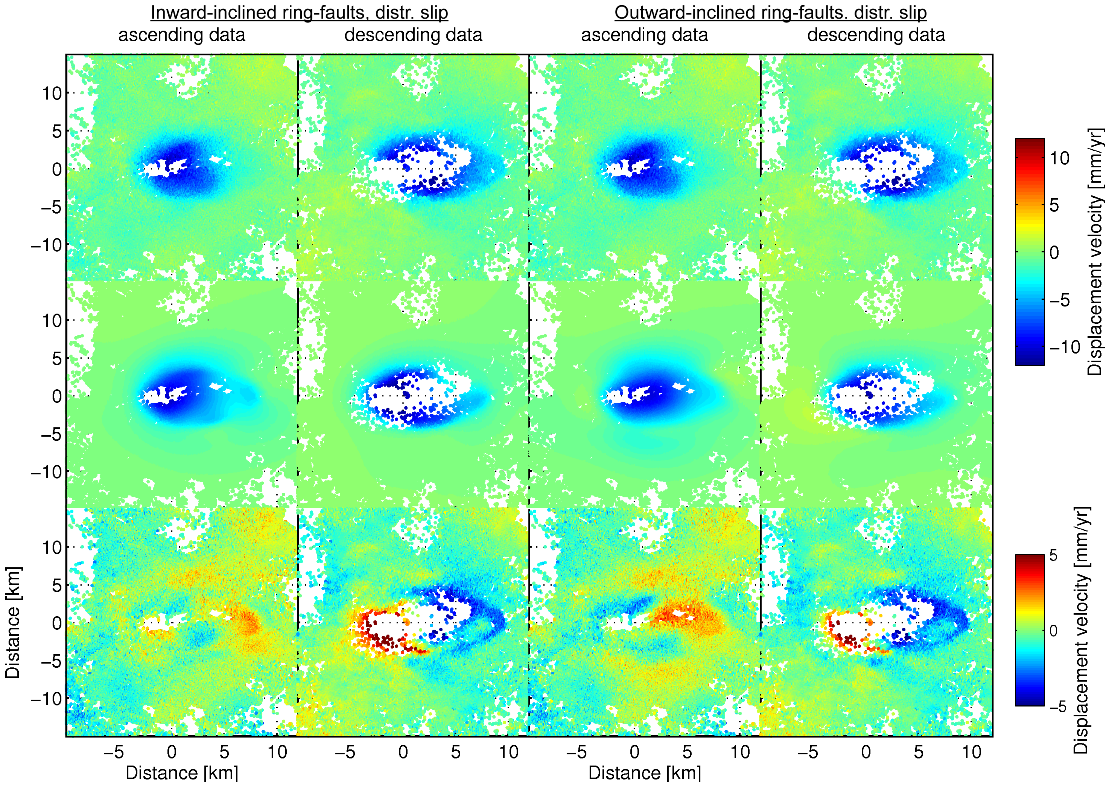

Figure 4.5.: Distributed slip data fit for global minimum κ_{cost}: Left columns: Sill-like source and inward-inclined ring-faults. Right columns: Sill-like source and outward-inclined ring-faults. Top panels: Displacement velocities for the ascending and descending tracks, respectively. Middle panels: Modeled optimum displacement velocities for the ascending and descending tracks, respectively. Bottom row: Residual displacement velocities in each satellite track.

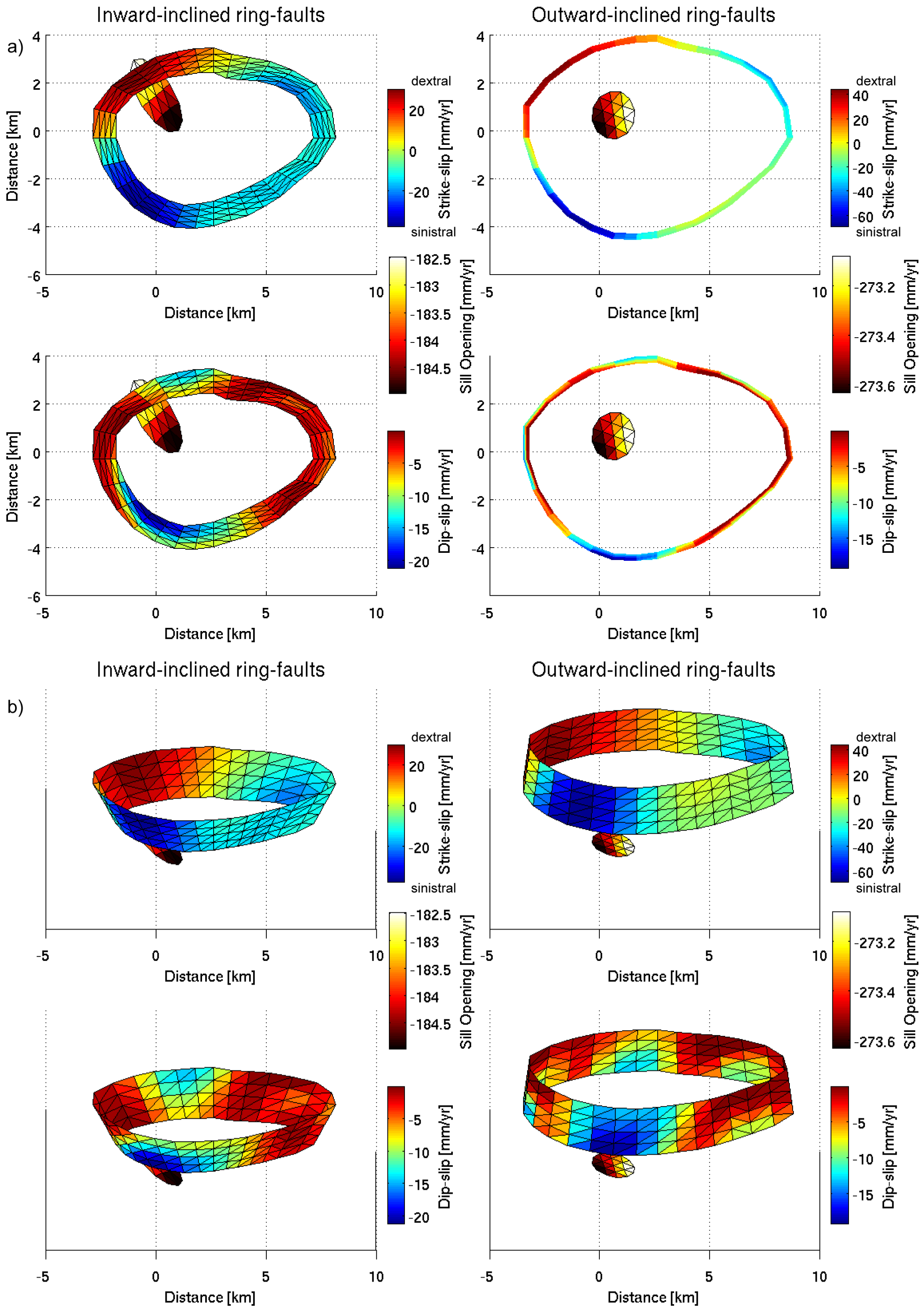

Figure 4.6.: Distributed slip for local minimum κ_{cost}: a) Top view: Left: Inward-inclined ring-faults. Right: Outward inclined ring-faults. Top panels: Estimated strike-slip distribution; red and blue colors represent a dextral and sinistral strike-slip direction, respectively. Bottom panels: Dip-slip distribution; red and blue colors show stable and slipping elements, respectively. b) Perspective view, same as a).

Table 4.1.: Optimization results: Parameters for the Sill and the ring-faults.

Sill and Ring-faults models		
Parameters	Inward-inclined	Outward-inclined
Sill		
Major axis [km]	0.8	1.0
Minor axis [km]	1.9	1.0
X Distance [km]	-0.02	-0.63
Y Distance [km]	-1.46	-0.64
Depth (a.s.l) [km]	-3.1	-2.7
X rot [°]	-23	1
Y rot [°]	-9	11
Z rot [°]	322	199
Traction [MPa]	-7.14	-12.03
Ring-fault		
Width [km]	2.8	1.8
Dip angle[○]	70	80
Axis Scaling	0.78	0.83
Depth upper edge (a.s.l.) [km]	2.0	1.8
Traction Quadr. 1 [MPa]	-0.018	-0.020
Traction Quadr. 2 [MPa]	-0.020	-0.018
Traction Quadr. 3 [MPa]	-0.008	-0.045
Traction Quadr. 4 [MPa]	-0.034	-0.007

4.5. Discussion

We used the boundary element method to test several model setups for the possible deformation sources that might be present at Tendürek volcano: 1) A sill-like source with real and flat topography 2/3) sill-like source and inward/outward inclined ring-faults with uniform traction 4/5) sill-like source and inward/outward inclined ring-faults with constrained distributed slip.

The models were constrained by the mean velocities of two displacement time series from the ascending and descending Envisat satellite tracks. With surface displacement data only, it is not clearly distinguishable whether the ring-faults are inward or outward inclined. In the following section we discuss the model assumptions and the interpretation of the results.

4.5.1. Modeling Assumptions

Our models give new insights into the deformation sources acting at Tendürek. Nevertheless, the modeling results depend on the model assumptions and the applied boundary conditions. Changing these might affect the parameter values.

We take into account the influence of topography (Cayol1998, Walter2006) and complex sources, but the integration of a heterogeneous crust might change the modeling results (Manconi et al. 2010, Wauthier et al. 2012). Unfortunately, we do not have further constraint on crustal properties from seismic or gravimetric data, so we decided to assume a homogeneous subsurface for simplicity.

We presume a constant dip angle along the ring-faults, which is very unlikely to be true in reality, as we can see it at Rabaul caldera for instance. The dip angle of the faults varies there with depth and along strike (Saunders 2001). The deficiencies in the mathematical approximation and the geometry of the fault mesh, combined with data uncertainties, hardly allow resolving more detailed models.

The data fit of the uniform traction results is significantly better, if compared to the results of the distributed slip inversions. This is justifiable, as the degree of freedom is larger for the uniform traction models, where the TDEs can slip in each direction. The distributed slip inversions have strong constraints in the allowed slip-directions and are therefore more meaningful geologically.

The fit of our boundary element models is not significantly better compared to the simple analytical models. The probably most important point for this is that the faulting mechanism at the ring faults may not be purely double couple. We hardly see a ring of uplift in the vertical displacement component (Fig. A.13) around the volcano. In the mathematic formulation however, the dislocation elements always have a double couple mechanism. This causes a significant uplifting displacement component outside of the ring-structures that largely affects the misfit in the optimization.

Ring-faulting at calderas may be double couple as seen at Dolomieu (LaRéunion) or Sierra Negra (Jónsson 2009). However, presumably due to the slow movement and/or fault locking at Tendürek, this might not be the case.

4.5.2. Interpretation of model results

Sill-like source-Influence of topography

The model results show that the topography has quite a large influence on the modeling results, because the amplitude of the signal we investigate is very small. If the topography is not accounted for in the inversions, the synthetic displacement is overestimated by $\sim 3\,\mathrm{mm}$ in this case with a reference height of 1,900 m. This will change dependent of the reference height for sure.

Consequently, the data fit of the Okada source inversion might have been better, only because the overestimated part of the signal has accounted partially for the displacement, caused by the ring-faults by chance.

When including the topography into the model setup, it is clearly visible that a sill-like source only cannot explain the observed displacement (Fig. 4.1 right panels). Therefore, we discard this possible model setup as a reasonable source for the displacement that has been observed at Tendürek and discuss in the following section the ring-fault model setups.

Sill-like source and ring-faults

Based on the model results and residuals only, we can hardly tell which of the inward and outward dipping ring-fault models is more likely to be more truthful. Nevertheless, when taking into account the analog model results from (Holohan 2008) it seems like we have neither the pure inward- nor the pure outward-inclined case at Tendürek.

In his analog experiment Holohan (2008) had been depleting a magma reservoir off-centered (Fig. 4.7a) and observed the outward-inclined reverse faults, developed near the point of depletion. On the other hand there were inward-inclined normal faults, formed on the opposite side (Fig. 4.7b). Moreover at the surface of the reservoir Holohan (2008) observed a strong horizontal displacement pointing towards the point of depletion.

If we apply this model to Tendürek, the cooling-contracting sill-like source below the western summit would resemble the point of depletion in the analog experiment and would be its driving force. Consequently, we might have inward-inclined faults at the eastern volcano flanks and outward-inclined faults at the western volcano flanks. This largely coincides with the observed residual displacements of our distributed slip models. The residual displacements for the inward- and outward-inclined ring-faults are small at the eastern and western volcano flanks, respectively (Fig. 4.5, bottom panels). Although the residual displacements are still quite large for both separate cases, an implementation of the proposed fault geometry with inward- and outward inclined faults would presumably lead to a much better data fit.

Holohan et al. (2013) propose a strike slip component along ring-faults caused by non-uniform subsidence of the caldera floor. We observe a large westward directed horizontal displacement component (Fig. A.13a), which implies that the highest slip along the ring-faults is at the western flank. The inverted strike-slip and dip-slip distributions intriguingly support the prediction that the slip along the ring-faults, either inward or outward-inclined, is the largest in the west. This observation corresponds to the surface expressions of the arcuate fractures that are the most prominent on the western volcano flanks (Bathke et al. 2013).

4.6. Conclusions

The subsidence of Tendürek volcano from 2003 until 2010 cannot be explained by only a contracting sill-like source that is centered below the western summit. It is most plausibly accompanied by elliptic concentric ring-faults around the volcano edifice.

The inclusion of the ring-faults affects the size of the sill-like source in the modeling results strongly. The dimensions changed from $6.5 \times 3.5\,\mathrm{km}$ to $1 \times 1\,\mathrm{km}$.

The geometry of the ring-faults can be hardly determined by the surface displacement data only. The inward-inclined normal faults in the east and the outward-inclined reverse faults in the west are the most plausible. The results, gained from analog experiments, confirm these assumptions and observations (Holohan 2008).

Distributed-slip inversions on the ring-faults show that the largest slip occurs on the western ring-faults and confirm the assumptions from Bathke et al. (2013). This outcome is also supported by the arcuate fracture system that is most developed at the western flanks.

Finally our study is a geodetic proof of a “sliding trapdoor”, faulting and oblique slip at volcanoes that has been initially proposed by Holohan (2008), Holohan et al. (2013) from analog experiments.

4.7. Acknowledgments

We appreciate fruitful discussions with Henriette Sudhaus. Very special thanks go to Eoghan Holohan for providing the figure of the analog modeling results. This work was financially supported within the framework of the PROGRESS project funded by the German Ministry of Education and Research (BMBF), the Helmholtz Alliance “Remote

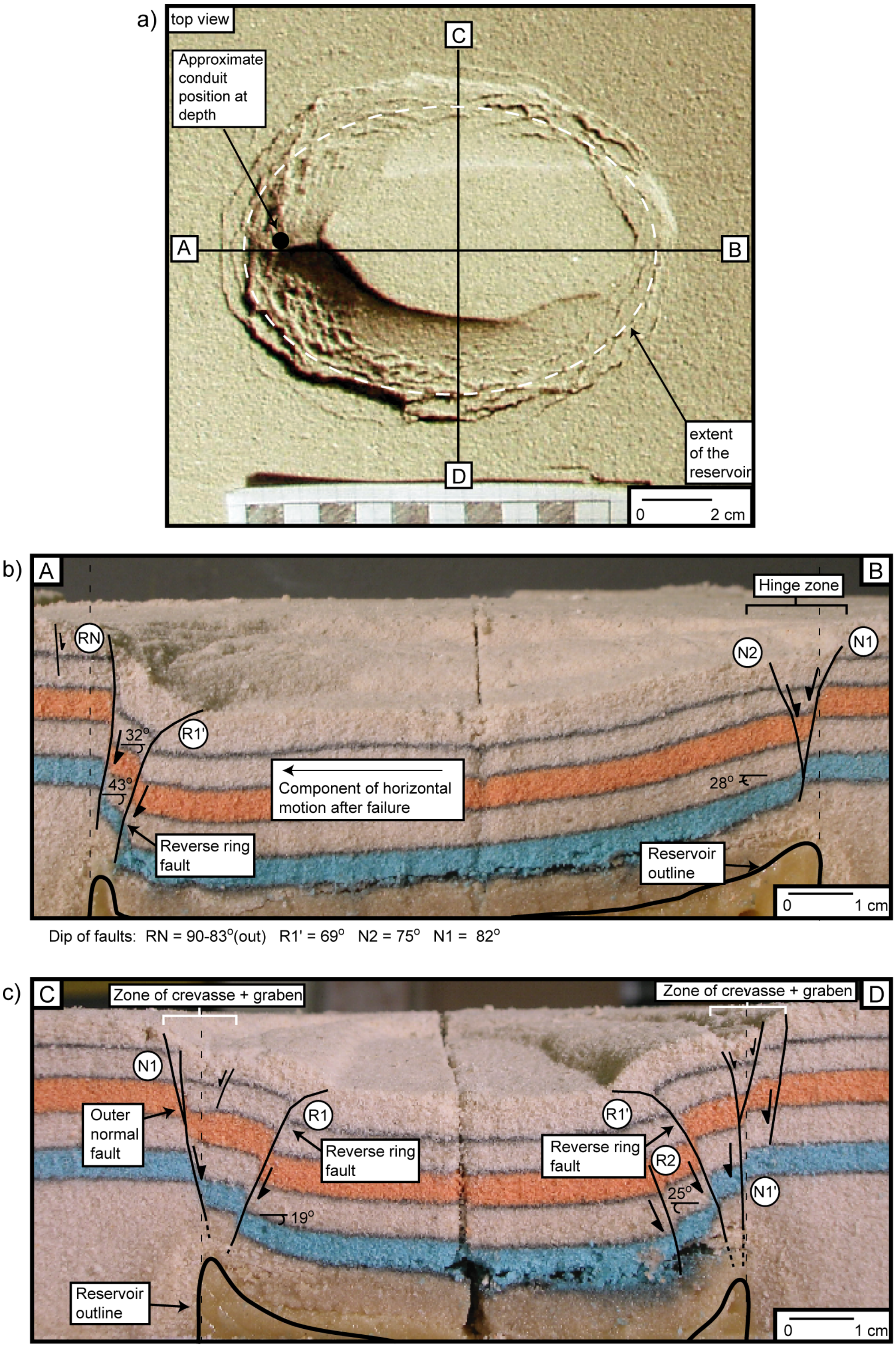

Dip of faults: RN = 90-83°(out) R1' = 69° N2 = 75° N1 = 82°

Dip of faults: N1 = 79° R1 = 65° R1' = 63° N1' = 84° R2 = 66°

Figure 4.7.: Analog experiment results modified from Holohan (2008): a) Top view on the final depleted reservoir. The reservoir has been depleted to the left off-centered of the reservoir (white dashed line). b) W-E Cross section through the model with marked structures that have been developed while the process of subsidence. c) N-S Cross section through the model with marked structures that have been developed during the process of subsidence.

Sensing and Earth System Dynamics", and the GFZ Potsdam. The used data were acquired by the European satellite Envisat and provided via the ESA proposal ID 3589 and 3455. RapidEye data was provided via the RESA proposal "Beobachtung von Vulkanen und deren Kopplung zu Erdbeben in Vorderasien".

5. Data subsampling for source modeling

H.Bathke[1], *H.Sudhaus*[1], *T.R.Walter*[1], *M.Shirzaei*[1,2]
(1) Dept. Physics of the Earth, Helmholtz-Centre Potsdam, GFZ German Research Centre for Geosciences, Telegrafenberg, 14473 Potsdam, Germany
(2) School of Earth and Space Exploration, Arizona State University, Tempe, AZ 85287-6004, USA Corresponding author: HB, bathke@gfz-potsdam.de

5.1. Abstract

For modeling of deformation sources at volcanoes or for earthquake faulting mechanisms, several hundreds of well distributed displacement data points are sufficient to obtain reliable source parameters. Current and upcoming radar satellites however provide SAR data with millions of data points. It is therefore required to reduce these very large data sets without loss of information in the displacement field of investigation. For the purpose of such data subsampling, we have developed an approach that considers the sensitivity of even heterogeneously distributed data points to a given input source model. Our method enables fast propagation of the data error statistics, allowing us to model uncertainties in the source optimization. A comparison to the established Quadtree algorithm with synthetic and real data shows that the new method performs well, especially when applied to displacement time series.

5.2. Introduction

Several processes can cause deformation at volcanic edifices, as there can be magmatic and hydrothermal activity, gravitational spreading, landslides or tectonic movements (Dzurisin 2007). Due to development of better monitoring techniques, modeling and interpretation of the sources of such deformation has also been improved (Ofeigsson et al. 2011, Ali and Feigl 2012, Hooper et al. 2012). Synthetic interferometric aperture radar (InSAR) data have led to a vast increase in the quantity of available data in particular. Although this improves our understanding of even remote volcanoes, we do start to encounter difficulties when analyzing and modeling large data sets. A single interferogram consists of millions of measurements in the form of pixels that contain information about the reflective properties of the surface and the displacement in a certain time span. Moreover, when multiple interferograms are accumulated and combined, we measure even time histories of parameters for a large number of ground points, e.g. (Hooper 2008).

In order to deal with such large datasets, and to understand the underlying geologic processes through source modeling, various spatial subsampling procedures have been proposed. They range from a simple decimation of the number of points (Delouis et al. 2002) to more sophisticated methods that account for the spatial variation of the observed signal (Jónsson et al. 2002, Simons et al. 2002), or include initial assumptions on the deformation process (Lohman and Simons 2005, Funning et al. 2007). To reduce the number of points in a time series, when the pixels are spatially heterogeneously distributed, we have modified the model-based subsampling procedure from Lohman and Simons (2005). It aims to find the optimum distribution of a desired number of subsampled pixels for efficient source modeling automatically and improves the feasibility of data error propagation (Sudhaus and Jónsson 2009).

We have applied this modified designed subsampling approach, as well as the model-independent Quadtree algorithm, to subsample a synthetic displacement data set. We used differently subsampled data sets to search for the parameters of the synthetic deformation source and repeated this procedure with a real displacement data set of Tendürek volcano afterwards. The optimization results are similar for both subsampled data sets in the synthetic and the real case. Consequently, the new subsampling approach appears valid and works as an alternative method that reduces the number of observations in an InSAR data set and allows for a fast calculation of the data-error variance covariance matrix.

5.3. Method: Data reduction through subsampling

A common aim after detecting and measuring surface displacement is, to find the parameters of a certain deformation source model that could cause the observed signal (e.g. the dimensions and the pressure change of a magma chamber below a volcano (Yang et al. 1988), or the location and kinematic parameters of a dislocation source (Okada 1985)). Such a highly non-linear inversion requires a large number of iterations in an optimization algorithm (e.g. genetic algorithm). In combination with a vast amount of observations this process becomes computationally very intensive. For this reason, the spatially dense observations in SAR interferometry need to be reduced through subsampling, to a subset that still contains the information of the original full data set.

The simplest way of data reduction is to uniformly reduce the whole data set by a certain factor. To better resolve areas with high displacement gradients, the point density can be increased in certain target areas, e.g. close to an extended fault (Delouis et al. 2002). With such simple subsampling strategies some information of the full data set can get lost, because the shape of the displacement signal itself is not considered. Therefore as an alternative, image compression algorithms are more often used (e.g. the Quadtree algorithm), which resample the scene at a lower resolution with respect to changes in the displacement signal (Jónsson et al. 2002, Simons et al. 2002). This way the signal information is preserved, along with data noise and artifacts from the data processing, such as unwrapping errors, which unfortunately may hamper the source parameter search later on. To overcome this problem, *a priori* assumptions on the displacement signal of interest can be taken into account, by using a deformation source model to subsample the data (Lohman and Simons 2005).

The abovementioned subsampling methods are the practical procedures of two-pass interferometry, in cases where the single points in the data set have a low noise level and where they are distributed relatively homogeneously. Time series analyses in surface displacement studies, specifically the small baseline subset (SBAS) and persistent scatterer (PS), result in heterogeneously distributed data points. In these cases image compression methods become less efficient, and a combination of both approaches is useful, model-based subsampling and image compression, (Funning et al. 2007).

Meaningful subsampling can also be achieved through looking at the problem from a design perspective, if we consider one pixel in our InSAR time series as a station in an instrument network. Solving the design problem helps us finding the optimum geometric set-up for a network (Dare and Saleh 2000), something often used in geodesy. These design problems have several orders and the first order asks: “Where should the stations of a GPS network be installed in order to measure a specific deformation process?” (Berné and Baselga 2004). From an InSAR subsampling perspective, the question would then be accordingly: “Which pixel do we need to select from our time series velocity?” Next we must consider the second order design problem: determining the weight or importance of each station in the network for recording the deformation signal. Lastly, we consider the third order design problem: the density of necessary observations, i.e. the number of instrument stations or the number of subsampled pixels.

In the following sections we briefly explain the Quadtree algorithm and introduce a new subsampling method deduced from the design problems. The details of how we dealt with the first order design problem are given in Appendix A.4.

5.3.1. Quadtree subsampling algorithm

When using the Quadtree algorithm (QTA) for data subsampling, the information held within the data gets compressed, rather than selectively picked out, as in the DPS method. The number of pixels that are to be combined into one new data point depends on the local gradient of the displacement signal. At high gradients in the data, the compression is less and the sampling remains comparatively dense. At places with small signal gradients the average over many pixels is taken, resulting in sparser sampling.

By applying the QTA to the data, the image is divided into four squares at first, and the mean of the data points in each square is calculated. If the variance of the pixels within a square exceeds a defined threshold, this square is again divided into four patches and the procedure is repeated. The sub-division stops when all variances within the squares are below the threshold, or a minimum square size is reached, which could be the pixel level. The strength of the QTA is that it restores the signal pattern and that it is independent of an input model. A weakness is that alongside the main signal of interest, other displacement signals and noisy data can tend to show high phase gradients. Accordingly, these regions experience dense sampling as well, although they are of no significance to the source optimization.

To calculate the data-error variance covariance matrix $\mathbf{C}$ for the data subsampled with the QTA, the pixel covariances need to be propagated to their mean covariance. For each Quadtree square pair we first have to compute a sub covariance matrix, by using an empirically determined variance- and covariance function (Appendix A.2.1). The mean value of such a sub covariance matrix is then assigned as the covariance for the according Quadtree pair (Sudhaus and Jónsson 2009). This process is computationally very expensive, as it requires square-by-square calculation of the full data-error variance covariance-matrix, dependent upon the number of pixels in each track.

5.3.2. Designed pixel subsampling

Designed pixel subsampling (DPS) is a procedure to find the subset of data points that is most sensitive to an input source model. Lohman and Simons (2005) use an initial deformation source model and calculate the data resolution matrix on a coarse grid for the whole radar image. A grid cell is formed by calculating the mean value of all displacement values within the grid cell. If the diagonal of the data resolution matrix of a corresponding grid cell is above a predefined threshold, this cell is sampled finer and the resolution is reevaluated. This is repeated iteratively until the given threshold is reached for all grid cells of the radar image.

Consequently, the data variance-covariance matrix has to be calculated in the same manner as for the QTA by first calculating the sub-covariance matrixes for each grid cell. So for large data sets this calculation is still very expensive and takes a long time for large data sets.

We modify this approach and calculate the model sensitivity of each data point to a given source model. Based on that, as a first step, we select a number of single pixels randomly. In the second step, we evaluate several of such selected data sets, according to their performance with regard to the model parameter covariance, and the condition number. Both of these values are small for an appropriate distribution of subsampled pixels.

The success of subsampling is mostly dependent upon a good choice of input model. The location of regions of high model sensitivity for this input model must align with regions of the observed displacement. The input model can be chosen according to *a priori* information, or can be picked from an ‘educated guess’, by judging the shape of the displacement field or by using the results from a trial source optimization, working with randomly selected data points.

For DPS the number of observations for each data set can be reduced directly to an arbitrary number N_{sub} of pixels. This number has to be still manageable even in extensive optimizations and it has to be large enough to represent the original full displacement signal. For the subsampled data set we evaluate its performance level B , which reflects the source parameter covariance and the condition number (see also Appendix A.4). The smaller these two numbers are, the better the subsampled data can constrain the source model parameters.

To find a subsampled data set $\mathbf{d}_{sub}$ with a good performance level B (lowest value of B) we have to optimize to achieve a good distribution of selected pixels. We search for these well-distributed points by generating a large number K of subsampled data sets $\mathbf{d}_{sub}$, and by sorting them according to their performance B. We then take the best performing data set (lowest B). The possible range of B - values is larger for data sets that were reduced to small numbers (Fig. 5.1). Therefore, when subsampling, a search for good point distributions is particularly important for significant data point reduction.

The data-error variance covariance matrix $\mathbf{C}$ of the subsampled data set is generated by using empirically determined data error variances and covariance functions (Appendix A.2.1). From the seperations between all possible combinations of subsampled pixel pairs, we can compute directly variance and covariance values. The computation of the resulting $N_{sub} \times N_{sub}$ - sized matrix is therefore, very fast and easy.

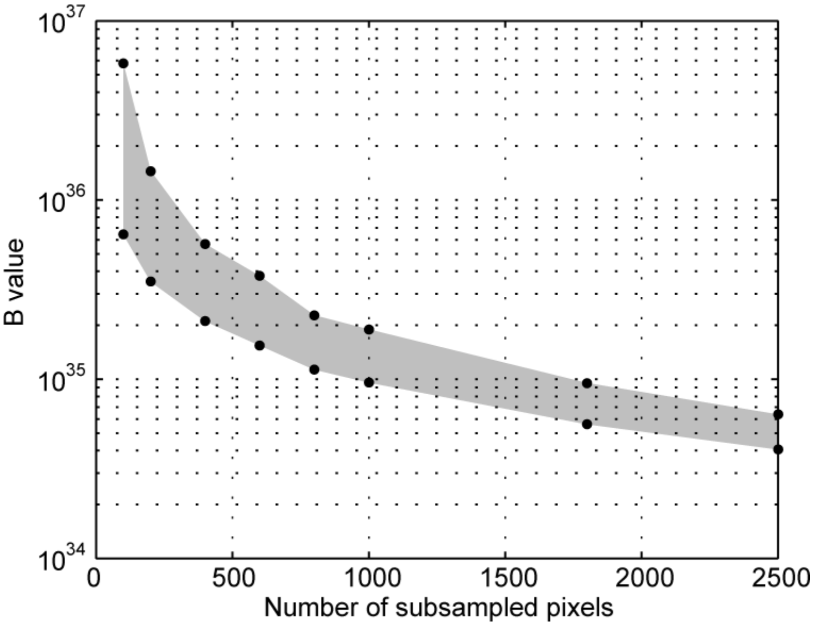

Figure 5.1.: The diagram shows the maximum and minimum value of B for the distribution of subsampled data sets $\mathbf{d}_{sub}$ with $K = 1,000$ versus the number of subsampled pixels N_{sub}.

5.3.3. Subsampling and modeling of synthetic and real data

To assess the performance of the subsampling algorithms we did a synthetic test. We created a synthetic displacement signal by setting the parameters of a certain analytical deformation source. Then we applied the subsampling algorithms (QTA & DPS) to reduce the size of the synthetic displacement data set. By using these reduced data sets separately in 200 repeated source optimizations we then checked whether we could obtain the true source parameters. If the resulting source parameters are distributed close to the original value, the respective subsampling algorithm is able to reduce the original data set without losing information of the full displacement signal.

If both subsampling algorithms performed well in this test, we can compare the modeling results of the established QTA with our new DPS. QTA is widely used and has been proven to perform well; if we can achieve similar good results with DPS it may prove to be a useful alternative way of data subsampling.

After such a validation we applied the whole procedure also to a real displacement data set. By using an InSAR displacement velocity signal acquired over Tendürek volcano we ran a ‘global direct search’ source inversion (Sambridge and Mosegaard 2002) to estimate the parameters of the deformation source. We altered the original displacement data with synthetic noise and repeated the source optimization 200 times. This way the data uncertainties are used to estimate model parameter uncertainties (Sudhaus and Jónsson 2009). Details on the processing of the SAR data to obtain the displacement signal and the source modeling approach are described in (Bathke et al. 2013).

5.4. Results: Subsampling and Source Modeling

5.4.1. Synthetic test

Synthetic displacement signal and the subsampled data sets

We used a closing Okada plane as the target source (Okada 1985) (for parameters see Tab. 5.1) and created synthetic displacement with a heterogeneous distribution of pixels and a maximum displacement velocity of approximately 12 mm/yr for the ascending and the descending track, respectively (Fig. 5.2a,b). Spatially correlated synthetic noise has been added to obscure the displacement signal in a realistic way.

We subsampled the data set with QTA to $\sim$ 200 points. The reduced resulting data set shows dense sampling at the highest gradient of displacement, and sparse sampling where only slight changes in the synthetic displacement signal occur (Fig.5.3a,b). In the very far field of the deformation source there is an almost uniform sampling.

To subsample this data set by using DPS, we used a roughly estimated input Okada model based on the shape of the displacement signal (Okada source parameters see table 5.1). To compare the performance of the subsampling methods the number of points in the subsampled data sets must be almost similar. Consequently, we reduced the original data set to $N_{sub} = 200$ points (Fig.5.3c-d). The resulting data points are located mainly in the regions of high model sensitivity (Fig.5.3e,f). There is no or very sparse sampling in the very far field of the synthetic displacement signal, with low model sensitivity.

Modeling Results

The modeling results for both subsampled data sets are similar (Fig. 5.4). The modeling results show a range of possible source parameters that can explain the observed data

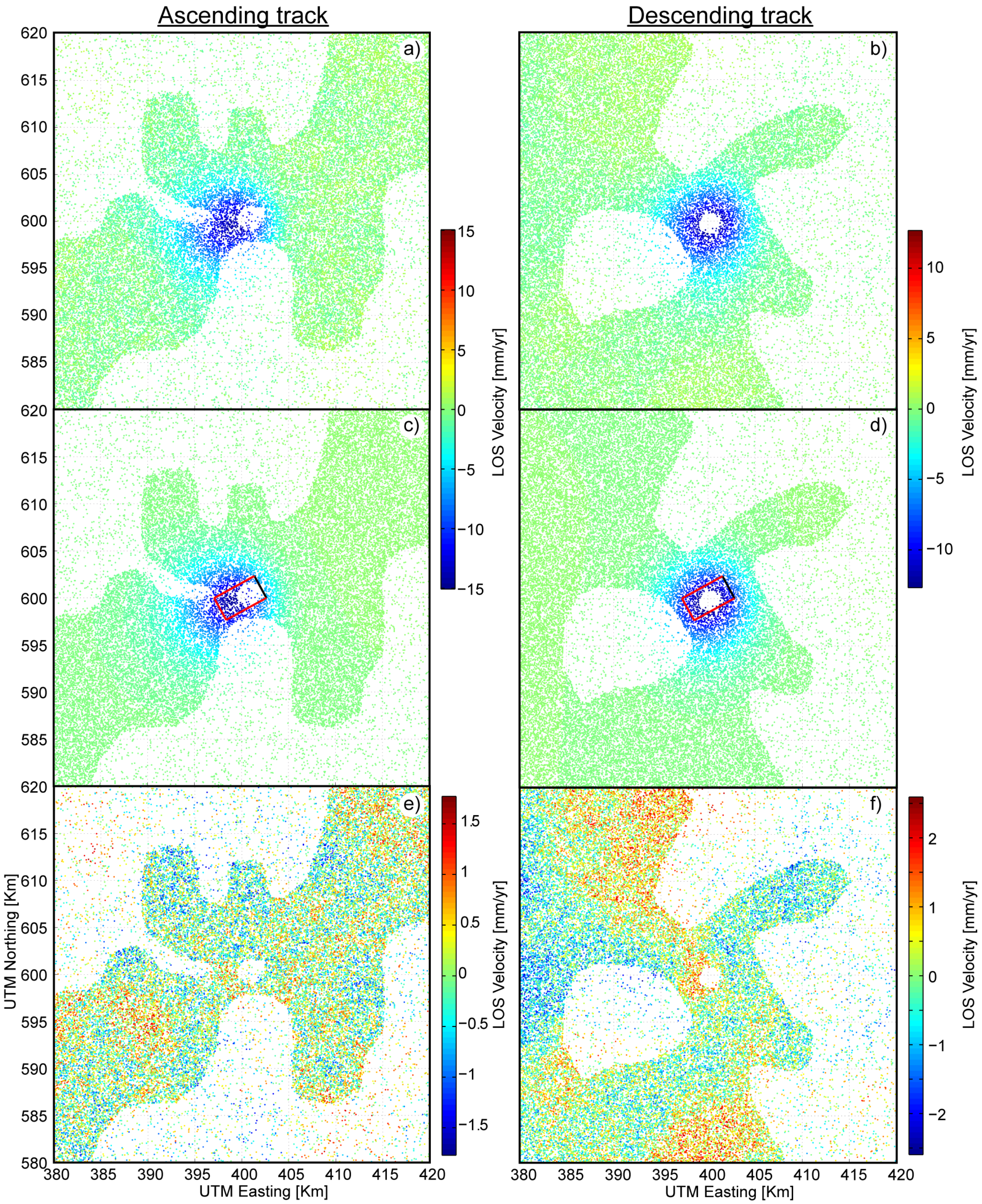

Figure 5.2.: Displacement velocity maps of the synthetic test. (a,b) Synthetic displacement projected in the radar line-of-sight direction of the ascending track and descending track, respectively. The displacement was generated by using Okada target source parameters (Tab. 5.1) and synthetic correlated noise (Tab. A.1). (b,c) Synthetic displacement of the optimum source model in the ascending and descending track. (e,f) The difference between the synthetic target displacement and the displacement of the optimum source model is the residual, in the ascending and the descending tracks. The rectangles in the panels mark the optimum modeled Okada plane, where the black lines indicate the upper edges.

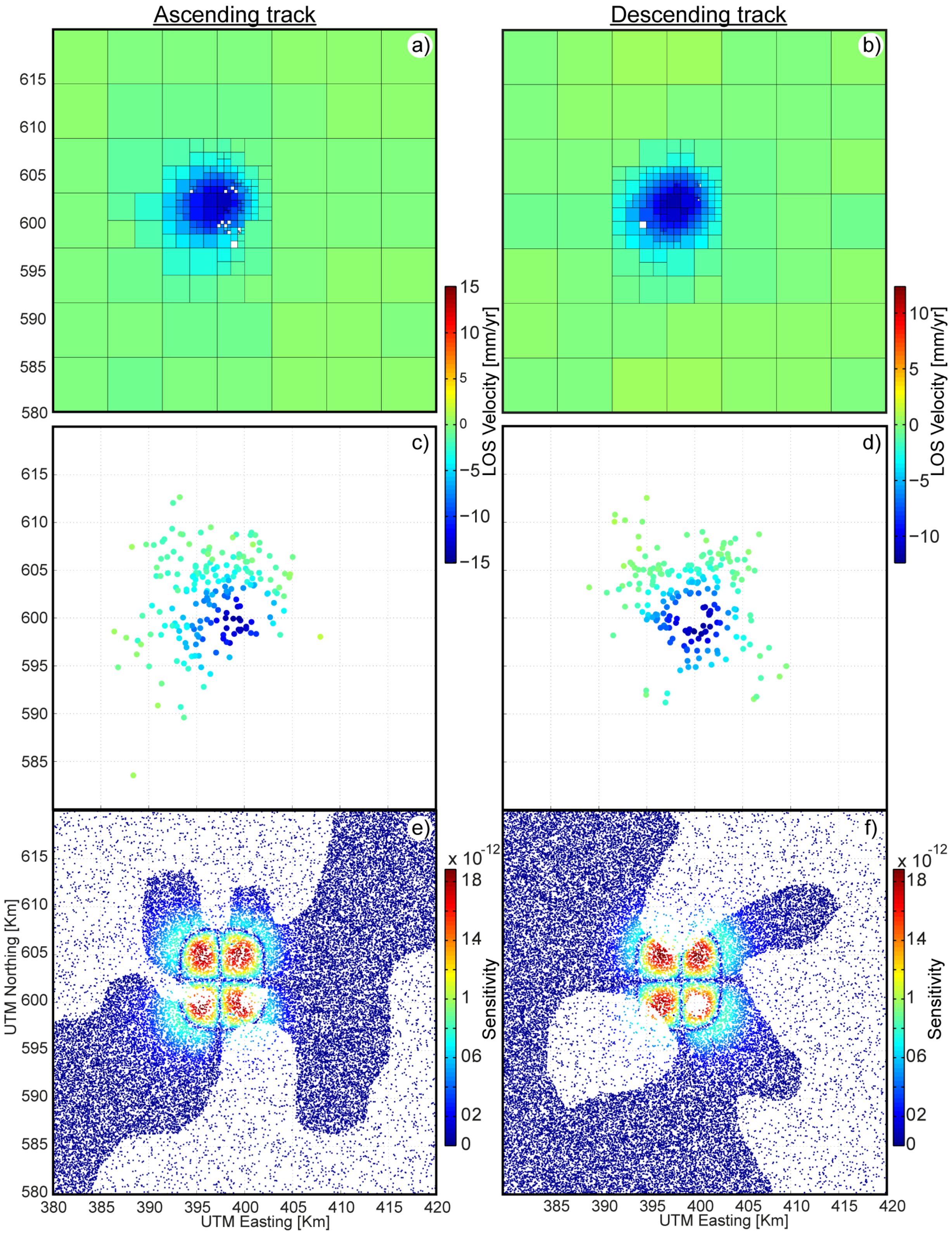

Figure 5.3.: Sensitivity and subsampled synthetic source data sets. (a,b) Subsampled data points by using the Quadtree algorithm (QTA) for the ascending and the descending tracks, and (c,d) by using designed pixel subsampling (DPS) for the ascending and the descending tracks. (e,f) Total sensitivity S of data points to a given input Okada source (Tab. 5.1) in the ascending and descending tracks.

equally well around the true value. Generally, the Okada source target parameters can be successfully retrieved, except for the source depth and source length. For these parameters is the true value of the target source at the margin of the parameter ranges. For the least well-constrained parameters, the target values are still within the 2.5 and 97.5 percentile and all others are more accurately retrieved (Tab. 5.1).

There are parameter ambiguities that cannot be resolved in the modeling results for both subsampled data sets. The correlation between the Okada source parameters shows that with decreasing Okada source opening, the length and width of the contracting Okada plane increases and the depth decreases (Fig. 5.5).

Model residuals, i.e. the difference between target synthetic displacements (Fig. 5.2a,b) and the modeled displacements (Fig. 5.2c,d), lie within the synthetic noise range (Fig. 5.2e,f).

Table 5.1.: Source parameters of the synthetic test: source parameters of the target source, the input model for DPS and the optimum source parameters with their 2.5% and 97.5% percentiles.

SYNTHETIC TEST WITH AN OKADA PLANE									
PARAMETERS		UTM North [km]	UTM East [km]	Depth [km]	Strike [°]	Dip [°]	Length [km]	Width [km]	Opening [m]
TARGET SOURCE		400	600	5.4	150	20	4	6	-0.05
QUADTREE ALGORITHM	Optimum Model	400	600	5.9	146	21	2.0	5.6	-0.11
	Percentile (2.5%,97.5%)	399.7 400.4	599.8 600.3	5.2 6.1	144 164	15 27	0.6 4.3	4.3 6.7	-0.45 -0.04
DESIGNED PIXEL SUB-SAMPLING	Optimum Model	399.9	599.9	5.5	151	18	2.7	5.1	-0.09
	Percentile (2.5%,97.5%)	399.8 400.4	599.8 600.4	5.1 6.2	139 167	17 28	0.5 4.3	0.7 6.4	-0.75 -0.04
INPUT PARAM. DPS		398	602.5	4	90	0	6.5	8	-0.2

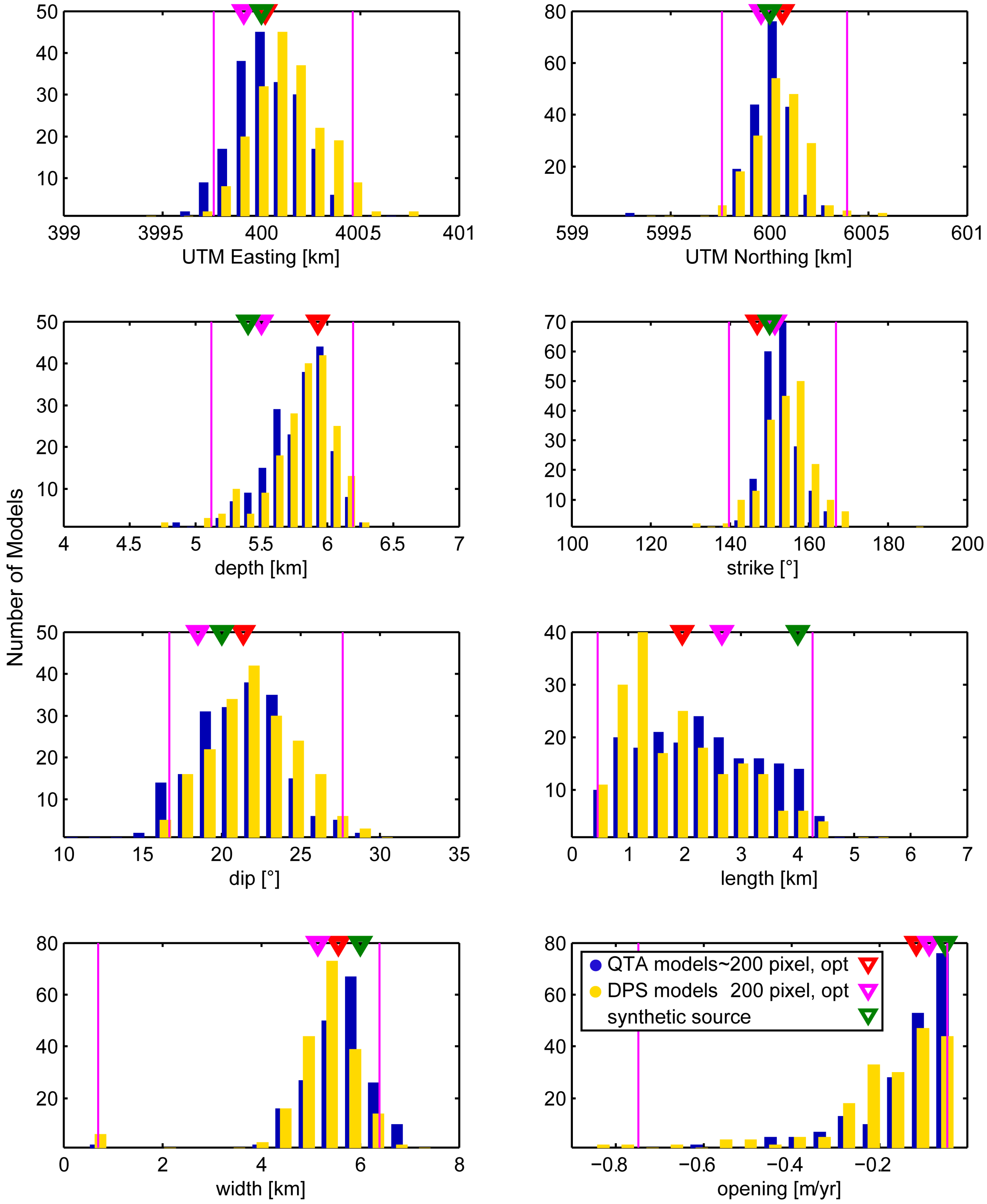

Figure 5.4.: Synthetic test: Histograms of the resulting Okada model parameters for 200 independent modeling runs. The differently subsampled data sets, Quadtree subsampled (QTA) and designed pixel subsampled (DPS), were used to invert for the parameters of the target Okada source. Triangles on top of each diagram give the corresponding optimum values.

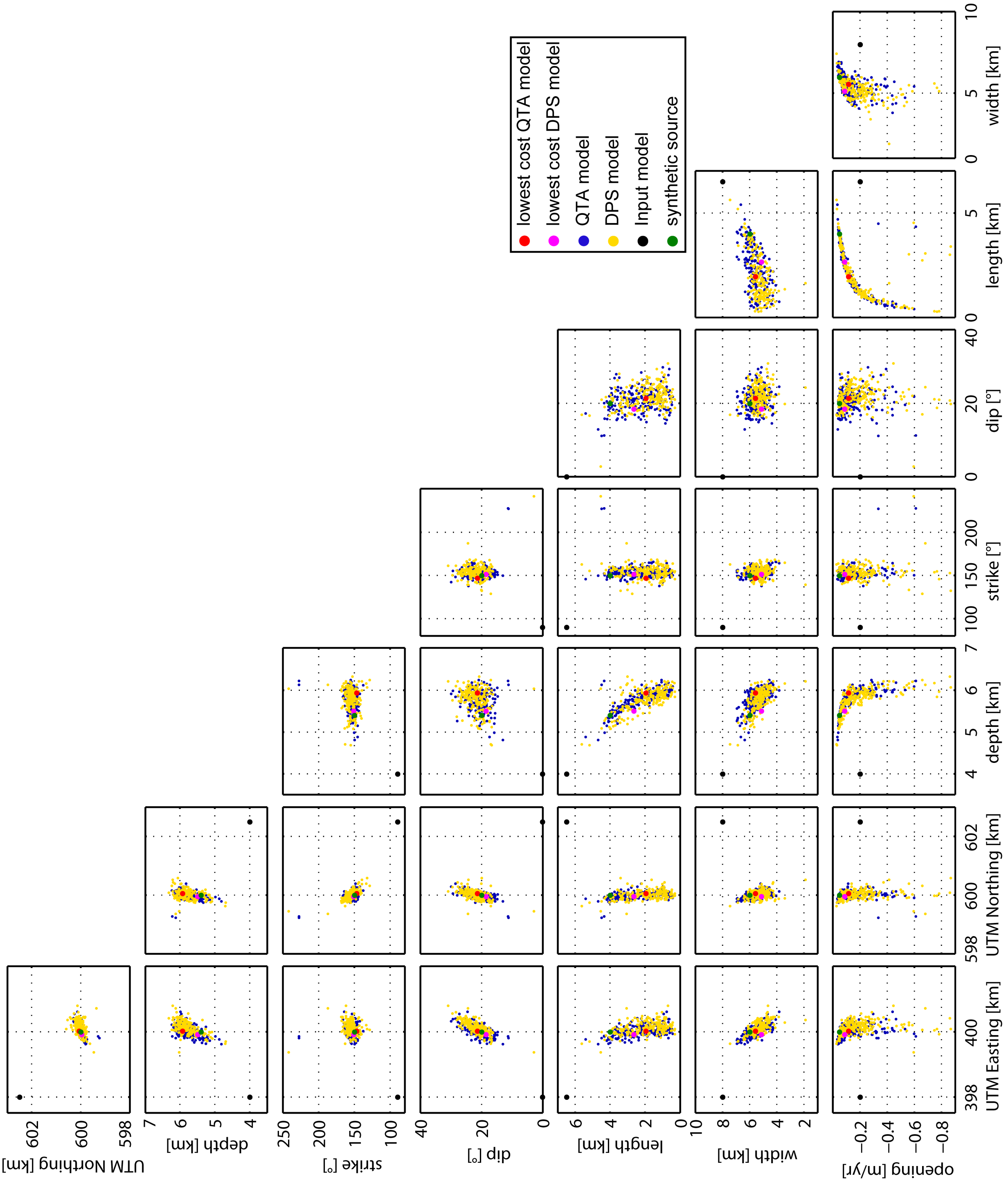

Figure 5.5.: Synthetic test: Okada model parameter correlations of the results of 200 independent modeling runs. The differently subsampled data sets, Quadtree subsampled (QTA) and designed pixel subsampled (DPS), were used to invert for the parameters of the target Okada source.

5.4.2. Application to Tendürek volcano

The InSAR data, the processing to obtain the displacement velocity signal over Tendürek volcano is described in Bathke et al. (2013). The authors obtained the modeling results by using data that has been subsampled with the QTA. To test the influence of different subsampling methods on the modeling results, we used the same displacement data and repeated the subsampling and modeling with DPS. Based on the shape of the displacement signal at Tendürek, we roughly estimated the parameters of an Okada input model (Tab. 5.2).

To make the comparison of the QTA with DPS, the number of points must have been reduced in such a way that it was comparable with the results of the QTA. We adjusted the DPS parameter N_{sub} so that we finally ended up with 2,500 pixels in the displacement velocity data of the ascending and the descending tracks, respectively.

Table 5.2.: Source parameters of the Okada source taken as input model for DPS.

OKADA SOURCE INPUT PARAMETERS							
UTM East [km]	UTM North [km]	Depth [km]	Strike [°]	Dip [°]	Length [km]	Width [km]	Opening [m]
405	4357	5	90	10	7	10	-0.3

Subsampled data sets

The resulting Quadtree square distribution (Fig. 5.6a/b) and the according centroid coordinates of all pixels within a Quadtree square (Fig. 5.6c,d), show that there is dense sampling at the summit and the flanks of the volcano, as well as in the far field of more than 20 km radial distance. Pixels at a summit distance of about 10 km are very sparsely sampled, because they hardly show any gradient in the displacement. Dense sampling occurs in the very far field, because of phase fluctuations that are unrelated to the source beneath Tendürek and are, therefore irrelevant to our study.

For the subsampling with DPS in this study we use $K = 1,000$ (repetition of sampling) for subsets of 2,500 points. Pixels in the very far field, with more than 10 km radial distance to the volcano summit, are very sparsely sampled, due to their low sensitivity according to the deformation in the vicinity of the volcano edifice (Fig. 5.7a,b). As a result, the pixels are definitely well distributed over the area and able to capture the deformation signal (Fig. 5.7c,d). Through DPS the pixel density has been more decreased at the foot and the flanks of the volcano than at the volcano summit. Therefore, the pixels there will have a high influence in the source modeling. This supports the search algorithm to find the global optimum solution.

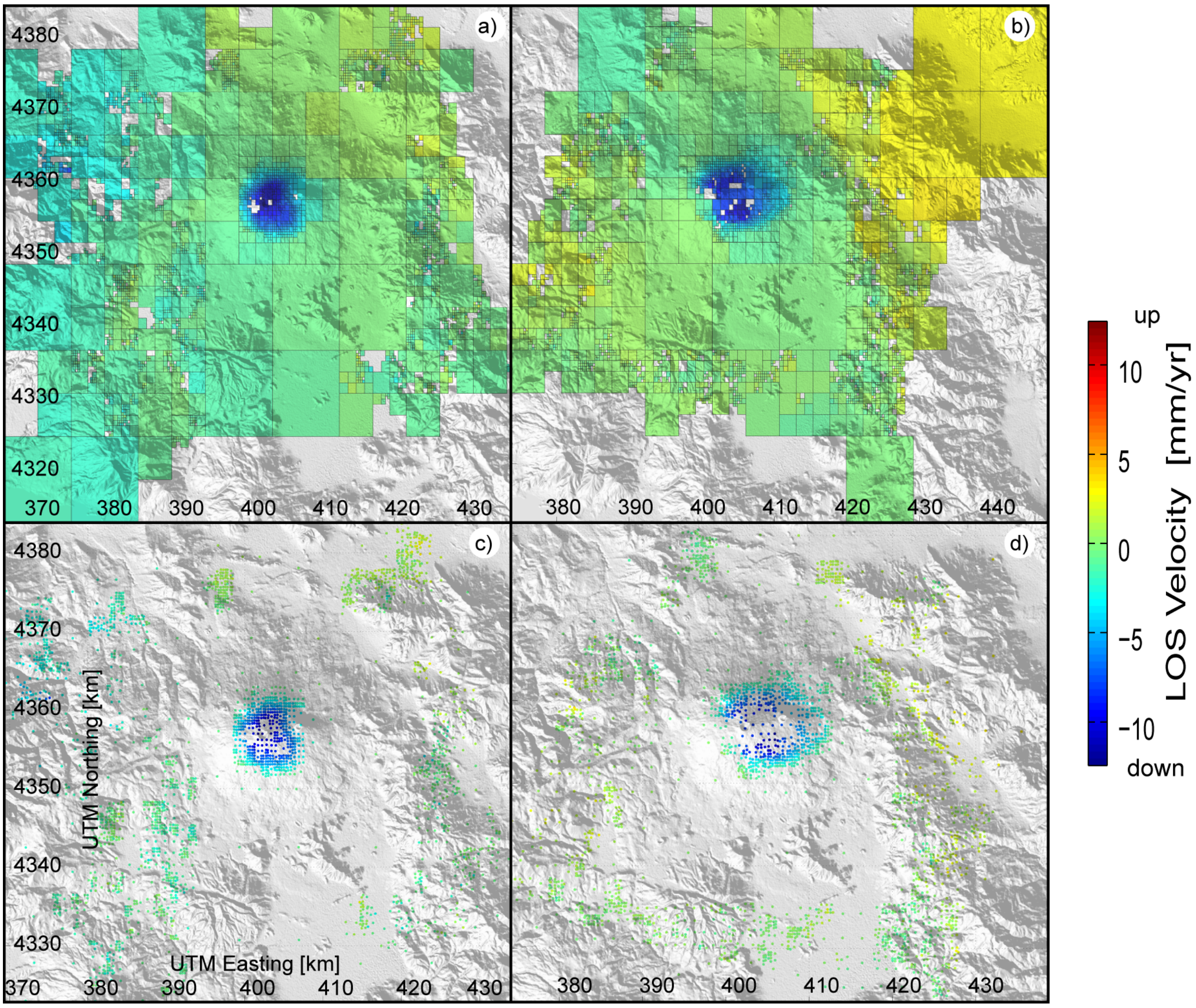

Figure 5.6.: Application to Tendürek: Data sets subsampled by using the Quadtree algorithm (QTA): (a,b): Quadtree squares; (c,d): focal points of the pixels in one Quadtree square; for the ascending and the descending tracks, respectively.

Modeling Results

In the following section we compare the modeling results obtained from 200 optimizations with QTA subsampled data, with the results obtained from 200 optimizations with DPS data.

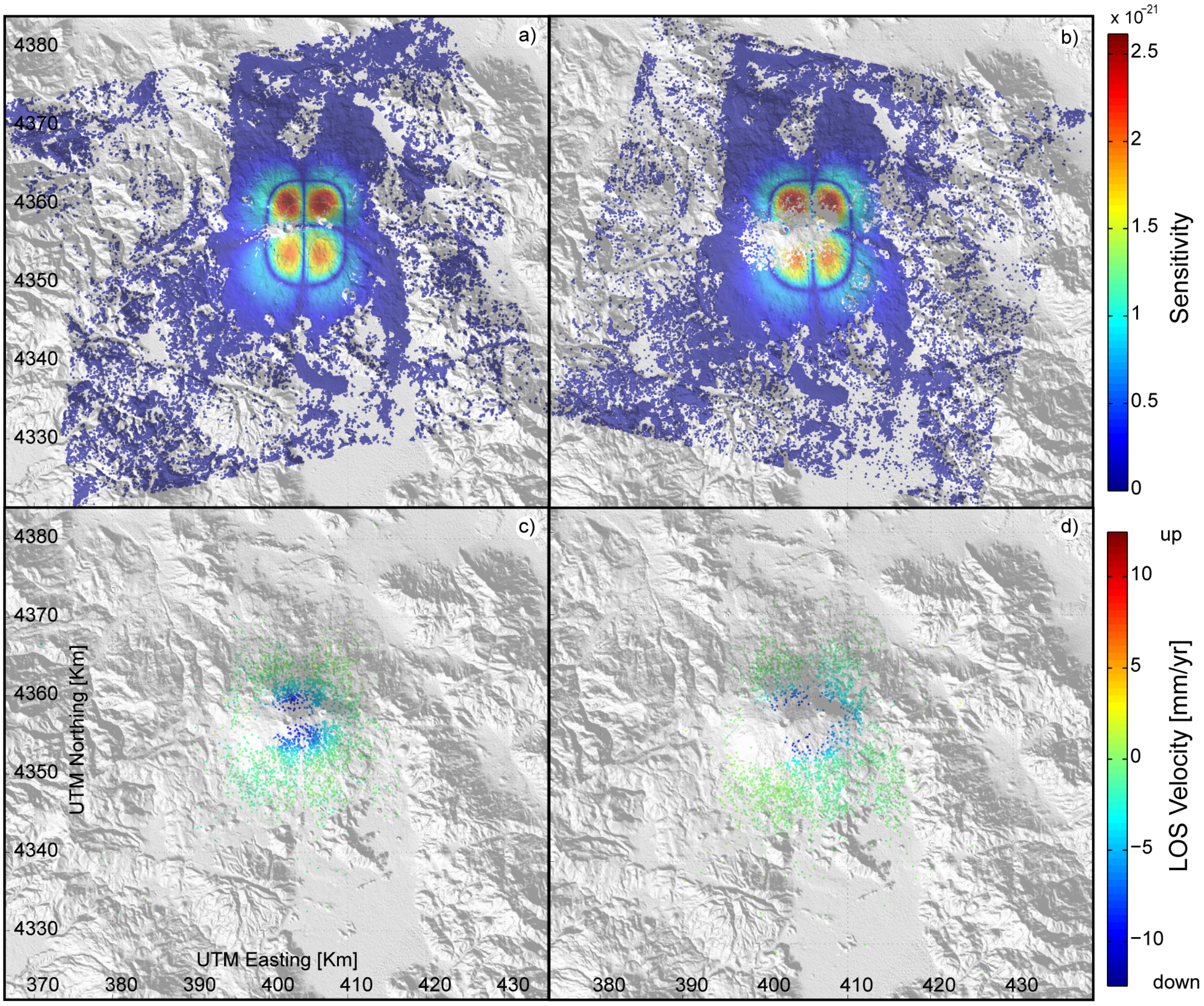

Figure 5.7.: Application to Tendürek: Data sets subsampled by using the designed pixel subsampling (DPS): (a,b): total sensitivity S of points to a given Okada source (Tab. 5.2); (c,d): final subsampled data points by using DPS for the ascending and the descending track, respectively.

Okada source The resulting Okada model parameters are in general similarly distributed for both data sets (Fig. 5.8, Tab. 5.3). The observed displacement velocity can be explained well through a range of source models, rather than just through one precise optimum solution.

The central location of the Okada plane (403.5 km UTM easting, 4356.9 km UTM northing), however, and the closing of 1.7 cm/yr, seem well constrained. For these parameters the histograms show pronounced peaks and narrow confidence intervals (Fig. 5.8). The depth and strike of the model plane are less well constrained, since here we find bi-modal parameter distributions for both subsampling methods. The remaining parameter solutions seem to be well constrained for both individual subsampling methods. The model parameter values of depth and dip differ for the QTA and DPS, however. Since the histograms of modeled depth overlap, within their 95% percentile intervals, the difference is not significant (Tab. 5.3). In contrast, the dip value differs by $10° - 15°$ between the two distributions without overlap.

Two-dimensional correlations of the source parameters are provided in Fig. 5.9. They show that solutions change significantly, when the strike changes from northwest to northeast. There is a trade-off between the origin of the Okada plane and other parameters; depth increases while the length shortens, and the amount of closing increases. Furthermore, the major part of our solutions show a clear correlation between dip and depth.

Influence of the number of subsampled pixels Data subsampling increases the computation speed of deformation source modeling, but for large reductions in data points there is a trade-off between the number of data points and their ability to constrain the model. For our problem we tested: “How many data points are needed to obtain a stable model result?” We subsampled the original data sets to different numbers of points (200, 400, 600 and 800) and repeated the Okada source modeling for each of these sub-sets independently. The results show that for 800 observations the parameter distributions are very similar to the results based on 2,500 points (Fig. 5.8). For decreasing numbers of subsampled pixels (600, 400 or 200), we found a degradation of the model parameter resolution, most pronounced for the model dip and length. The lower the number of pixels in the subsampled data sets, the less pronounced were the peaks in the histograms whilst the range of the different model parameters remained relatively stable (Tab. 5.3).

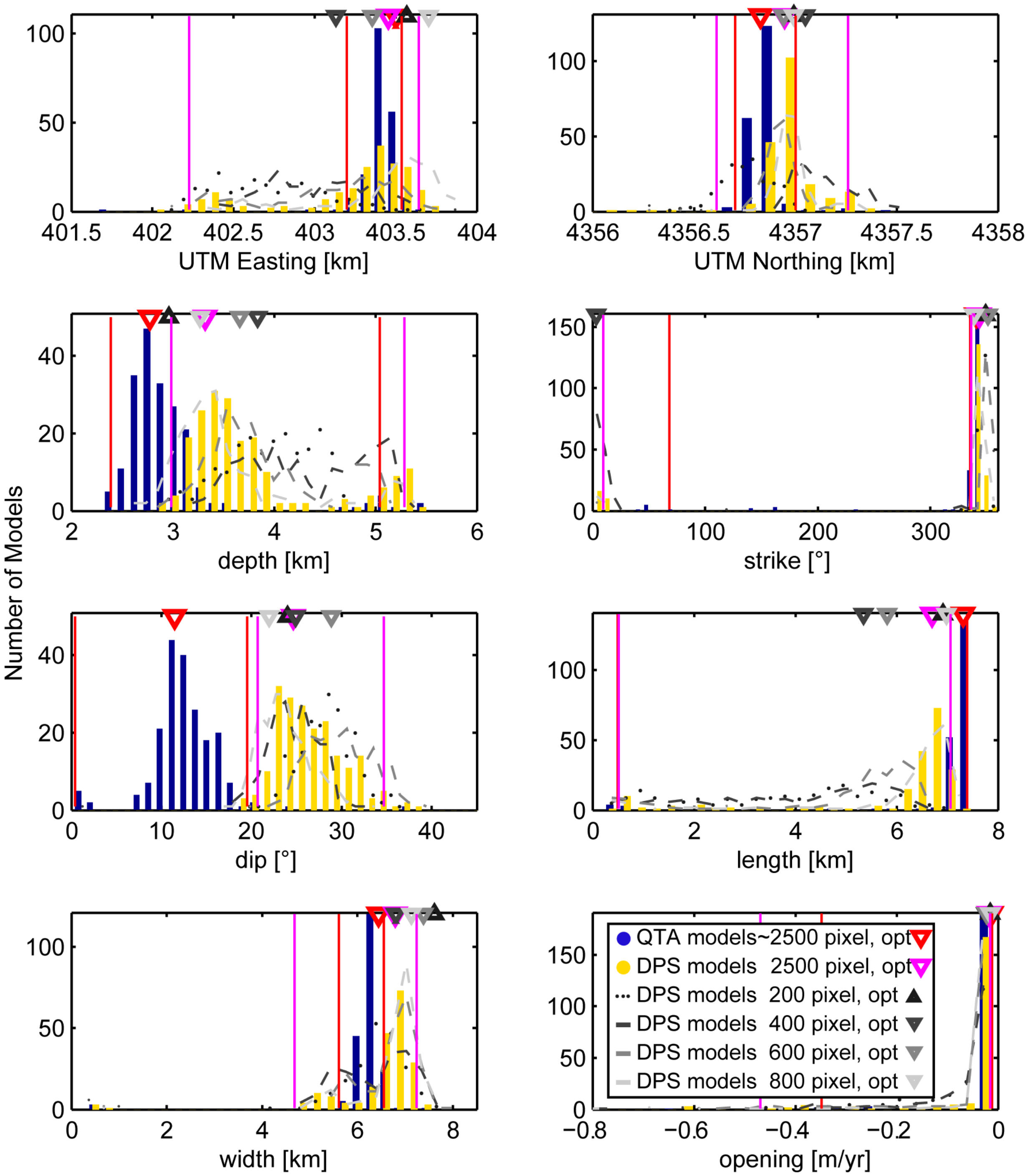

Figure 5.8.: Application to Tendürek: Histograms of the resulting Okada model parameters for 200 independent modeling runs. The differently subsampled data sets, Quadtree subsampled (QTA), designed pixel subsampled (DPS) and smaller subsampled numbers for DPS were used to invert for the parameters of an Okada source. Triangles give the corresponding optimum values and the magenta vertical lines mark the upper and lower 2.5% percentile of the 2,500 point DPS results.

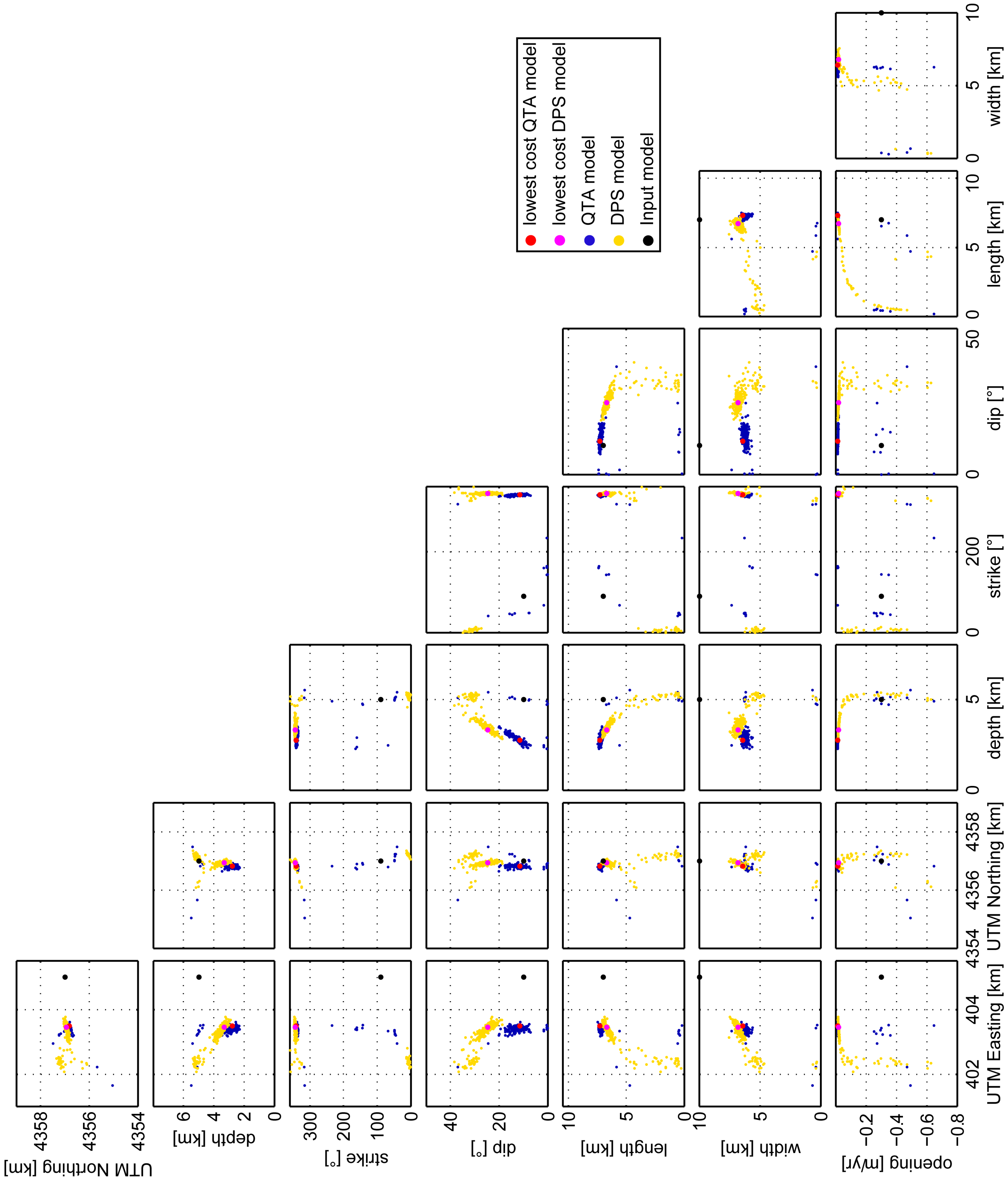

Figure 5.9.: Synthetic test: Okada model parameter correlations of the results of 200 independent modeling runs for data sets with ∼ 2500 pixels.

5.5. Discussion

The herein introduced Designed Pixel Subsampling (DPS) is an alternative subsampling approach that is modified from Lohman and Simons (2005). We compared its performance with the established Quadtree Algorithm (QTA) through deformation source modeling, by using a synthetic test data set with known source parameters.

We also applied the two subsampling algorithms to a displacement velocity data set over Tendürek volcano and modeled the deformation source by using an Okada source model. As we want to focus in the following section on the performance of the subsampling algorithms, we refer to Bathke et al. (2013) for the discussion of modeling assumptions and the implications of the resulting modeled source parameters at Tendürek volcano.

5.5.1. Synthetic test

With the synthetic test we wanted to check following issues: Firstly, does the subsampled data set allow to find the target source parameters through deformation source modeling? Secondly, how do the modeled source parameters change by using a different subsampling algorithm for data reduction? Thirdly, how do the input model parameters of an analytical source, e.g. Mogi (Mogi 1958), Okada (Okada 1985) or Yang (Yang et al. 1988), influence the modeling results?

The modeling results for the synthetic displacement data set (Tab. 5.1) show that the true solution for each parameter is usually flanked by a range of solutions, which are also acceptable in terms of data misfit. These parameter ranges can be attributed to the amplitude of the spatially correlated synthetic noise signal. It contributes about 10-15% of the whole synthetic displacement signal and increases the solution space for possible Okada source parameters. Independent from the subsampling algorithm, these ambiguities between the source parameters of the modeling results cannot be resolved. Nevertheless the target source parameters were obtained within the 95 % percentile.

For both subsampling methods, the modeling results and the width of the parameter ranges, are very similar (Fig. 5.4). Thus both subsampling algorithms perform equally well and seem to have little influence on the modeling results.

The input model parameters for DPS are very different compared to the parameters of the target source and the modeling results are comparable between both subsampling methods. Therefore, in this case, the input model parameters seem to have little influence on the final source optimization.

5.5.2. Application to Tendürek volcano

Real data always has several sources of correlated and uncorrelated noise (Hanssen 2001). Nowadays it is still nearly impossible to correct the data for all of these sources of error, which usually matter in the deformation source modeling procedure. Other sources of deformation contributing to the observed displacement influence the modeling of the primary deformation source. Thus the subsampling of data points, which show displacement of either sources increase the ambiguity of the final source parameters in addition to the noise components. Fukushima et al. (2005) showed that the optimization results vary slightly for data subsampled with various methods.

Akin we see differences in our modeling results for the Tendürek deformation source, for the different subsampling algorithms. The distributed dip angle solutions are not overlapping between both subsampling methods. We assume that the secondary deformation signal within the data, the Tendürek ring faults (Bathke et al. 2013), are represented differently in each subsampled dataset. The QTA averages pixels within each square and therefore the rather sharp signal along the ring fractures, will be suppressed. On the contrary the DPS does not alter the original data values and the displacement signal corresponding to the ring-faults is not suppressed. This may be one explanation for the large differences in the modeling results for the fault dip.

5.5.3. Features: QTA versus DPS

In this section we aim to illustrate advantages and disadvantages of both subsampling algorithms.

User influence

Almost every processing step in the processing chain of producing surface displacement data until the modeling of the observed signal needs user interaction. So does the data subsampling and weighting procedures. Therefore, the modeling results will be to some extent influenced as well by that important step.

The DPS is a model-driven method whereas the QTA is data-driven; both appeal to reduce the number of points in a highly redundant data set. When using DPS, an appropriate input model needs to be chosen, whereas QTA parameters need to be adjusted, to successfully retrieve the displacement signal with a reasonable number of points. The main QTA parameter is the threshold on the gradient of displacement that defines, if a grid cell is divided into several smaller cells. Therefore, the resulting number of subsampled points is indirectly produced. In the DPS the best distribution of available pixels around a defined deformation source will be given based on the desired number of subsampled pixels. Thus, the resulting number of subsampled points can be directly adjusted.

The settings of both subsampling algorithms are to some extent subjective to the applicant, who either chooses an input model for DPS or tunes the QTA.

Interferograms and Time Series

In geocoded interferograms the data points are mostly homogeneous on a semi-regular grid. Where in a time series (e.g. the SBAS or PSI methods) the data points are distributed heterogenously. These two settings influence the way of subsampling.

The QTA works better for 2-pass interferograms, but is not easily applied to the heterogeneously distributed points of a time series.

By using DPS, data sets with spatially heterogeneously distributed data points can be subsampled in an efficient way. The pixels that are more relevant for the deformation source model are selected. Pixels, once identified as important in a single interferogram of the time series, will also be crucial in all other remaining interferograms, given that the source process does not change essentially. Hence a particular pixel selection can be applied to all the interferograms of a time series. This may simplify the continuous monitoring of volcanoes and the corresponding modeling of sources, as the subsampling does not need to be repeated for each single interferogram. This is required if the QTA is applied for data subsampling.

On the other hand, these advantages lessen if DPS is applied on the pixels of a 2-pass interferogram, instead of a displacement time series. In interferograms, noisy pixels will be selected as well as coherent phase pixels that influence the data quality and eventually the optimization results, if not removed previously. In a properly processed time series there is usually a lower noise level (Ferretti et al. 2007), and thereof less risk to select outliers.

Data errors and error propagation

Interferometric displacement data has several sources of error that are sometimes hardly removable (Ferretti et al. 2007, Hooper 2008). Sequentially, the displacement signal that is associated with a certain deformation source at depth is altered by these errors. That in turn leads to higher uncertainties and ambiguities in the modeling of the deformation sources. Hence, the best way is to estimate these uncertainties and express them in terms of a range of modeled deformation source parameters (Sudhaus and Jónsson 2009).

The QTA may produce a high density of points in the presence of small scale noise or phase unwrapping errors, because these show high phase gradients. Such extra points decrease the efficiency of the optimization process and may cause bias if not manually removed. The DPS works independent from the displacement signal itself, therefore noisy data will not increase the amount of subsampled points.

Apart from the subsampling itself, propagation of the data error covariances to the subsampled data set after DPS is less complicated than after applying the QTA, since no averaging of pixels is involved. Covariance values can be picked directly from the covariance function, and the whole variance-covariance matrix is created very quickly. In contrast to that, the covariance of a Quadtree square is calculated from the covariances of all contributing pixels, which is often time.

In this work it took a few seconds to create the variance-covariance matrix after DPS, and 3 days when subsampling using the QTA on a DELL workstation with 8 processors.

To conclude, DPS performs as well as QTA does, because the optimum model and the range of all the model solutions for both subsampling methods differ very little. The source parameter ranges are slight, but insignificant, wider for the DPS than for the QTA (Tab. 5.3). Nevertheless, in this study on time series data the DPS shows several advantages and we consider it to be a proper alternative method for subsampling heterogeneously distributed InSAR data.

5.6. Conclusions

We introduce an alternative InSAR data reduction method that is modified from the R-based subsampling from Lohman and Simons (2005). This method may be applied to subsample interferograms and InSAR time series of displacement for deformation source modeling.

Single important data points in a heterogeneously distributed data set are identified with respect to a given input deformation source model. Consequently, the subsampling is independent of the measured displacement signal and does not need to be repeated for each single displacement data set. This holds under the assumption that the source of deformation has not changed position over the time of observation significantly.

Data errors can be propagated to model uncertainties much easier and faster with the new method compared to the Quadtree algorithm, as the variance-covariance matrix can be calculated within seconds.

This supports upcoming and already existing monitoring of the displacement field of volcanoes worldwide and therefore, the investigation of their plumbing systems. The available high resolution TSX satellite data and the data of future satellite missions have and will have even denser measurements at the earth's surface. For deformation source modeling, however, only a fraction of the available data points is needed and data reduction will be of increasing importance.

Table 5.3.: Source parameters of the optimum source models and percentile intervals for the modeling results with the subsampled data sets using both methods: the designed pixel subsampling (DPS) and the quadtree algorithm (QTA).

APPLICATION TO TENDÜREK: OKADA SOURCE MODEL RESULTS

Source parameters		UTM East [km]	UTM North [km]	Depth [km]	Strike [°]	Dip [°]	Length [km]	Width [km]	Opening [cm/yr]
QTA $\sim$ 2500 pts	Optimum Model	403.5	4356.9	3.3	343	25	6.7	6.8	-1.7
	Percentile	402.2	4356.6	3	336	21	0.5	4.7	-46.7
	(2.5%, 97.5%)	403.6	4357.2	5.3	10	35	7.0	7.2	-1.5
DPS 2500 pts	Optimum Model	403.5	4356.8	2.7	341	11	7.3	6.4	-1.4
	Percentile	403.2	4356.7	2.3	335	1	0.5	5.6	-34.9
	(2.5%, 97.5%)	403.5	4357.0	5.0	68	20	7.4	6.6	-1.4
DPS 800 pts	Optimum Model	403.7	4357.0	3.3	339	22	7.0	7.1	-1.6
	Percentile	402.5	4356.8	2.8	338	19	0.4	5.1	-60.2
	(2.5%, 97.5%)	403.8	4357.3	5.3	8	31	7.2	7.5	-1.3
DPS 600 pts	Optimum Model	403.4	4356.9	3.6	351	28	5.8	7.4	-2.2
	Percentile	402.3	4356.8	3.0	346	23	0.4	5.3	-46
	(2.5%, 97.5%)	403.6	4357.1	5.0	2	37	6.4	7.4	-1.7
DPS 400 pts	Optimum Model	403.1	4357.0	3.8	3.2	25	5.3	6.8	-2.3
	Percentile	402.5	4356.4	3.3	327	19	0.5	5.3	-62
	(2.5%, 97.5%)	403.6	4357.4	5.2	17.3	30	6.3	7.4	-1.7
DPS 200 pts	Optimum Model	403.6	4357.0	3.0	349	24	6.9	7.6	-1.5
	Percentile	402.2	4356.5	3.0	339	22	0.5	5.2	-37
	(2.5%, 97.5%)	403.4	4357.0	4.6	352	34	6.5	7.4	-0.9

6. General Discussion and Outlook

With this work I would like to contribute to the understanding of source processes at two previously barely studied volcanoes, which differ in their genesis, structure and composition.

The first case study about Llaima, a stratovolcano in Chile, showed that the pre- and post-eruptive sources are located at shallow and high depths, respectively. A plausible explanation to this would be that the magma has ascended prior to the eruption into the shallow reservoir. Independent petrological studies have confirmed the setup of magma reservoirs at Llaima (Bouvet de Maisonneuve et al. 2012b,a). If continuously monitored a longer time-span, other volcanoes that are located in a similar tectonic regime might show complementary complex source interactions, instead of the assumption of just one single magma chamber (Pritchard and Simons 2004, Fournier et al. 2010).

In the second case study at Tendürek volcano, I have found an even more complex interaction of deformation sources. Elliptic ring-faults, which exist around the volcano, have been reactivated during a slow but continuous subsidence of the volcano edifice, caused by a contracting subsurface source. Based on this observation, the widespread concept of a fast catastrophic caldera genesis might be supplemented with the idea of calderas being slowly forming over several thousands of years. Only few cases of caldera formation with active ring-faulting have been witnessed so far. Therefore, the process of caldera formation is mostly based either on indirect interpretation of existing geologic structures or on numerical and analog modeling. Hence, Tendürek volcano poses an ideal target for a further investigation of the ring-fault (re)-activation process during a phase of subsidence.

All these processes of volcano deformation will be better understood, if an increasing number of volcanoes are to be monitored by complementary station networks (e.g. seismic), additionally to remote sensing data. A detailed analysis of the petrology of the eruptive products of volcanoes has been approved to be very useful to determine the depth of magma chambers, the magma origin and besides, it allows investigating the eruptions of the past.

Deformation processes at volcanoes are on the one hand long-lasting and on the other hand very fast variable sometimes. Consequently, an interdisciplinary and continuous monitoring of volcanoes is the most important to enable a coverage either of short periodic as well as long-periodic deformation signals.

One of such tools to measure displacements at the Earth's surface is InSAR that has been proven to be reliable and effective. Due to the upcoming new generation of high resolution SAR satellites (Sentinel), which have a global coverage and frequent passes of just few days, the InSAR method could be used for the development of a volcano rapid response system. A similar system based on seismic data has been operating since decades, wherein earth quake magnitude and epicenter determination are automatically and routinely done. Nevertheless there are still many problems that have to be resolved in such an InSAR-based system. The short wavelength radar signal of the high resolution satellites will be strongly affected by the atmospheric water vapor and suffers from decorrelation, if the displacements are high. Another major problem nowadays, is that the calculation of a displacement time-series requires a reprocessing of the whole data set with each radar acquisition, which is added. Therefore, algorithms that obviate or solve these problems will be needed.

A fast, reliable and automatic modeling for initial deformation source parameter estimation will require a reduction of the large amount of data. The technical advancements of this work, the subsampling algorithm and the model based unwrapping/the modeling of wrapped phase data, are tools that could be a valuable part of such a rapid response system.

A catalog of events at volcanoes, similar to the earthquake catalogs, could be produced and also statistically investigated with such a system. This would improve our understanding of the deformation processes acting at volcanoes step by step and thus result in more reliable eruption forecast.

A. Appendix

A.1. Llaima volcano

InSAR data and source modeling results at Llaima volcano. a: Observed wrapped phase data with coherence threshold of 0.24. b: Synthetic phase data from the approximate deformation model (ADM). c: Observed wrapped phase data with coherence threshold of 0.17 from the same SAR scenes as part a. d: Phase residual between observed wrapped phase data with low coherence (c) and synthetic phase data from the approximate (b). e: Line of sight deformation (LOS) of the complete unwrapped data set (CUD). f: Synthetic LOS deformation for the optimum deformation model (ODM) for the CUD (e). g: LOS deformation residual between the CUD (e) and the synthetic LOS deformation for the ODM (f).

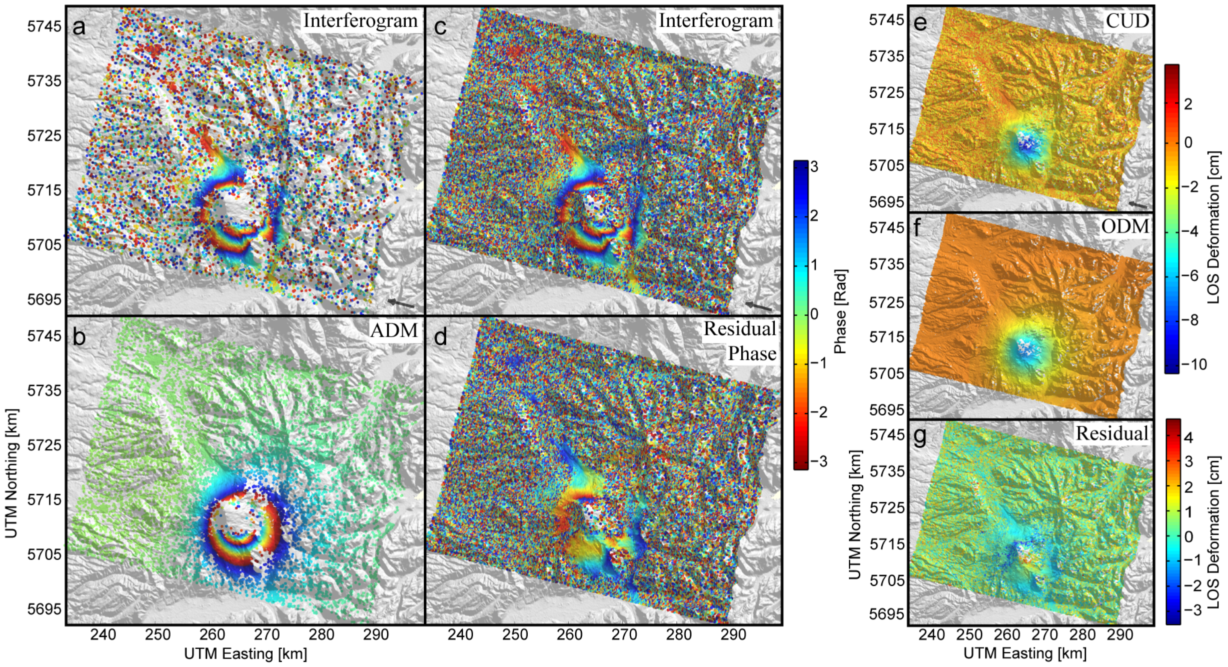

Figure A.1.: Interferogram of 25. November 2003 and 03. April 2007. Description see text above.

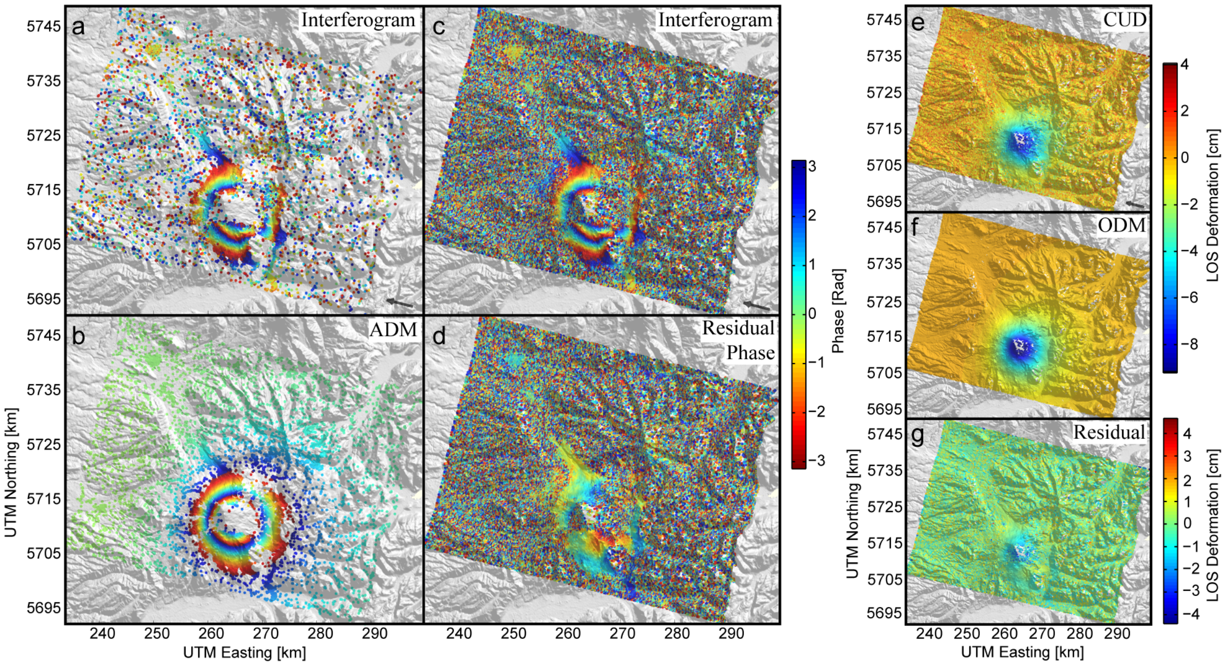

Figure A.2.: Interferogram of 09. March 2004 and 03. April 2007. Description see text above.

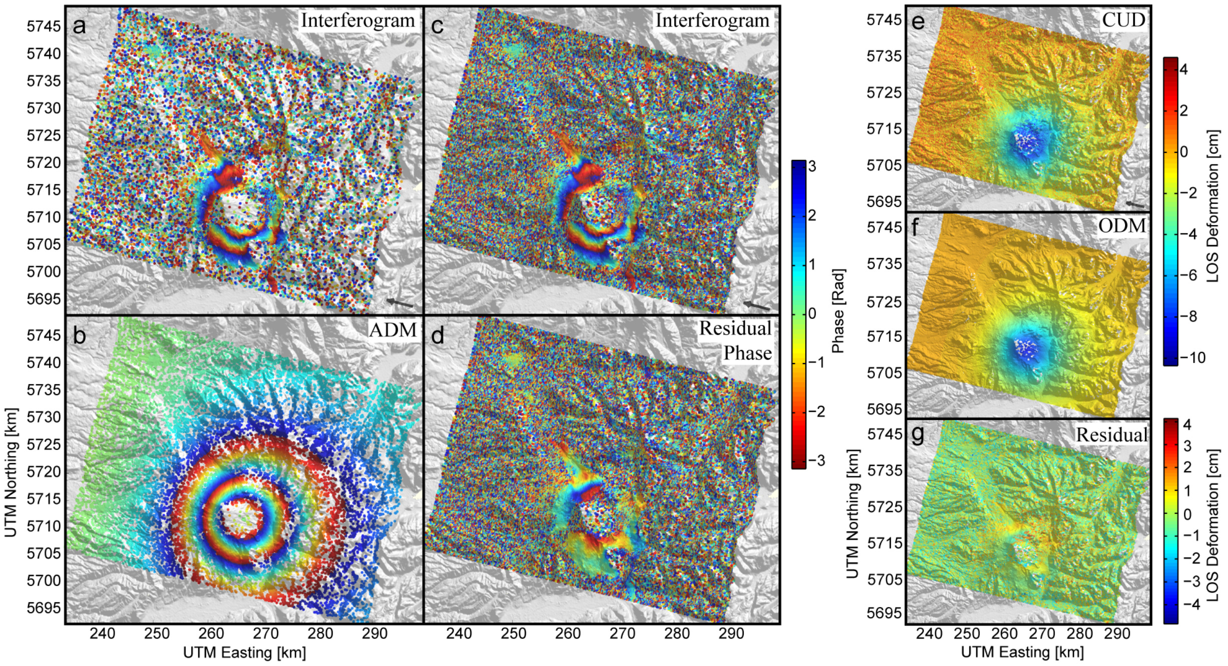

Figure A.3.: Interferogram of 09. March 2004 and 08. May 2007. Description see text above.

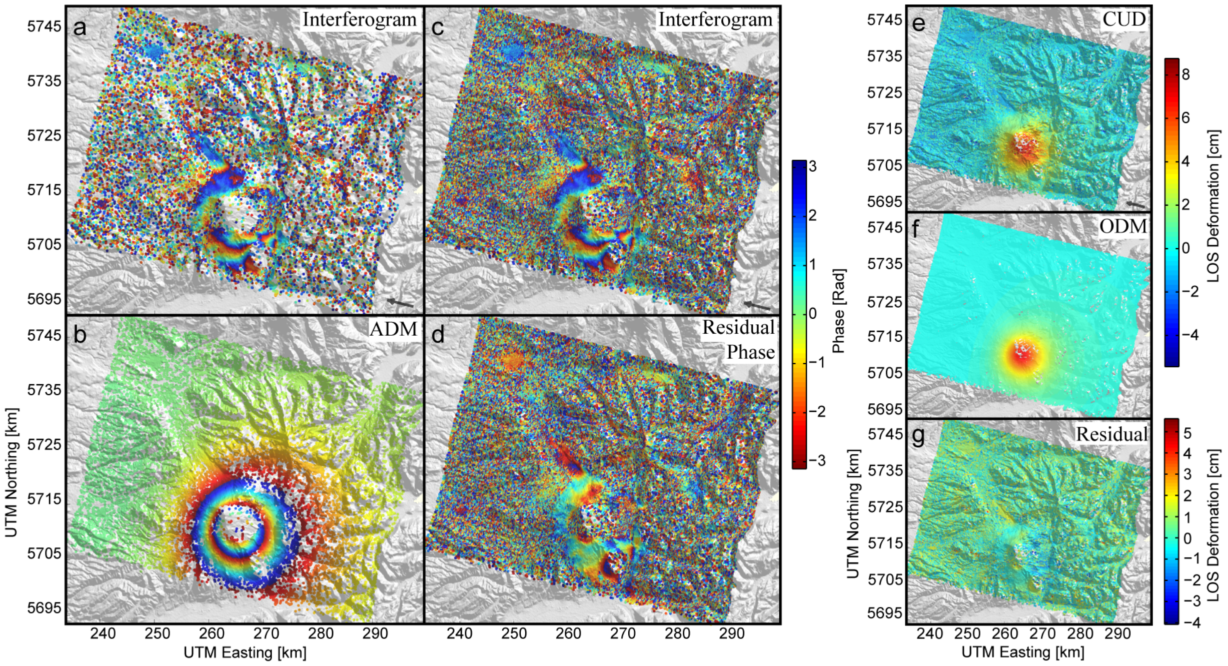

Figure A.4.: Interferogram of 08. May 2007 and 08. January 2008. Description see text above.

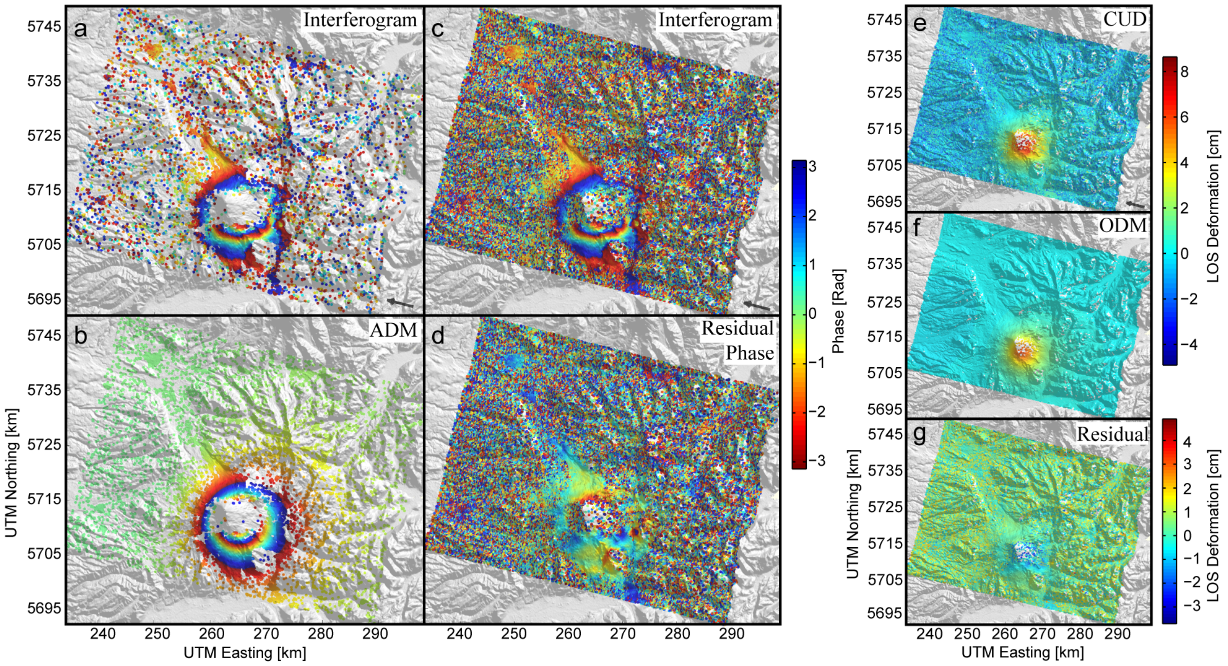

Figure A.5.: Interferogram of 03. April 2007 and 18. November 2008. Description see text above.

A.2. Tendürek volcano

A.2.1. Data error estimation

The empirical data error estimation was done in the far field of the volcano summit, where no systematic displacement is observed. We assumed that the data error is stationary (i.e. the error characteristics measured in the far field are identical to those in the deformed areas) and that we can approximate the data error characteristics with random functions. For these random functions, we here used the functional form $g(r) = a \cdot e^{-\frac{r}{p}} \cdot cos(2\pi f \cdot r)$, where a is the amplitude coefficient of the function, p is the degree of functional decay, f is the frequency of the functional oscillation and r is the distance between the points of one co-variogram sample. The p and f parameters are measures of spatially correlated atmospheric noise. As the noise structure of the descending track has a strong correlated component, these values are high (Tab. A.1). No cosine term is necessary to fit the co-variogram of the ascending track data. Here, and are low, whereas the covariance decays very fast. Thus the data error in the ascending track consists mainly of spatially uncorrelated phase decorrelation that is expressed with the variance value.

Table A.1.: Covariance function parameters of the descending and ascending tracks using the functional form $g(r) = a \cdot e^{-\frac{r}{p}} \cdot cos(2\pi f \cdot r)$.

Covariance Function Parameters					
	Variance [m^2]	Coefficient a [m^2]	Frequency f [1/km]	Power p [km]	Synthetic noise amplitude [mm/yr]
Descending track	$6.0078e-7$	$9.0815e-8$	0.0164	9.1507	-/+1.4
Ascending track	$8.3786e-7$	$4.7318e-8$	0	2.576	-/+0.8

A.2.2. Atmospheric errors

Particularly for applications at volcanoes, it is important to show that the signal measured in the InSAR time-series is caused primarily by surface displacement, rather than atmospheric phase delays. The topography of volcanic edifices typically has a near-axisymmetric (conical) geometry, which correlates, inversely or directly, with an InSAR-detected dis-

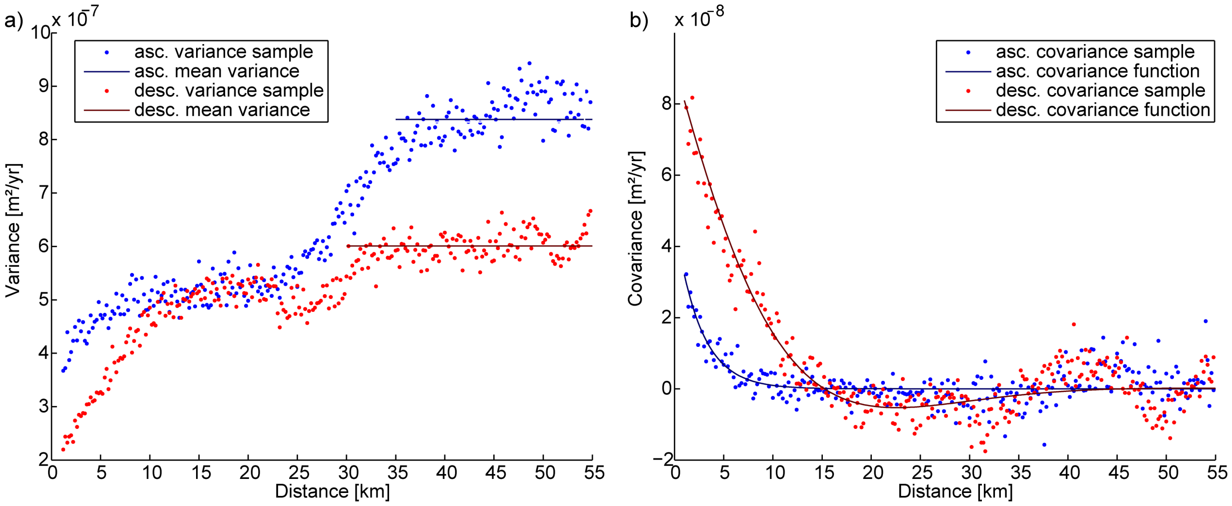

Figure A.6.: Spatial error of average displacement velocity. a) Semi-variograms of the ascending and descending line-of-sight deformation velocities. The horizontal lines mark the distance range of the variance estimations and the variance values of each dataset. b) Co-variograms of the ascending and descending line-of-sight deformation velocities and the corresponding covariance functions (solid lines) of the functional form $g(r) = a \cdot e^{-\frac{r}{p}} \cdot cos(2\pi f \cdot r)$.

placement field arising from any near-axisymmetric deformation source located directly below the volcano. Variations in atmospheric properties, especially humidity changes, can also strongly affect the InSAR signal. In particular, if atmospheric structure around the volcano is correlated to edifice topography, such atmospheric effects may be incorrectly interpreted as displacement.

To address this issue, we show several independent interferograms that span different times with different temporal baselines for each satellite track (Fig.A.7 & A.8). The signal in these interferograms is the radar phase change or shift in the line-of-sight (LOS). These images show that the signal, in particular the sign of the signal, at the volcano is consistent over time in both satellite tracks. Moreover, interferograms with short temporal baselines show low amplitude signals, whereas interferograms with long temporal baselines show high amplitude signals. These observations indicate that the observed signal is caused by displacement of the Earth's surface rather than any atmospheric influences, since effects of the latter are unlikely to produce such consistency in the signal.

To further illustrate the relationship of the measured displacement to the topographic elevation, we have plotted east-west oriented profiles through the interferograms (Fig. A.9 & A.10). For easier comparison of the observed signal with the topography, we used the sign convention for LOS phase change, normalized each phase change profile to the maximum value, and set the reference point to the easternmost longitude.

In the ascending track (Fig. A.9), it is clear that although the elevation changes significantly in the east and the west of the volcano, the signal is stable or changes just slightly. In the descending track (Fig. A.10), a similar relationship is seen in the west. In the east, some interferograms indicate a partial correlation between signal and elevation, but others show weak correlation and or even local de-correlation. For both tracks, it is clear that the increase in phase on the western flank of the volcano is offset from the increase in elevation.

In summary, although a minor contribution to the signal from atmospheric delay that is correlated to topography cannot be ruled out completely, the predominant contribution to the InSAR time-series signal comes from displacement of the volcano surface.

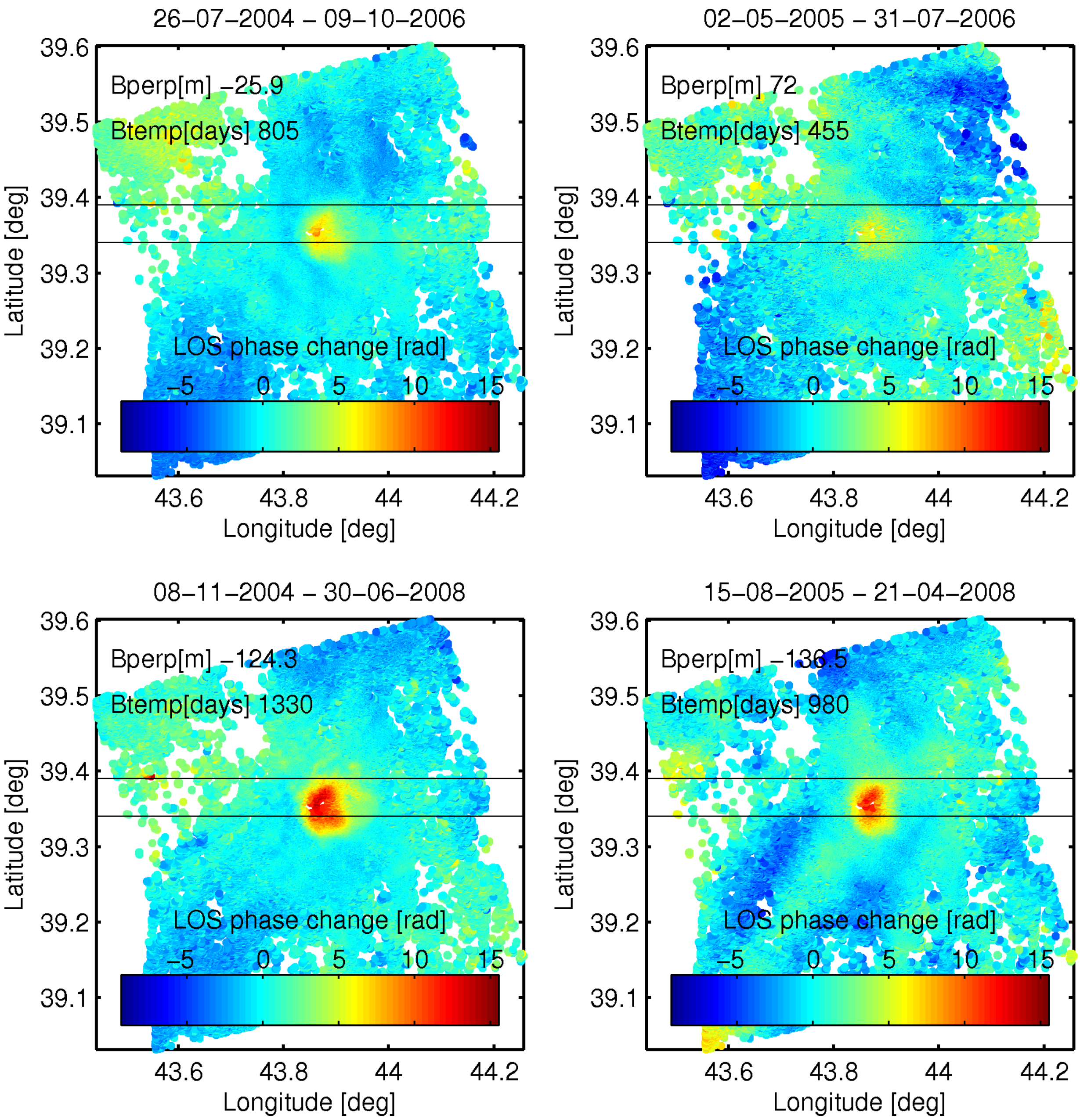

Figure A.7.: Sample interferograms of the ascending track. The title above each image shows the dates of each acquisition in the format day-month-year. We use the sign convention of the slant range change in radar line-of-sight (LOS) in these interferograms in order to illustrate more clearly the relationship of topography to signal. Positive values show range increase in radar LOS and negative values show range decrease in LOS. The two horizontal black lines mark the extent of the east- west profiles shown in figure A.9.

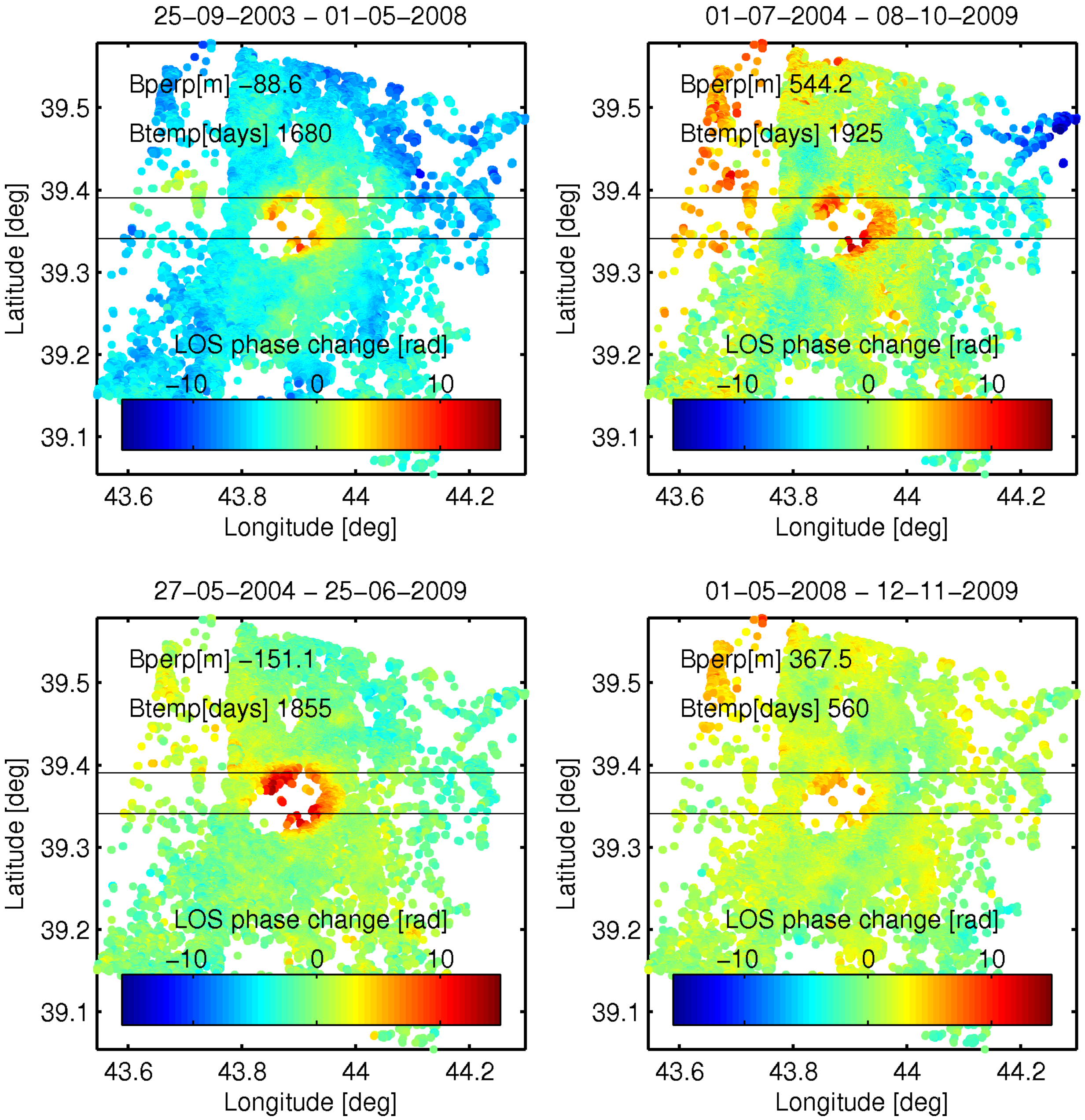

Figure A.8.: Sample interferograms of the descending track. The title above each image shows the dates of each acquisition in the format day-month-year. We use the sign convention of the slant range change in radar line-of-sight (LOS) in these interferograms in order to illustrate more clearly the relationship of topography to signal. Positive values show range increase in radar LOS and negative values show range decrease in LOS. The two horizontal black lines mark the extent of the east- west profiles shown in figure A.10.

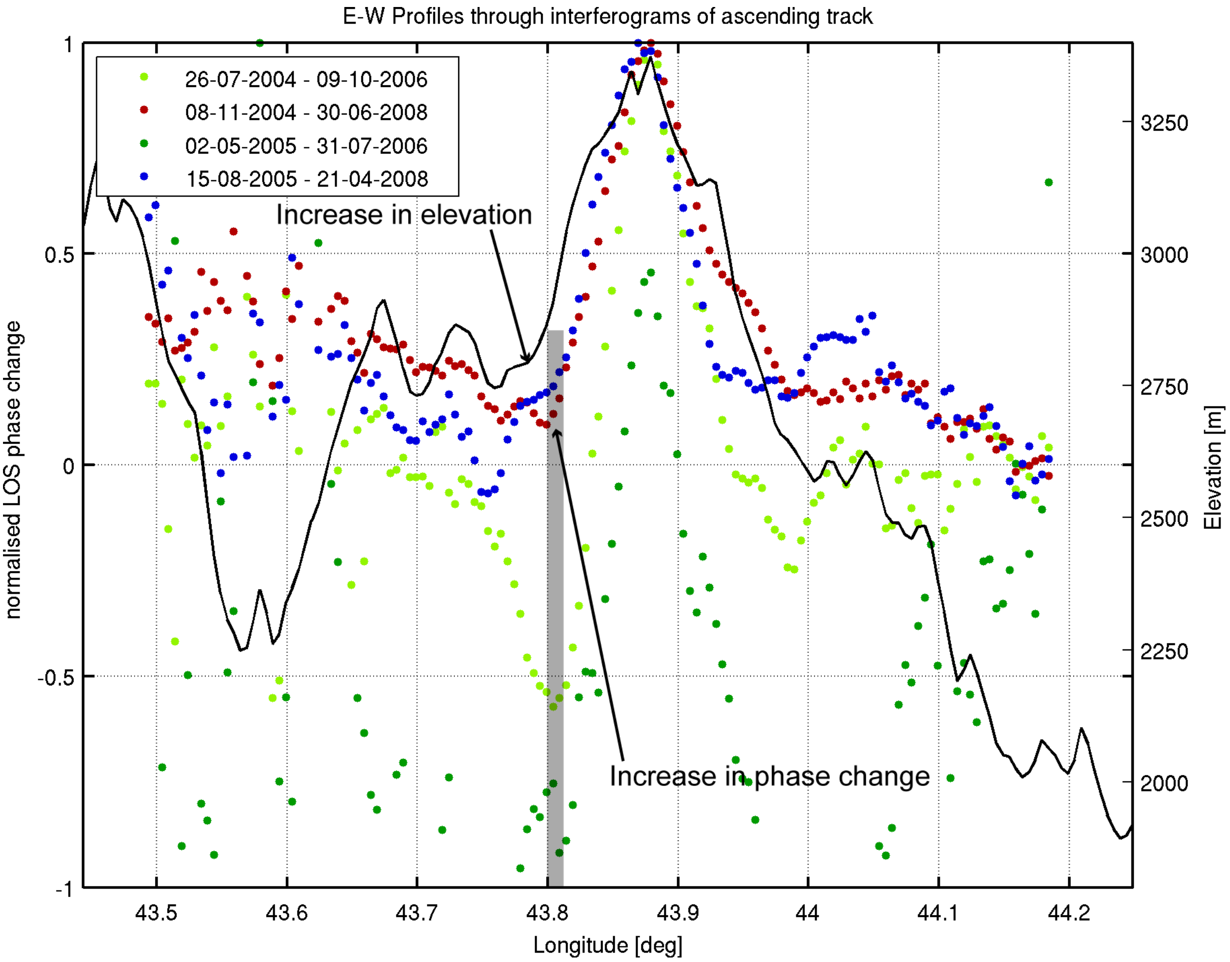

Figure A.9.: East-west profiles taken from the ascending track interferograms of figure A.7 and from the digital elevation model. Colored dots show the normalized phase changes of each sample interferogram. The black continuous line shows the elevation.

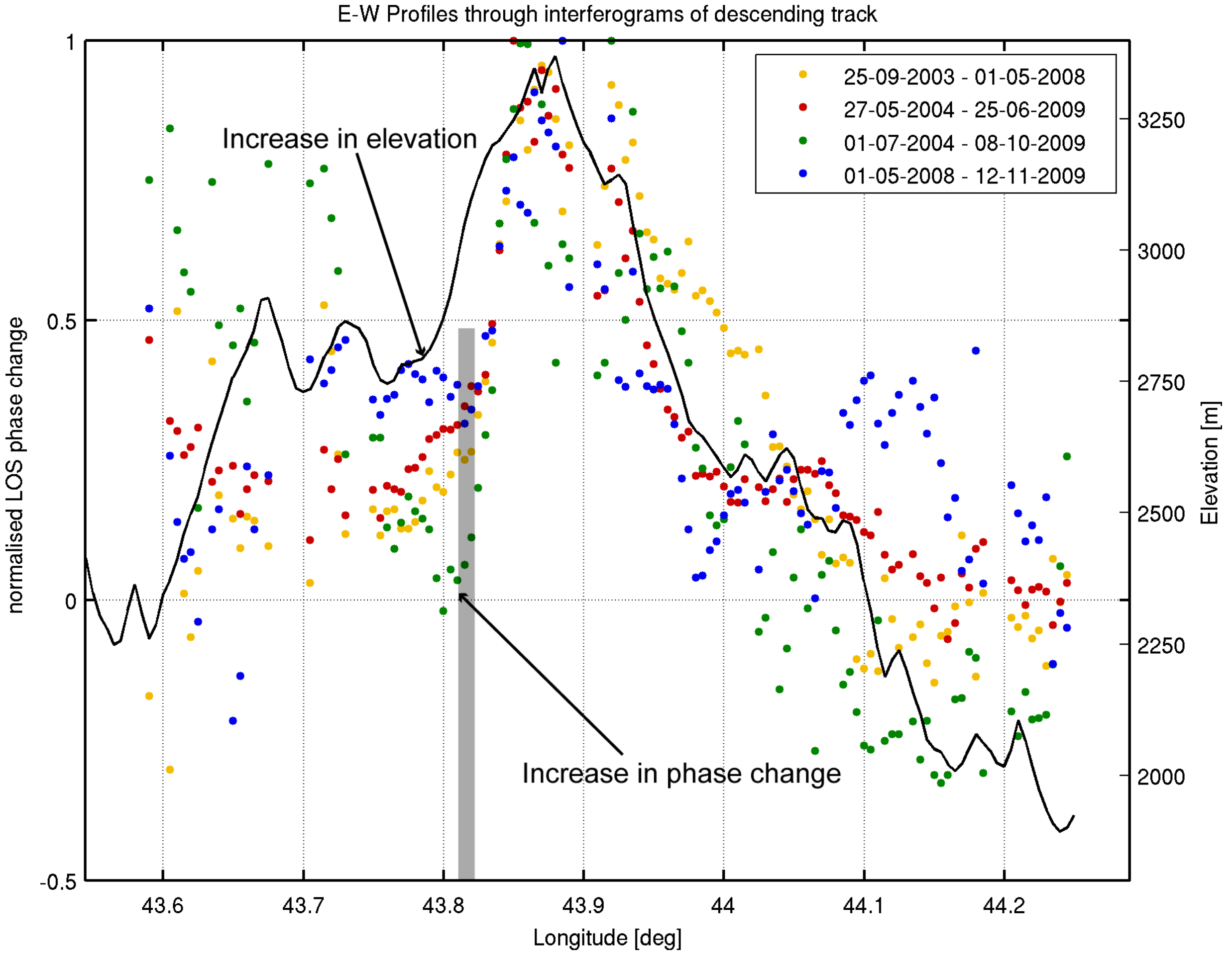

Figure A.10.: East-west profiles taken from the descending track interferograms of figure A.8 and from the digital elevation model. Colored dots show the normalized phase changes of each sample interferogram. The black continuous line shows the elevation.

A.2.3. Model parameter correlation

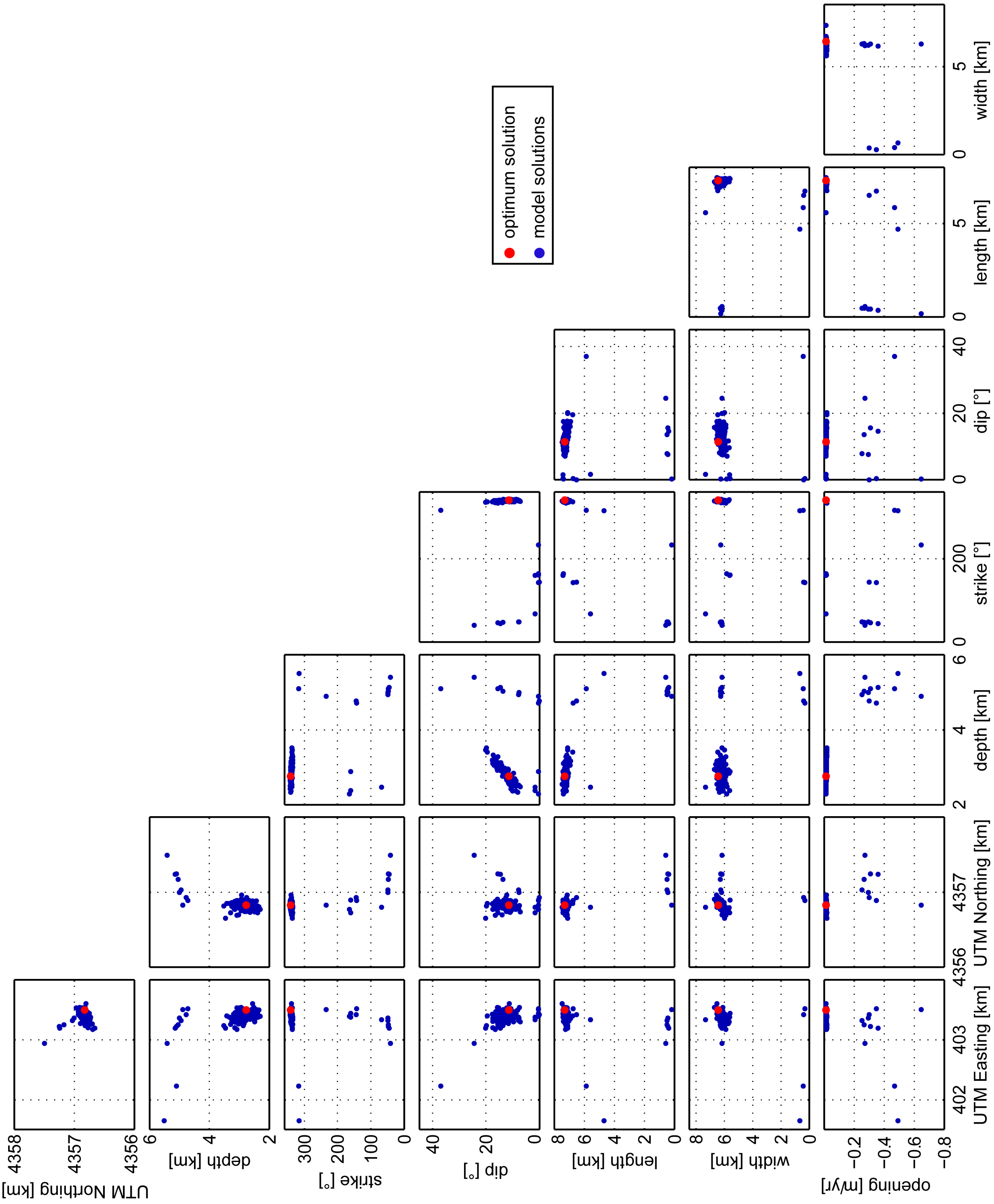

Figure A.11.: Okada model parameter correlations of 200 independent optimization runs.

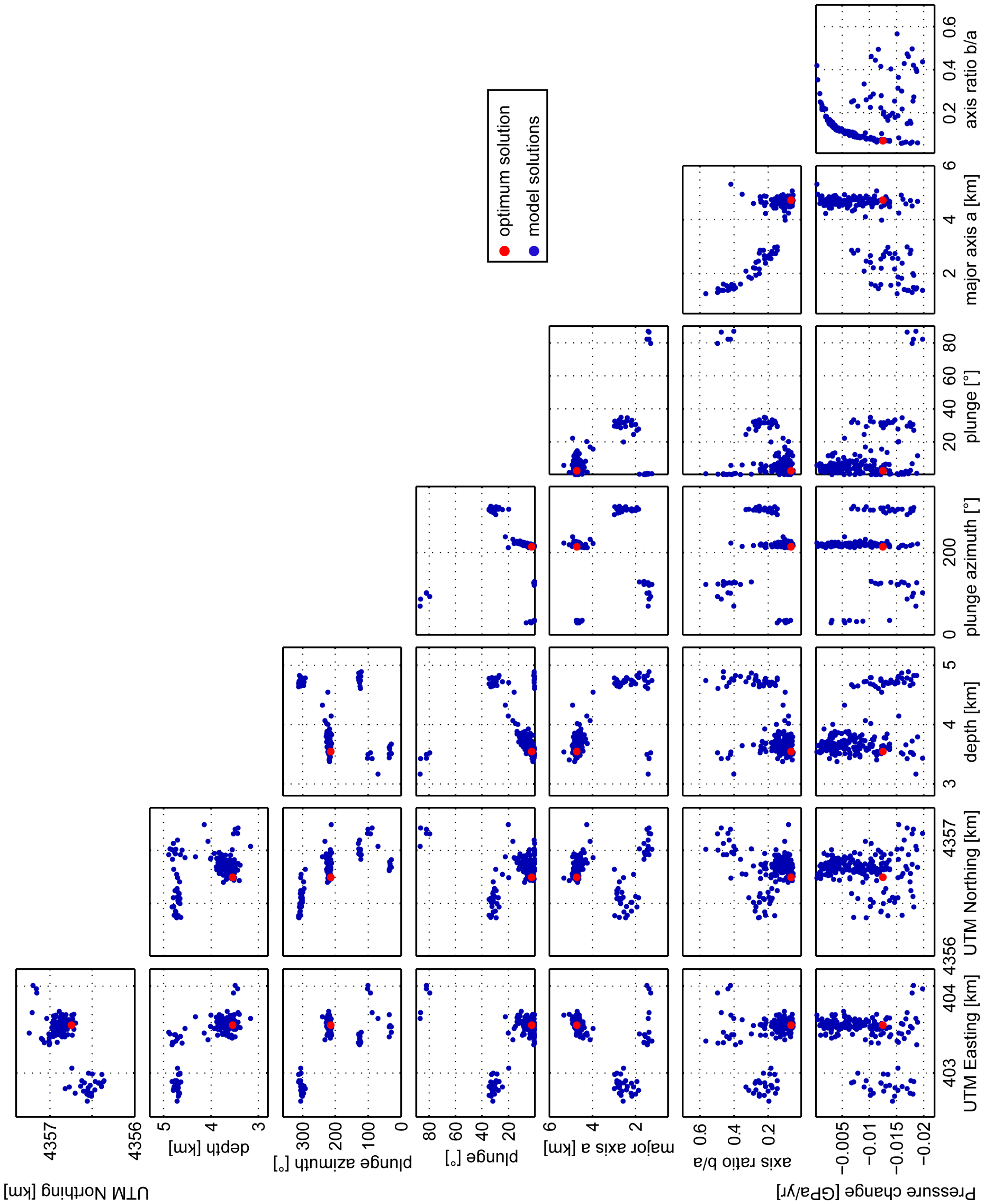

Figure A.12.: Yang model parameter correlations of the 200 optimization results.

A.2.4. Horizontal and vertical displacements

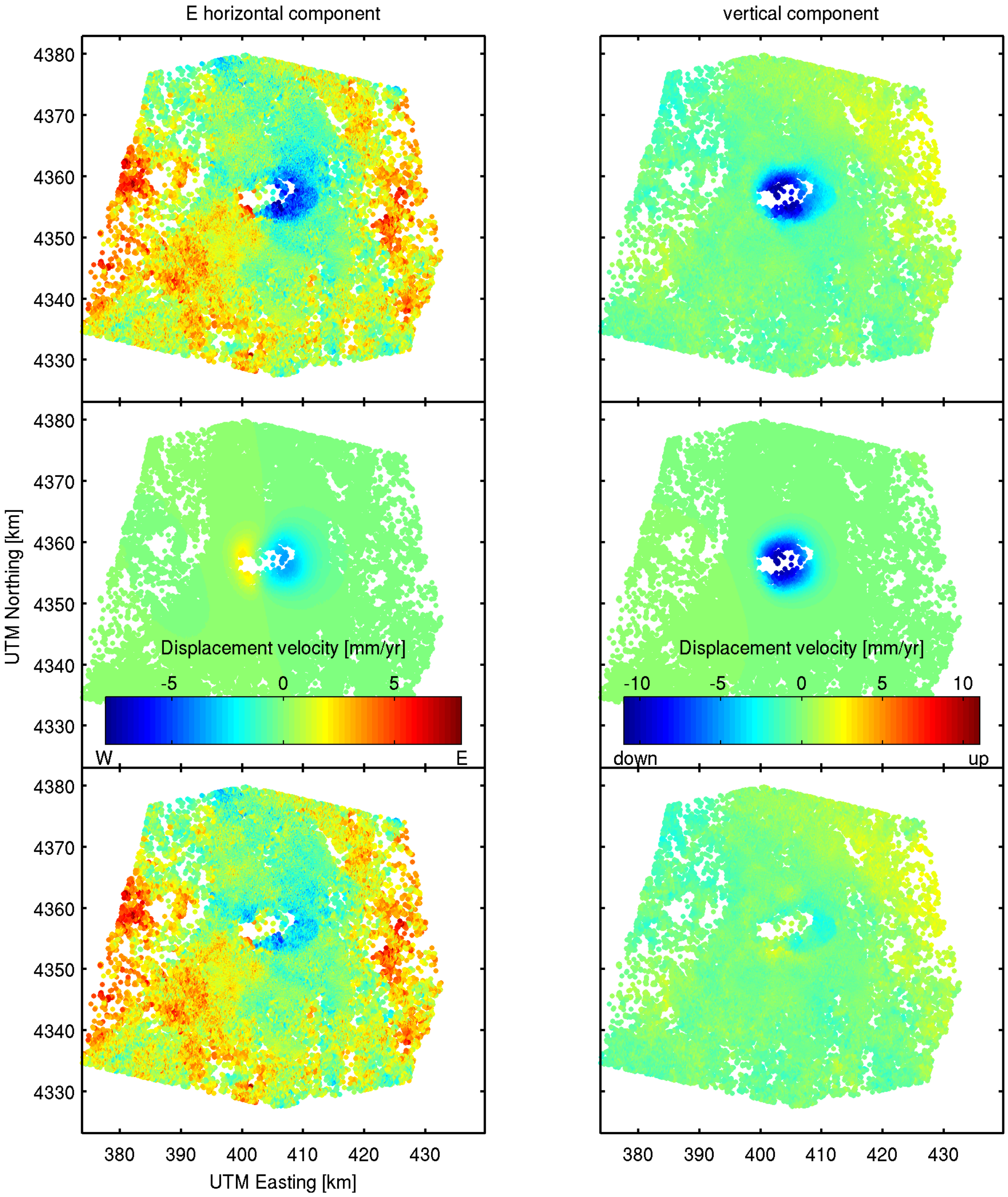

Figure A.13.: East horizontal and vertical components of the InSAR data (top panels), synthetic surface displacements of the optimum Okada source model (middle panels) and residual displacements (bottom panels).

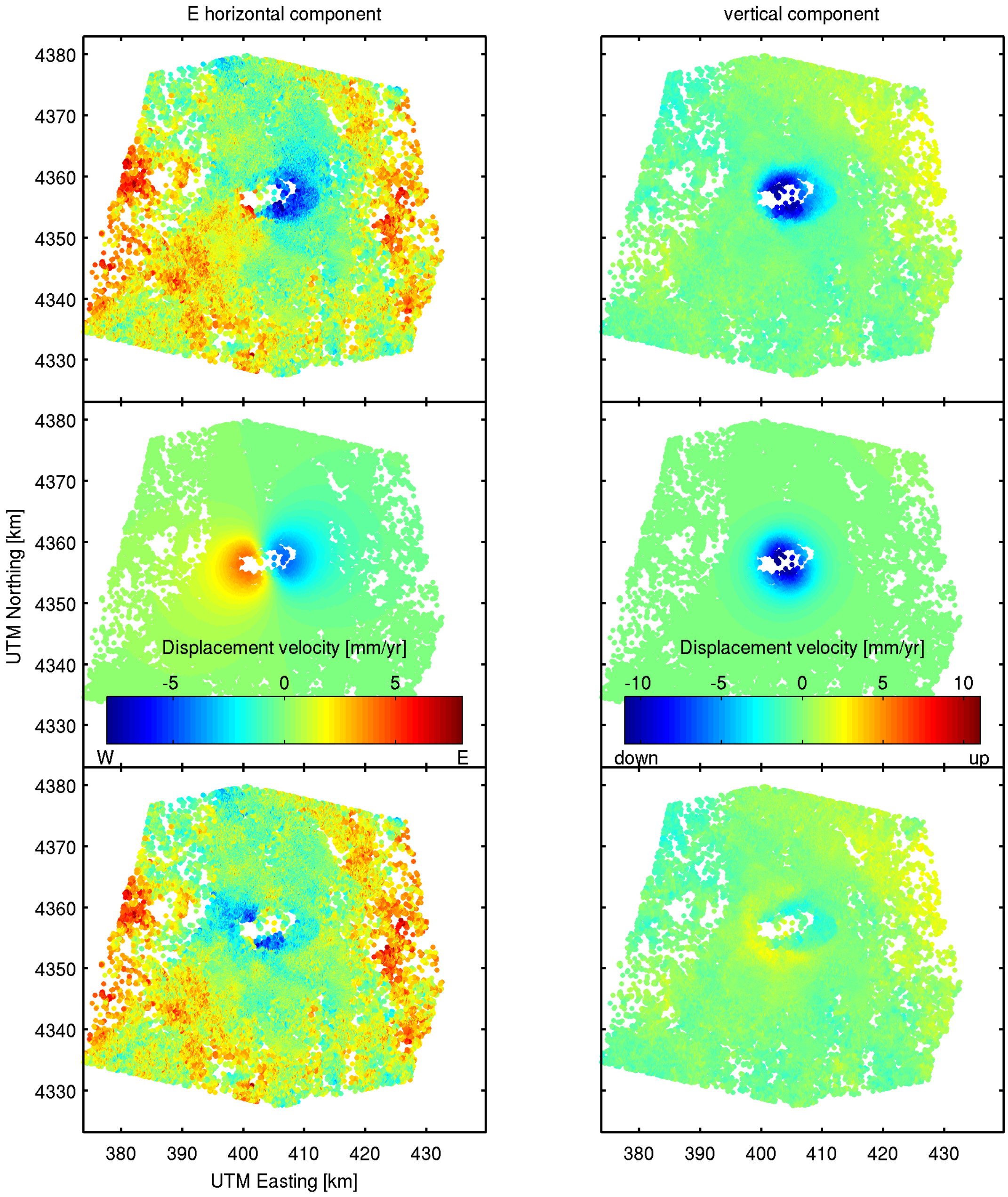

Figure A.14.: East horizontal and vertical components of the InSAR data (top panels), synthetic surface displacements of the optimum Yang source model (middle panels) and residual displacements (bottom panels).

A.3. 3D boundary element model of ring-faulting at Tendürek volcano

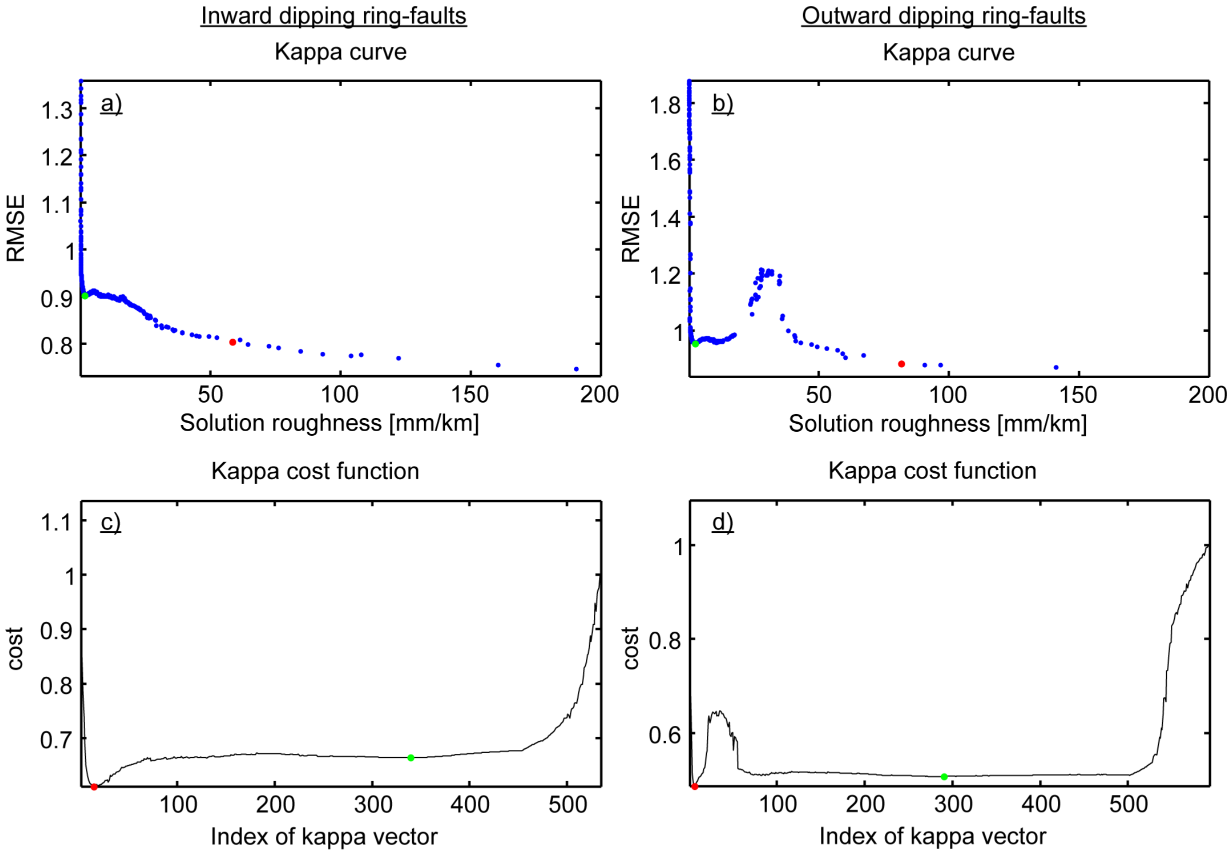

Figure A.15.: Kappa related curves for the inward- and outward-inclined ring-faults: (a & b) RMSE vs. roughness for the inward- and outward-inclined ring-faults. (c & d) κ_{cost}- values on the resulting solution vector (equa.4.5). The red dot indicates the according values for the global minimum solution for κ_{cost}. The green dot marks the according local minimum values for the κ_{cost} that has been used in the final slip distributions (Fig. 4.6).

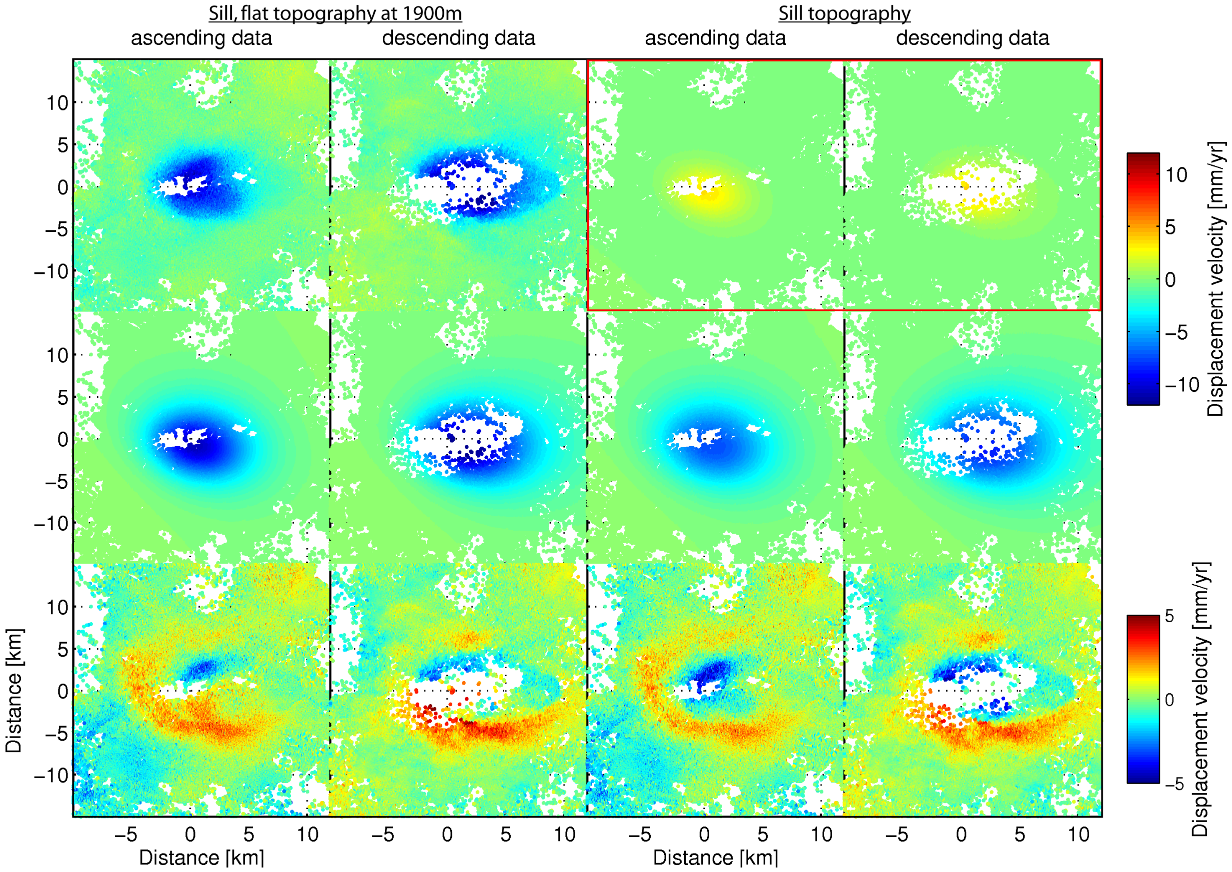

Figure A.16.: Left columns: 3D BEM sill with flat surface at 1,900 m a.s.l.; right columns: 3D BEM sill with real topography. Top panels: Left: Displacement velocities for the ascending and descending tracks, respectively. Right: Difference of the synthetic displacement velocities of the optimum source models in the middle panels by using a sill-like source with flat surface and real topography, respectively. Bottom row: Residual displacement velocities in each satellite track for the 3D sill-like sources with flat surface and real topography, respectively.

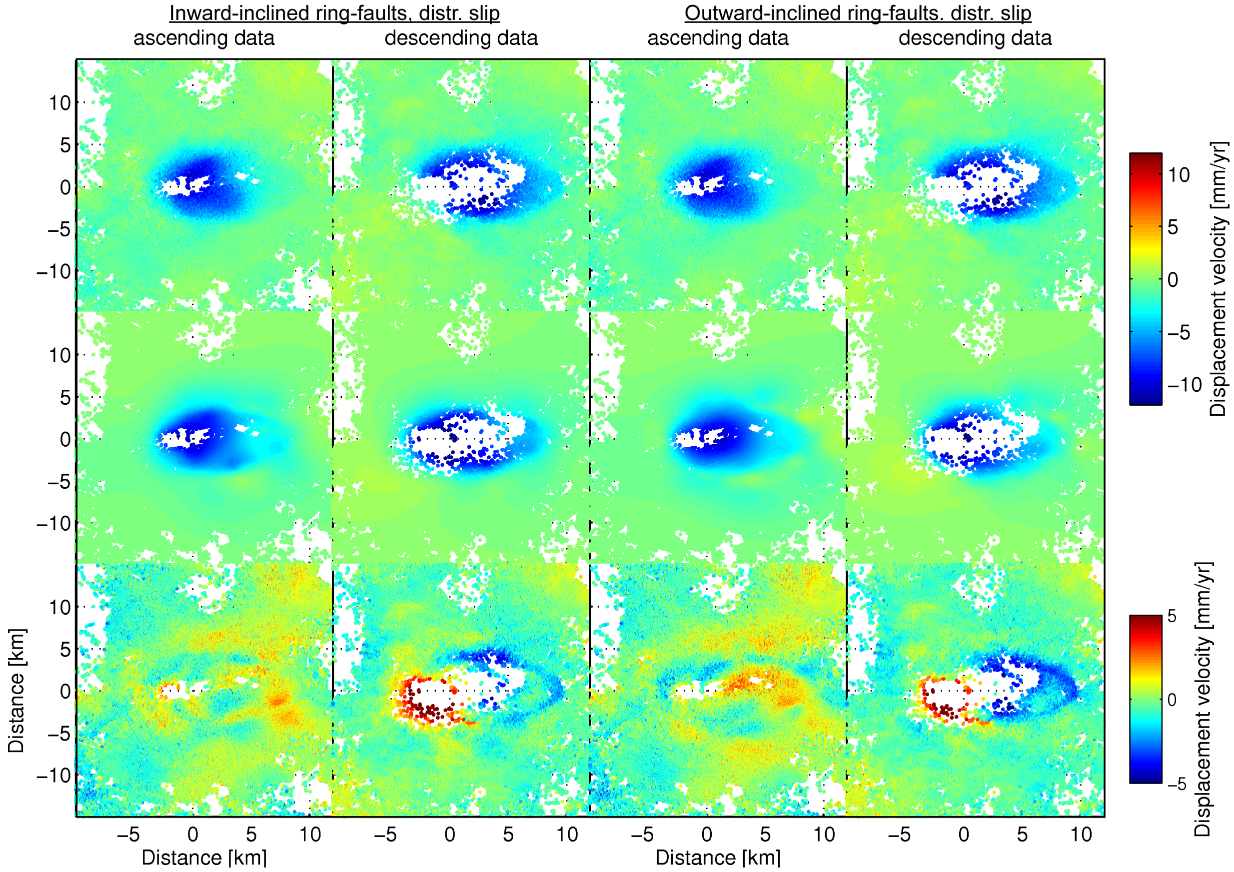

Figure A.17.: Distributed slip data fit for global minimum κ_{cost}: Left columns: Sill-like source and inward-inclined ring-faults. Right columns: Sill-like source and outward-inclined ring-faults. Top panels: Displacement velocities for the ascending and descending tracks, respectively. Middle panels: Modeled optimum displacement velocities for the ascending and descending tracks, respectively. Bottom row: Residual displacement velocities in each satellite track.

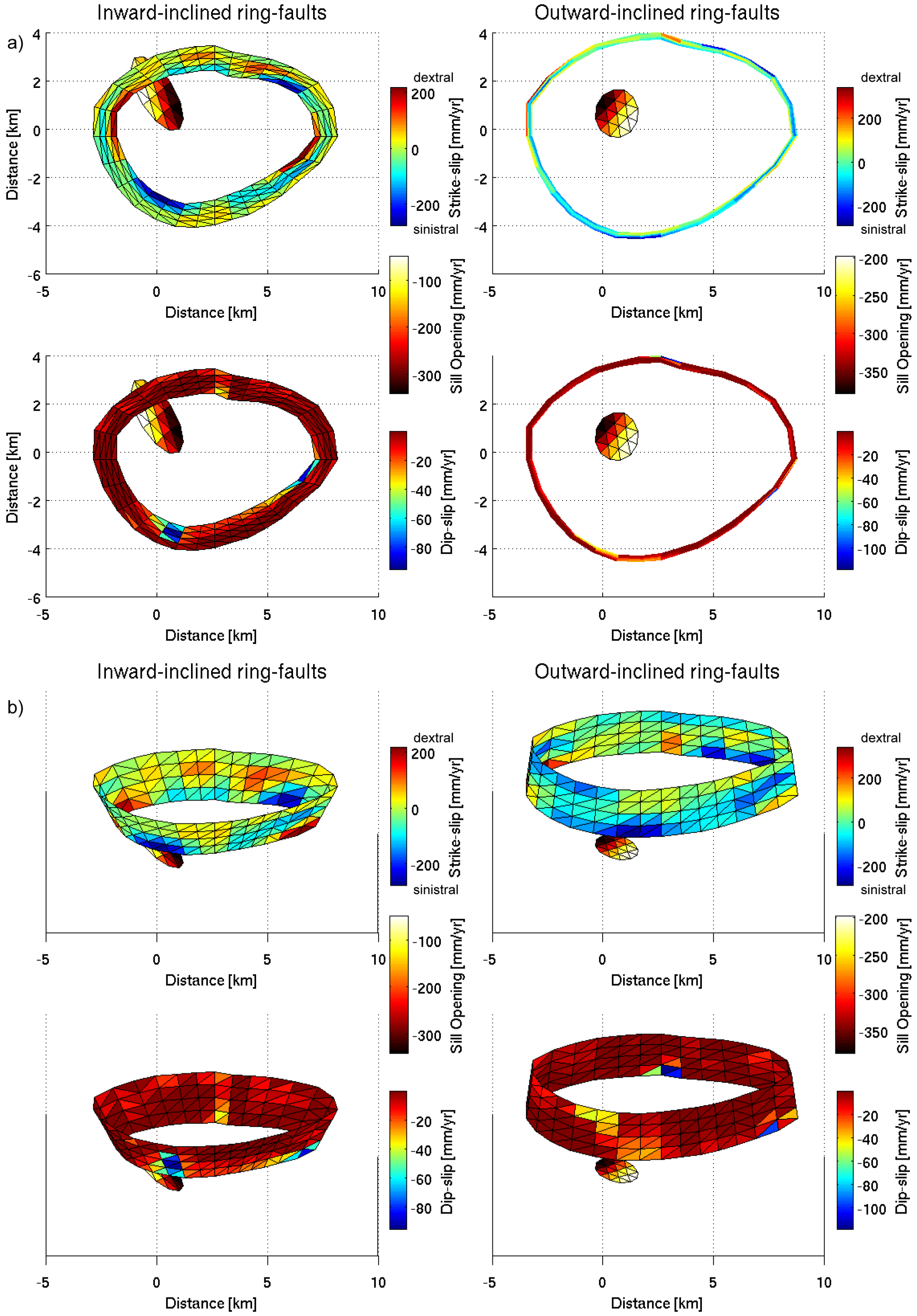

Figure A.18.: Distributed slip for global minimum κ_{cost}: a) Top view: Left: Inward-inclined ring-faults. Right: Outward inclined ring-faults. Top panels: Estimated strike-slip distribution; red and blue colors represent a dextral and sinistral strike-slip direction, respectively. Bottom panels: Dip-slip distribution; red and blue colors show stable and slipping elements, respectively. b) Perspective view, same as a).

A.4. Subsampling: Designed Pixel Subsampling

With data subsampling we aim to reduce the full data set drastically, without loss of information. Designed pixel subsampling (DPS) optimizes the distribution of a chosen number of pixels N_{sub} that are selected from a data set with respect to a given input model. This input model has to be chosen beforehand, as described in section 5.3.2. Our synthetic test (sections 5.3.3, 5.4.1) shows, however, that the dependence of the particular model parameter results on the input model for the problem studied here is negligible. The system of equations for the parametric 'least squares' method, which relates a model to the observations, can be written as (Berné and Baselga 2004):

$$\mathbf{Ax} = \mathbf{d} - \mathbf{v} \tag{A.1}$$

A is the design matrix, **x** are the model parameters (depth, location,...), **d** is the data vector (in this case deformation velocity) and **v** is the difference between the data and what the model is able to describe - the residual.
The design matrix **A** is dependent on the partial derivative of the displacement **F** in the line-of-sight, with respect to each input model parameter x_{sub}:

$$\mathbf{A} = \left.\frac{\partial \mathbf{F}}{\partial \mathbf{x}}\right|_{x_1}^{x_M} \tag{A.2}$$

with M being the number of model parameters. Therefore, **A** is an expression of the sensitivity of each parameter to small changes. As some of the model parameters (e.g., depth, dip) have different units, we weight **A** to be able to compare different columns of **A** without favoring one or the other model parameter. We calculate the weighting matrix **P** as the ratio of the element-wise inverse of **A** and the sum of this inverse over all input model parameters:

$$\mathbf{P} = \frac{\frac{1}{A_{ij}}}{\sum_{i=1}^{M} \frac{1}{A_{ij}}} \tag{A.3}$$

In this way **P** represents the normalized finite change of each model parameter that is necessary to produce the line-of-sight displacement of 1 cm at a data point. By adding up all the weighted gradients $P_{ij} \cdot A_{ij}$ of the model parameters i for every data point j, we derive the model sensitivity w_i:

$$w_j = \sum_{i=1}^{M} P_{ij} \cdot A_{ij} \tag{A.4}$$

with $j = 1, \ldots, N$, where N is the number of data points. The model sensitivity w_i controls the subsampling. When we select data points with high sensitivity rather than those with low sensitivity, we may be keeping the total sensitivity of the data high while reducing the number of observations. We enable the sensitivity-based subsampling by assigning a probability to each data point to be picked. For that we normalize all the model sensitivities w_i at the position of the observation with the total sensitivity S:

$$S = \sum_{j=1}^{N} w_i \tag{A.5}$$

to the normalized model sensitivities s_j :

$$s_j = \frac{w_j}{S} \tag{A.6}$$

with $\sum_{j=1}^{N} s_j$, and $s_0 = 0$. In practice for the subsampling, we take the cumulative sum of each normalized model sensitivity s_j to determine the lower (s_{j-1}) and upper (s_j) bound of an interval, where its width is defined by the normalized model sensitivity s_j. Thus, to create a subsampled data set $\mathbf{d}_{sub}$ we generate a vector $\mathbf{u}$ with random numbers $u_r \epsilon [0, 1]$ and the length of N_{sub}, the desired number of subsampled pixels. Each u_r then represents the j-th data point if it meets the criteria $s_{j-1} < u_r \leqq s_j$. For example, for a data set with only two pixels, where pixel 1 has a normalized model sensitivity of $s_1 = 0.4$, pixel 1 will be selected if $0 < u_r \leqq 0.4$, otherwise pixel 2 is selected. The resulting points in the set $\mathbf{l}_{sub}$ have a high probability of being generally sensitive to the model parameters. Additional to high model sensitivity we need a good spatial distribution of the subsampled points, to well constrain the model parameters. The according design matrix $\mathbf{A}_{sub}$ and the empirically determined data error variance-covariance matrix $\mathbf{C}$ can be used to calculate $\mathbf{C}_{mod}$, which is the variance-covariance matrix of the model parameters:

$$\mathbf{C}_{mod} = \left(\mathbf{A}_{sub}^{T} \mathbf{C} \mathbf{A}_{sub}\right)^{-1} \tag{A.7}$$

Small trace values of $\mathbf{C}_{mod}$ mean little correlation and therefore, high precision between the input model parameters. Thus by creating repeatedly (K - times) different sets of random numbers $\mathbf{u}_k$, and therefore $\mathbf{d}_{sub,k}$, $\mathbf{A}_{sub,k}$ with different $\mathbf{C}_{mod,k}$, for $k = 1, ..., K$, we could choose from several sets the one with the highest precision regarding the input model $\mathbf{x}$, by finding the smallest values for the trace t_k of the variance-covariance matrices $\mathbf{C}_{mod,k}$ (Berné and Baselga 2004):

$$\mathbf{t} = trace\left(\mathbf{C}_{mod,k}\right)\Big|_{k=1}^{K} \tag{A.8}$$

As an additional criterion for finding a good distribution of points, we calculate the condition number from $\mathbf{A}_{sub,k}$, which is a measure of the uniqueness of the pixel distributions:

$$\mathbf{g} = cond\left(\mathbf{A}_{sub,k}\right)\Big|_{k=1}^{K} \tag{A.9}$$

Aiming at good point distributions we now combine both of these criteria and define a performance B as the Hadamard product of the traces $\mathbf{t}$ and the condition numbers $\mathbf{g}$:

$$\mathbf{B} = \mathbf{t} \circ \mathbf{g} \tag{A.10}$$

The minimum of the performances $B_{opt} = min(\mathbf{B})$ finally indicates the data set $\mathbf{l}_{sub,k}$ with the optimum distribution of subsampled points.
The number of repetitions K becomes more important if the number of subsampled data points N_{sub} is low (Fig. 5.1). In this case the range of resulting $\mathbf{B}$ increases, with decreasing N_{sub}. With large K's, we have a better chance of getting a well-designed subsampled data set than we would have with little or no repetitions.

B. Acknowledgments

First of all I want to thank my supervisor Thomas Walter for giving me the opportunity to do this PhD. His door was always open for discussion and there was never anything “impossible”. While getting my diploma thesis, he offered me an opportunity to work with SAR data, that’s when I unexpectedly fell in love with the “fringes”.

My very special thanks go to my two Persian friends Manoochehrjoon and Mehdijan. Both of them made my life so much easier and brighter with a lot of unforgettable jokes and laughs in the office and during various ceremonies. I’m very grateful for having met them and experiencing such a rich and unquestioned friendship- Merci.

I thank Henriette and Eoghan for teaching me about what quality really means, for being accassory supervisors and for reading and correcting the assemblage of letters and words that I produced and transforming them to manuscripts, over and over again.

In the office I met several people who shared and carried the same weight of doing a PhD and I want to thank them for their companionship especially Silke, Ade, Olja, Camilla, Michele, Elena and Katrin. Also I want to thank the older generation of PhD students, Joel and Andrea from whom I learned a lot. I am especially grateful for their mental support.

The probably most important person of the last ten years of my life was Babbel and I want to thank him for having been a very patient room-mate, for sharing the long road of studying up to the PhD, and of course for his long-lasting friendship.

Also my special thanks go to Adrian and the “Spinner” for letting me see and feel the “real” world and for providing to me an opportunity to counter the mental work with physical activity.

I want to thank my father for awaking the interest for natural sciences in myself and teaching me how to work careful and accurate. I want to thank my mother, my brothers and my grand-mothers for being a warm and homely haven. They have always kept their ears opened for all minor and big problems of mine, have given me comfort and put me back on my feet when I lay “crushed” on the floor.

Finally I want to thank my beloved fiance Olha, who has taken the annoying ’hore’ to correct my horrible english language in this thesis. She showed me that life does not only consist of PhD and computers. She gives me the feeling of “home” and will hopefully further be on my side all the years to come.

C. Bibliography

Ahuja, R., Magnati, T. and Orlin, J.: 1993, *Network Flows: Theory, Algorithms, and Applications.*, NY, Prentice- Hall.

Ali, S. T. and Feigl, K. L.: 2012, A new strategy for estimating geophysical parameters from InSAR data: Application to the Krafla central volcano in Iceland, *Geochemistry Geophysics Geosystems* **13**(6), 1–18.
URL: *http://www.agu.org/pubs/crossref/2012/2012GC004112.shtml*

Anderson, E.: 1936, The dynamics of the formation of cone sheets, ring dykes, and cauldron subsidence, *Proc. Indian Acad. Sci.* **56**, 128–163.

Bathke, H., Sudhaus, H., Holohan, E., Walter, T. R. and Shirzaei, M.: 2013, An active ring fault detected at Tendürek volcano by using InSAR, *Journal of Geophysical Research: Solid Earth* **118**(8), 4488–4502.
URL: *http://doi.wiley.com/10.1002/jgrb.50305*

Battaglia, M., Troise, C., Obrizzo, F., Pingue, F. and De Natale, G.: 2006, Evidence for fluid migration as the source of deformation at Campi Flegrei caldera (Italy), *Geophysical Research Letters* **33**(1), 1–4.
URL: *http://www.agu.org/pubs/crossref/2006/2005GL024904.shtml*

Beauducel, F., Natale, G. D., Obrizzo, F. and Pingue, F.: 2004, 3-D Modelling of Campi Flegrei Ground Deformations: Role of Caldera Boundary Discontinuities, *Pure and Applied Geophysics* **161**(7), 1329–1344.

Berardino, P., Fornaro, G., Lanari, R., Member, S. and Sansosti, E.: 2002, A New Algorithm for Surface Deformation Monitoring Based on Small Baseline Differential SAR Interferograms, *IEEE Transactions on Geoscience and Remote Sensing* **40**(11), 2375–2383.

Berné, J. L. and Baselga, S.: 2004, First-order design of geodetic networks using the simulated annealing method, *Journal of Geodesy* **78**(1-2), 47–54.

Biggs, J., Anthony, E. and Ebinger, C.: 2009, Multiple inflation and deflation events at Kenyan volcanoes, East African Rift, *Geology* **37**(11), 979–982.
URL: *http://geology.gsapubs.org/cgi/doi/10.1130/G30133A.1*

Bonaccorso, a., Cianetti, S., Giunchi, C., Trasatti, E., Bonafede, M. and Boschi, E.: 2005, Analytical and 3-D numerical modelling of Mt. Etna (Italy) volcano inflation, *Geophysical Journal International* **163**(2), 852–862.
URL: *http://gji.oxfordjournals.org/cgi/doi/10.1111/j.1365-246X.2005.02777.x*

Bouvet de Maisonneuve, C., Dungan, M. A., Bachmann, O. and Burgisser, A.: 2012a, Insights into shallow magma storage and crystallization at Volcán Llaima (Andean Southern Volcanic Zone, Chile), *Journal of Volcanology and Geothermal Research* **211-212**, 76–91.
URL: *http://linkinghub.elsevier.com/retrieve/pii/S0377027311002538*

Bouvet de Maisonneuve, C., Dungan, M. A., Bachmann, O. and Burgisser, A.: 2012b, Petrological Insights into Shifts in Eruptive Styles at Volcan Llaima (Chile), *Journal of Petrology* **54**(2), 393–420.
URL: *http://www.petrology.oxfordjournals.org/cgi/doi/10.1093/petrology/egs073*

Branney, M. J.: 1995, Downsag and extension at calderas: new perspectives on collapse geometries from ice-melt, mining, and volcanic subsidence, *Bulletin of Volcanology* **57**(5), 303–318.

Byrne, P. K., Holohan, E. P., Kervyn, M., van Wyk de Vries, B., Troll, V. R. and Murray, J. B.: 2013, A sagging-spreading continuum of large volcano structure, *Geology* **41**(3), 339–342.
URL: *http://geology.gsapubs.org/cgi/doi/10.1130/G33990.1*

Byrne, P. K., van Wyk de Vries, B., Murray, J. B. and Troll, V. R.: 2009, The geometry of volcano flank terraces on Mars, *Earth and Planetary Science Letters* **281**(1-2), 1–13.

Cayol, V. and Cornet, F. H.: 1997, 3D Mixed Boundary Elements for Elastostatic Deformation Field Analysis, *Stress: The International Journal on the Biology of Stress* **34**(2), 275–287.

Cayol, V. and Cornet, F. H.: 1998, Three-dimensional modeling of the 1983-1984 eruption at Piton de la Fournaise Volcano , Réunion Island, *Journal of Geophysical Research* **103**, 18,025–18037.

Cecchi, E., Wyk de Vries, B. and Lavest, J.-M.: 2004, Flank spreading and collapse of weak-cored volcanoes, *Bulletin of Volcanology* **67**(1), 72–91.
URL: *http://www.springerlink.com/index/10.1007/s00445-004-0369-3*

Chadwick, W. W., Geist, D. J., Jónsson, S., Poland, M., Johnson, D. J. and Meertens, C. M.: 2006, A volcano bursting at the seams: Inflation, faulting, and eruption at Sierra Negra volcano, Galápagos, *Geology* **34**(12), 1025.
URL: *http://geology.gsapubs.org/cgi/doi/10.1130/G22826A.1*

Chen, C. W. and Zebker, H. A.: 2001, Two-dimensional phase unwrapping with use of statistical models for cost functions in nonlinear optimization, *Journal of the Optical Society of America A* **18**, 338–351.

Clough, C., Maufe, H. and Baley, E.: 1909, The cauldron subsidence of Glen-Coe, and the associated igneous phenomena., *Q.J.Soc. Lond.* **65**, 611–678.

Constantini, M.: 1998, A Novel Phase Unwrapping Method Based on Network Programming, *IEEE Transactions on Geoscience and Remote Sensing* **36**(3), 813–821.

Dare, P. and Saleh, H.: 2000, GPS network design: logistics solution using optimal and near-optimal methods, *Journal of Geodesy* **74**(6), 467–478.

Dawson, J. and Tregoning, P.: 2007, Uncertainty analysis of earthquake source parameters determined from InSAR: A simulation study, *Journal of Geophysical Research* **112**(B9), 1–13.
URL: *http://www.agu.org/pubs/crossref/2007/2007JB005209.shtml*

De Natale, G., Troise, C., Pingue, F., Mastrolorenzo, G., Pappalardo, L., Battaglia, M. and Boschi, E.: 2006, The Campi Flegrei caldera: unrest mechanisms and hazards, *Mechanisms of Activity and Unrest at Large Calderas*, Vol. 269, Geological Society, London, pp. 25–45.

Delouis, B., Giardini, D., Lundgren, P. and Salichon, J.: 2002, Joint Inversion of In SAR , GPS , Teleseismic , and Strong-Motion Data for the Spatial and Temporal Distribution of Earthquake Slip : Application to the 1999 Izmit Mainshock, *Bulletin of the Seismological Society of America* **92**(1), 278–299.

Dhont, D. and Chorowicz, J.: 2005, Review of the neotectonics of the Eastern Turkish-Armenian Plateau by geomorphic analysis of digital elevation model imagery, *International Journal of Earth Sciences* **95**(1), 34–49.

Doğan, B. and Karakaş, A.: 2013, Geometry of co-seismic surface ruptures and tectonic meaning of the 23 October 2011 Mw 7.1 Van earthquake (East Anatolian Region, Turkey), *Journal of Structural Geology* **46**, 99–114.
URL: *http://linkinghub.elsevier.com/retrieve/pii/S0191814112002210*

Dzierma, Y. and Wehrmann, H.: 2010, Eruption time series statistically examined: Probabilities of future eruptions at Villarrica and Llaima Volcanoes, Southern Volcanic Zone, Chile, *Journal of Volcanology and Geothermal Research* **193**(1-2), 82–92.
URL: *http://linkinghub.elsevier.com/retrieve/pii/S0377027310001009*

Dzurisin, D.: 2007, *Volcano Deformation; Geodetic Monitoring Techniques*, Springer-Verlag, Berlin Heidelberg New York.

Dzurisin, D., Poland, M. and Bürgmann, R.: 2002, Steady subsidence of Medicine Lake volcano, northern California, revealed by repeated leveling surveys, *Journal of Geophysical Research* **107**(B12), 2372.
URL: *http://doi.wiley.com/10.1029/2001JB000893*

Ebmeier, S. K., Biggs, J., Mather, T. a. and Amelung, F.: 2013, On the lack of InSAR observations of magmatic deformation at Central American volcanoes, *Journal of Geophysical Research: Solid Earth* **118**(5), 2571–2585.
URL: *http://doi.wiley.com/10.1002/jgrb.50195*

Ekström, G.: 1994, Anomalous earthquakes on volcano ring-fault structures, *Earth and Planetary Science Letters* **128**, 707–712.

Farr, T. G., Rosen, P. A., Caro, E., Crippen, R., Duren, R., Hensley, S., Kobrick, M., Paller, M., Rodriguez, E., Roth, L., Seal, D., Shaffer, S., Shimada, J., Umland, J., Werner, M., Oskin, M., Burbank, D. and Alsdorf, D.: 2007, The shuttle radar topography mission, *Rev. Geophys.* **45**(2005), 1–33.

Feigl, K. L. and Thurber, C. H.: 2009, A method for modelling radar interferograms without phase unwrapping: application to the M 5 Fawnskin, California earthquake of 1992 December 4, *Geophysical Journal International* **176**(2), 491–504.
URL: *http://blackwell-synergy.com/doi/abs/10.1111/j.1365-246X.2008.03881.x*

Ferretti, A., Prati, C. and Rocca, F.: 2001, Permanent Scatterers in SAR Interferometry, *IEEE Transactions on geoscience and remote sensing* **39**(1), 8–20.

Ferretti, A., Savio, G., Barzaghi, R., Borghi, A., Musazzi, S., Novali, F., Prati, C. and Rocca, F.: 2007, Submillimeter Accuracy of InSAR Time Series: Experimental Validation, *IEEE Transactions on Geoscience and Remote Sensing* **45**(5), 1142–1153.
URL: *http://ieeexplore.ieee.org/lpdocs/epic03/wrapper.htm?arnumber=4156314*

Fichtner, A. and Tkalčić, H.: 2010, Insights into the kinematics of a volcanic caldera drop: Probabilistic finite-source inversion of the 1996 Bárdarbunga, Iceland, earthquake, *Earth*

and Planetary Science Letters **297**(3-4), 607–615.
URL: *http://linkinghub.elsevier.com/retrieve/pii/S0012821X10004516*

Filson, J., Simkin, T. and Leu, L.-k.: 1973, Seismicity of a caldera collapse: Galapagos Islands 1968, *Journal of Geophysical Research* **78**(35), 8591–8622.
URL: *http://doi.wiley.com/10.1029/JB078i035p08591*

Fournier, R. O.: 1999, Hydrothermal Processes Related to Movement of Fluid From Plastic into Brittle Rock in the Magmatic-Epithermal Environment, *Economic Geology* **94**, 1193–1211.

Fournier, T. J., Pritchard, M. E. and Riddick, S. N.: 2010, Duration, magnitude, and frequency of subaerial volcano deformation events: New results from Latin America using InSAR and a global synthesis, *Geochemistry Geophysics Geosystems* **11**(1).
URL: *http://www.agu.org/pubs/crossref/2010/2009GC002558.shtml*

Fukushima, Y., Cayol, V. and Durand, P.: 2005, Finding realistic dike models from interferometric synthetic aperture radar data: The February 2000 eruption at Piton de la Fournaise, *J. Geophys. Res.* **110**(B3), 1–16.

Funning, G. J., Bürgmann, R., Ferretti, A., Novali, F. and Fumagalli, A.: 2007, Creep on the Rodgers Creek fault, northern San Francisco Bay area from a 10 year PS-InSAR dataset, *Geophysical Research Letters* **34**(19), 3–7.
URL: *http://www.agu.org/pubs/crossref/2007/2007GL030836.shtml*

Galle, B., Johansson, M., Rivera, C., Zhang, Y., Kihlman, M., Kern, C., Lehmann, T., Platt, U., Arellano, S. and Hidalgo, S.: 2010, Network for Observation of Volcanic and Atmospheric Change (NOVAC)-A global network for volcanic gas monitoring: Network layout and instrument description, *Journal of Geophysical Research* **115**(D5), 1–19.
URL: *http://www.agu.org/pubs/crossref/2010/2009JD011823.shtml*

Geshi, N., Shimano, T., Chiba, T. and Nakada, S.: 2002, Caldera collapse during the 2000 eruption of Miyakejima Volcano, Japan, *Bulletin of Volcanology* **64**(1), 55–68.
URL: *http://link.springer.com/10.1007/s00445-001-0184-z*

Goldstein, R. M.: 1995, Atmospheric limitations to repeat-track radar interferometry, *Geophysical Research Letters* **22**(18), 2517–2520.

Goldstein, R. M. and Werner, C. L.: 1998, Radar interferogram filtering for geophysical applications, *Geophysical Research Letters* **25**(21), 4035–4038.

Hanssen, R. F.: 2001, *Radar Interferometry*, Kluwer Academic Publishers, Dordrecht.

Holland, J. H.: 1975, *Adaptation in Natural and Artificial Systems*, University of Michigan Press., Oxford.

Holohan, E. P.: 2008, *An Experimental Study of the Geometry and Kinematics of Caldera Collapse*, PhD thesis, University of Dublin, Trinity College.

Holohan, E. P., Schöpfer, M. P. J. and Walsh, J. J.: 2011, Mechanical and geometric controls on the structural evolution of pit crater and caldera subsidence, *Journal of Geophysical Research* **116**(B7), 1–23.
URL: *http://www.agu.org/pubs/crossref/2011/2010JB008032.shtml*

Holohan, E. P., Troll, V. R., van Wyk de Vries, B., Walsh, J. J. and Walter, T. R.: 2008, Unzipping Long Valley: An explanation for vent migration patterns during an elliptical ring fracture eruption, *Geology* **36**(4), 323.
URL: *http://geology.gsapubs.org/cgi/doi/10.1130/G24329A.1*

Holohan, E. P., Walter, T. R., Schöpfer, M. P., Walsh, J. J., van Wyk de Vries, B. and Troll, V. R.: 2013, Origins of oblique-slip faulting during caldera subsidence, *Journal of Geophysical Research: Solid Earth* **118**(4), 1778–1794.
URL: *http://doi.wiley.com/10.1002/jgrb.50057*

Hooper, A.: 2006, *Persistent scatterer radar interferometry for crustal deformation studies and modeling of volcanic deformation*, PhD thesis, Stanford University.

Hooper, A.: 2008, A multi-temporal InSAR method incorporating both persistent scatterer and small baseline approaches, *Geophysical Research Letters* **35**(16).

Hooper, A., Bekaert, D., Spaans, K. and Arıkan, M.: 2012, Recent advances in SAR interferometry time series analysis for measuring crustal deformation, *Tectonophysics* **514-517**, 1–13.
URL: *http://linkinghub.elsevier.com/retrieve/pii/S0040195111004343*

Hooper, A., Segall, P. and Zebker, H.: 2007, Persistent scatterer interferometric synthetic aperture radar for crustal deformation analysis, with application to Volcan Alcedo, Galapagos, *Journal of Geophysical Research* **112**, 8–20.

Horasan, G. and Boztepe-Güney, A.: 2006, Observation and analysis of low-frequency crustal earthquakes in Lake Van and its vicinity, eastern Turkey, *Journal of Seismology*

11(1), 1–13.
URL: *http://www.springerlink.com/index/10.1007/s10950-006-9022-2*

Jolivet, R., Grandin, R., Lasserre, C., Doin, M.-P. and Peltzer, G.: 2011, Systematic InSAR tropospheric phase delay corrections from global meteorological reanalysis data, *Geophysical Research Letters* **38**(17), 1–6.
URL: *http://www.agu.org/pubs/crossref/2011/2011GL048757.shtml*

Jones, R. H. and Stewart, R. C.: 1997, A method for determining significant structures in a cloud of earthquakes Simplifying the Earthquake Cloud, *Journal of Geophysical Research* **102**(134), 8245–8254.

Jónsson, S.: 2009, Stress interaction between magma accumulation and trapdoor faulting on Sierra Negra volcano, Galápagos, *Tectonophysics* **471**(1-2), 36–44.
URL: *http://linkinghub.elsevier.com/retrieve/pii/S0040195108003880*

Jónsson, S., Zebker, H., Segall, P. and Amelung, F.: 2002, Fault Slip Distribution of the 1999 Mw 7.1 Hector Mine, California, Earthquake, Estimated from Satellite Radar and GPS Measurements, *Bulletin of the Seismological Society of America* **92**(4), 1377–1389.

Kampes, B. and Usai, S.: 1999, Doris: The Delft object-oriented radar interferometric software, *paper presented at 2nd Operationalization of Remote Sensing Symposium, ITC*, Enschede, Netherlands.

Karakhanian, A., Djrbashian, R., Trifonov, V., Philip, H., Arakelian, S. and Avagian, A.: 2002, Holocene-historical volcanism and active faults as natural risk factors for Armenia and adjacent countries, *Journal of Volcanology and Geothermal Research* **113**(1-2), 319–344.

Karakhanian, A. S., Trifonov, V. G., Philip, H., Avagyan, A., Hessami, K., Jamali, F., Salih Bayraktutan, M., Bagdassarian, H., Arakelian, S., Davtian, V. and Adilkhanyan, A.: 2004, Active faulting and natural hazards in Armenia, eastern Turkey and northwestern Iran, *Tectonophysics* **380**(3-4), 189–219.

Konstantinou, K. I., Kao, H., Lin, C.-h. and Liang, W.-t.: 2003, Analysis of broad-band regional waveforms of the 1996 September 29 earthquake at Bárdarbunga volcano , central Iceland : investigation of the magma injection hypothesis, *Geophysical Journal International* **154**, 134–145.

Kumagai, H., Ohminato, T., Nakano, M., Ooi, M., Kubo, a., Inoue, H. and Oikawa, J.: 2001, Very-long-period seismic signals and caldera formation at Miyake Island, Japan.,

Science (New York, N.Y.) **293**(5530), 687–90.
URL: *http://www.ncbi.nlm.nih.gov/pubmed/11474109*

Lipman, P. W.: 1997, Subsidence of ash-flow calderas: relation to caldera size and magma-chamber geometry, *Bulletin of Volcanology* **59**(3), 198–218.

Lohman, R. B. and Simons, M.: 2005, Some thoughts on the use of InSAR data to constrain models of surface deformation: Noise structure and data downsampling, *Geochemistry Geophysics Geosystems* **6**(1).

Lu, Z.: 2005, Interferometric synthetic aperture radar study of Okmok volcano, Alaska, 1992âĂŞ2003: Magma supply dynamics and postemplacement lava flow deformation, *Journal of Geophysical Research* **110**(B2), 1992–2003.
URL: *http://www.agu.org/pubs/crossref/2005/2004JB003148.shtml*

Maerten, F., Resor, P., Pollard, D. and Maerten, L.: 2005, Inverting for Slip on Three-Dimensional Fault Surfaces Using Angular Dislocations, *Bulletin of the Seismological Society of America* **95**(5), 1654–1665.
URL: *http://bssa.geoscienceworld.org/cgi/doi/10.1785/0120030181*

Manconi, A., Longpre, M.-A., Walter, T. R., Troll, V. R. and Hansteen, T. H.: 2009, The effects of flank collapses on volcano plumbing systems, *Geology* **37**(12), 1099–1102.
URL: *http://geology.gsapubs.org/cgi/doi/10.1130/G30104A.1*

Manconi, A., Walter, T. R., Manzo, M., Zeni, G., Tizzani, P., Sansosti, E. and Lanari, R.: 2010, On the effects of 3-D mechanical heterogeneities at Campi Flegrei caldera, southern Italy, *Journal of Geophysical Research* **115**(B8), B08405.
URL: *http://doi.wiley.com/10.1029/2009JB007099*

Marshall, J. and Bethel, J.: 1996, Basic Concepts of L1 Norm Minimization for Surveying Applications, *Journal of Surveying Engineering* **122**, 168–179.

Massonnet, D. and Souyris, J.-C.: 2008, *Imaging with synthetic aperture radar*, EPFL Press, Lausanne.

McTigue, D. F.: 1987, Elastic stress and deformation near near a finite spherical magma body: Resolution of the point source paradox, *J. Geophys. Res.* **92**, 12931–12940.

Michon, L., Staudacher, T., Ferrazzini, V., Bachèlery, P. and Marti, J.: 2007, April 2007 collapse of Piton de la Fournaise: A new example of caldera formation, *Geophysical*

Research Letters **34**(21), L21301.
URL: *http://www.agu.org/pubs/crossref/2007/2007GL031248.shtml*

Mogi, K.: 1958, Relations between the eruptions of various volcanoes and the deformation of the ground surfaces around them., *Bull. Earthq. Res. Inst. U. Tokyo* **36**, 99–134.

Mora-Stock, C., Thorwart, M., Wunderlich, T., Bredemeyer, S., Hansteen, T. H. and Rabbel, W.: 2012, Comparison of seismic activity for Llaima and Villarrica volcanoes prior to and after the Maule 2010 earthquake, *International Journal of Earth Sciences* .
URL: *http://link.springer.com/10.1007/s00531-012-0840-x*

Mori, J. and McKee, C.: 1987, Outward-dipping ring-fault structure at rabaul caldera as shown by earthquake locations., *Science (New York, N.Y.)* **235**(4785), 193–5.
URL: *http://www.ncbi.nlm.nih.gov/pubmed/17778631*

Nairn, I., McKee, C., Talai, B. and Wood, C.: 1995, Geology and eruptive history of the Rabaul Caldera area, Papua New Guinea, *Journal of Volcanology and Geothermal Research* **69**, 255–284.

Naranjo, J. A. and Moreno, H.: 1991, Actividad explosiva postglacial en el volcan Llaima, Andes del sur (38Âř45’S), *Revista Geologica de Chile* **18**(1), 69–80.

Ofeigsson, B. G., Hooper, A., Sigmundsson, F., Sturkell, E. and Grapenthin, R.: 2011, Deep magma storage at Hekla volcano, Iceland, revealed by InSAR time series analysis, *Journal of Geophysical Research* **116**(B5), 1–15.
URL: *http://www.agu.org/pubs/crossref/2011/2010JB007576.shtml*

Okada, Y.: 1985, Surface deformation due to shear and tensile faults in a half-space, *Bulletin of the Seismological Society of America* **75**(4), 1135–1154.

Ölmez, E., Ercan, T. and Yildirim, T.: 1994, Volcanology and Geothermal Energy possibilities of the Tendürek Area (Diyadin, Zilan, Caldıran), Eastern Anatolia (Turkey), *47. Türkeiye Jeoloji Kurultay Bildiri Özleri Kitabi 1994*, pp. 106–107.

Onn, F. and Zebker, H. a.: 2006, Correction for interferometric synthetic aperture radar atmospheric phase artifacts using time series of zenith wet delay observations from a GPS network, *Journal of Geophysical Research* **111**(B9), B09102.
URL: *http://doi.wiley.com/10.1029/2005JB004012*

Oruc, N.: 2008, Occurrence and problems of high fluoride waters in Turkey: an overview., *Environmental geochemistry and health* **30**(4), 315–23.

Parfitt, E. A. and Wilson, L.: 2008, *Fundamentals pf physical volcanology*, Blackwell Publishing, Malden, Oxford, Victoria.

Pearce, J., Bender, J., De Long, S., Kidd, W., Low, P., Güner, Y., Saroglu, F., Yılmaz, Y., Moorbath, S. and Mitchell, J.: 1990, Genesis of collision volcanism in Eastern Anatolia, Turkey, *Journal of Volcanology and Geothermal Research* **44**, 189–229.

Pinel, V., Hooper, A., De la Cruz-Reyna, S., Reyes-Davila, G., Doin, M. and Bascou, P.: 2010, The challenging retrieval of the displacement field from InSAR data for andesitic stratovolcanoes: Case study of Popocatepetl and Colima Volcano, Mexico, *Journal of Volcanology and Geothermal Research* **200**(1-2), 49–61.
URL: *http://linkinghub.elsevier.com/retrieve/pii/S037702731000380X*

Pritchard, M. E. and Simons, M.: 2002, A satellite geodetic survey of large- scale deformation of volcanic centres in the Central Andes, *Nature* **418**, 167–171.

Pritchard, M. E. and Simons, M.: 2004, An InSAR- based survey of volcanic deformation in the central Andes, *G-cubed* **5**(2).

Reilinger, R., McClusky, S., Vernant, P., Lawrence, S., Ergintav, S., Cakmak, R., Ozener, H., Kadirov, F., Guliev, I., Stepanyan, R., Nadariya, M., Hahubia, G., Mahmoud, S., Sakr, K., ArRajehi, A., Paradissis, D., Al-Aydrus, a., Prilepin, M., Guseva, T., Evren, E., Dmitrotsa, A., Filikov, S. V., Gomez, F., Al-Ghazzi, R. and Karam, G.: 2006, GPS constraints on continental deformation in the Africa-Arabia-Eurasia continental collision zone and implications for the dynamics of plate interactions, *Journal of Geophysical Research* **111**(B5), 1–26.
URL: *http://www.agu.org/pubs/crossref/2006/2005JB004051.shtml*

Roche, O., Druitt, T. H. and Merle, O.: 2000, Experimental study of caldera formation, *Journal of Geophysical Research* **105**(B1), 395.
URL: *http://doi.wiley.com/10.1029/1999JB900298*

Rosen, P. A., Henley, S., Peltzer, G. and Simons, M.: 2004, Updated Repeat Orbit Interferometry Package Released, *Eos Trans. AGU* **85**(5), 47.

Ruch, J., Anderssohn, J., Walter, T. R. and Motagh, M.: 2008, Caldera- scale inflation of the Lazufre volcanic area, South America: Evidence from InSAR, *Journal of Volcanology and Geothermal Research* **174**, 337–344.

Ruch, J., Pepe, S., Casu, F., Acocella, V., Neri, M., Solaro, G. and Sansosti, E.: 2012, How do volcanic rift zones relate to flank instability? Evidence from collapsing rifts at

Etna, *Geophysical Research Letters* **39**(20), n/a–n/a.
URL: *http://doi.wiley.com/10.1029/2012GL053683*

Ruch, J. and Walter, T.: 2010, Relationship between the InSAR-measured uplift, the structural framework, and the present-day stress field at Lazufre volcanic area, central Andes, *Tectonophysics* **492**(1-4), 133–140.
URL: *http://linkinghub.elsevier.com/retrieve/pii/S0040195110002465*

Rytuba, J. J.: 1994, Evolution of volcanic and tectonic features in caldera settings and their importance in localization of ore deposits, *Economic Geology* **89**(8), 1687–1696.
URL: *http://econgeol.geoscienceworld.org/cgi/doi/10.2113/gsecongeo.89.8.1687*

Sambridge, M. and Mosegaard, K.: 2002, Monte Carlo Methods in Geophysical Inverse Problems, *Rev. Geophys.* **40**(3).

Samsonov, S.: 2010, Topographic Correction for ALOS PALSAR Interferometry, *IEEE Transactions on Geoscience and Remote Sensing* **48**(7), 3020–3027.

Saunders, S.: 2001, The shallow plumbing system of Rabaul caldera: a partially intruded ring fault?, *Bulletin of Volcanology* **63**(6), 406–420.

Scarpati, C., Cole, P. and Perrotta, A.: 1993, The Neapolitan Yellow Tuff - A large volume multiphase eruption from Campi Flegrei, Southern Italy, *Bulletin of Volcanology* **55**, 343–356.

Scavia, C.: 1991, The Displacement Discontinuity Method in the Analysis of open cracks, *Meccanica* **26**, 27–32.

Shirzaei, M.: 2013, A Wavelet-Based Multitemporal DInSAR Algorithm for Monitoring Ground Surface Motion, *IEEE Geoscience and Remote Sensing Letters* **10**(3), 456–460.
URL: *http://ieeexplore.ieee.org/lpdocs/epic03/wrapper.htm?arnumber=6289345*

Shirzaei, M. and Walter, T. R.: 2009, Randomly iterated search and statistical competency as powerful inversion tools for deformation source modeling: Application to volcano interferometric synthetic aperture radar data, *Journal of Geophysical Research* **114**(B10), 1–16.
URL: *http://www.agu.org/pubs/crossref/2009/2008JB006071.shtml*

Shirzaei, M., Walter, T. R. and Bürgmann, R.: 2013, Coupling of Hawaiian volcanoes only during overpressure condition, *Geophysical Research Letters* **40**(April), 1–6.
URL: *http://doi.wiley.com/10.1002/grl.50470*

Shirzaei, M., Walter, T. R., Nankali, H. R. and Holohan, E. P.: 2011, Gravity-driven deformation of Damavand volcano, Iran, detected through InSAR time series, *Geology* **39**(3), 251–254.
URL: *http://geology.gsapubs.org/cgi/doi/10.1130/G31779.1*

Shou, K.-J., Siebrits, E. and Crouch, S. L.: 1997, A higher order Displacement Discontinuity Method for Three-dimensional Elastostatic Problems, *Int. J. Rock. Mech. Min. Sci.* **34**(2), 317–322.

Shuler, A., Ekström, G. and Nettles, M.: 2013, Physical mechanisms for vertical-CLVD earthquakes at active volcanoes, *Journal of Geophysical Research: Solid Earth* **118**(February), 1–18.
URL: *http://doi.wiley.com/10.1002/jgrb.50131*

Sigmundsson, F., Hreinsdóttir, S., Hooper, A., Arnadóttir, T., Pedersen, R., Roberts, M. J., Oskarsson, N., Auriac, A., Decriem, J., Einarsson, P., Geirsson, H., Hensch, M., Ofeigsson, B. G., Sturkell, E., Sveinbjörnsson, H. and Feigl, K. L.: 2010, Intrusion triggering of the 2010 Eyjafjallajökull explosive eruption., *Nature* **468**(7322), 426–30.
URL: *http://www.ncbi.nlm.nih.gov/pubmed/21085177*

Sigmundsson, F., Vadon, H. and Massonnet, D.: 1997, Readjustment of the Krafla Spreading Segment to crustal rifting measured by satellite radar interferometry, *Geophysical Research Letters* **24**(15), 1843–1846.
URL: *http://doi.wiley.com/10.1029/97GL01934*

Sigurdsson, H.: 2000, The history of volcanology, *Encyclopedia of volcanoes*, Academic Press, London, chapter The histor, pp. 15–37.

Simkin, T. and Howard, K. A.: 1970, Caldera Collapse in the Galapagos Islands , 1968, **169**(3944), 429–437.

Simkin, T. and Siebert, L.: 2013, Volcanoes of the World: an Illustrated Catalog of Holocene Volcanoes and their Eruptions. Smithsonian Institution, Global Volcanism Program Digital Information Series, webpage.
URL: *http://www.volcano.si.edu/world/*

Simons, M., Fialko, Y. and Rivera, L.: 2002, Coseismic Deformation from the 1999 M w 7 . 1 Hector Mine , California , Earthquake as Inferred from InSAR and GPS Observations, *Bulletin of the Seismological Society of America* **92**(4), 1390–1402.

Stern, C. R.: 2004, Active Andean volvanism: its geologic and tectonic setting, *Andean Geology* **31**(2), 161–206.

Sudhaus, H. and Jónsson, S.: 2009, Improved source modelling through combined use of InSAR and GPS under consideration of correlated data errors: application to the June 2000 Kleifarvatn earthquake, Iceland, *Geophysical Journal International* **176**(2), 389–404.

Surono, Jousset, P., Pallister, J., Boichu, M., Buongiorno, M. F., Budisantoso, A., Costa, F., Andreastuti, S., Prata, F., Schneider, D., Clarisse, L., Humaida, H., Sumarti, S., Bignami, C., Griswold, J., Carn, S., Oppenheimer, C. and Lavigne, F.: 2012, The 2010 explosive eruption of Java's Merapi volcano-A '100-year' event, *Journal of Volcanology and Geothermal Research* **241-242**, 121–135.
URL: *http://linkinghub.elsevier.com/retrieve/pii/S0377027312001862*

Tolluoglu, D.: 2006, *Monitoring deformations on Tendürek volcano by differential SAR interferometry*, PhD thesis, Van Yuzuncu Yil University.

Walker, G. P. L.: 1984, Downsag calderas, ring faults, caldera sizes, and incremental caldera growth, *J. Geophys. Res.* **89**(B10), 8407–8416.

Walter, T. R. and Troll, V. R.: 2003, Experiments on rift zone evolution in unstable volcanic edifices, *Journal of Volcanology and Geothermal Research* **127**(1-2), 107–120.
URL: *http://linkinghub.elsevier.com/retrieve/pii/S0377027303001811*

Wauthier, C., Cayol, V., Kervyn, F. and D'Oreye, N.: 2012, Magma sources involved in the 2002 Nyiragongo eruption, as inferred from an InSAR analysis, *Journal of Geophysical Research* **117**(B5), B05411.
URL: *http://doi.wiley.com/10.1029/2011JB008257*

Wilson, C. J. N. and Hildreth, W.: 1997, The Bishop Tuff : New Insights from Eruptive Stratigraphy 1, *The Journal of Geology* **105**, 407–439.

Wright, T. J.: 2003, Source model for the M w 6.7, 23 October 2002, Nenana Mountain Earthquake (Alaska) from InSAR, *Geophysical Research Letters* **30**(18), 30–33.
URL: *http://www.agu.org/pubs/crossref/2003/2003GL018014.shtml*

Yang, X.-M., Davis, P. M. and Dieterich, J. H.: 1988, Deformation From Inflation of a Dipping Finite Prolate Spheroid in an Elastic Half-Space as a Model for Volcanic Stressing, *J. Geophys. Res.* **93**, 4249–4257.

Yılmaz, Y., Guner, Y. and Şaroğlu, F.: 1998, Geology of the quaternary volcanic centres of the east Anatolia, *Journal of Volcanology and Geothermal Research* **85**(1-4), 173–210.

Yun, S., Segall, P. and Zebker, H.: 2006, Constraints on magma chamber geometry at Sierra Negra Volcano, Galápagos Islands, based on InSAR observations, *Journal of Volcanology and Geothermal Research* **150**(1-3), 232–243.
URL: *http://linkinghub.elsevier.com/retrieve/pii/S0377027305002611*